Imperial College of Science, Technology and Medicine
Department of Materials

Computer Simulations of Functional Solid Oxides

Ji Wu

Submitted in part fulfilment of the requirements for the degree of
Doctor of Philosophy in Materials of Imperial College,
March 2017

Abstract

Several novel mixed ionic-electronic conductors (MIECs) based on the oxygen interstitial diffusion mechanism have been developed and studied for the past decade. This kind of materials has the potential to be used as the cathode of intermediate temperature solid oxide fuel cell (IT-SOFC) systems. Among them, the $La_2NiO_{4+\delta}$ Ruddlesden-Popper (RP) and the $CeNbO_{4+\delta}$ Fergusonite materials attract particular attention due to their interesting properties. These materials are capable to take extra oxygen and become oxygen ion conductor without any aliovalent doping. To understand more about their catalytic and diffusion behaviours, atomistic computer simulations using both classical pair potentials and density functional theory (DFT), as well as classical thermodynamics calculations, have been carried out on these materials.

The $La_2NiO_{4+\delta}$ material has recently been discovered to exhibit a La-only surface[1–3]. This observation disagrees with previous theoretical study which suggest a Ni-terminated surface and challenges the traditional belief that the oxygen reduction takes place on $La_2NiO_{4+\delta}$'s exposed Ni sites. Our hybrid DFT surface energy calculation suggests that the most stable (001) La_2NiO_4 surface is La terminated. Previous theoretical surface study's results may not appropriately reflect the room temperature La_2NiO_4 sample. To explain the La-only surface observed on the polycrystalline $La_2NiO_{4+\delta}$ samples, a thermodynamic decomposition based hypothesis is proposed. The evaluation of La_2NiO_4's stability with respect to the higher ordered RP materials ($La_3Ni_2O_7$, $La_4Ni_3O_{10}$ and $LaNiO_3$) shows that the decomposition of La_2NiO_4 is thermodynamically favourable and supports our hypothesis. The defective La-Ni-O RP material's decomposition thermodynamics are estimated with the help of hybrid DFT calculations and agree with our hypothesis too. The decomposition hypothesis predicts a Ni-enriched subsurface layer and agrees with the experiments.

The La vacancy formation energy and diffusion barriers are calculated with hybrid DFT methods, as these results may provide hints on why the thermodynamically favourable decomposition only limits to the surface of La_2NiO_4. Before these calculations, different input La_2NiO_4 phases and magnetic orderings are evaluated to check their impacts on simulation results' reliability. We have shown that the choice of input structure and magnetic ordering will have significant effect on the simulation results. Appropriate choice of the input setups is therefore very important to the quality of the simulation. Based on the evaluation, La_2NiO_4's room temperature Fmmm phase and g_x type anti-ferromagnetic ordering are selected for the DFT calculations.

The La vacancy formation energy and diffusion barrier calculated are compared to the oxygen defect formation energy and related diffusion barrier. Possible relations between the La_2NiO_4 decomposition reaction and the La vacancy's formation/diffusion energetics are also discussed.

Similar to the $La_2NiO_{4+\delta}$, the $CeNbO_{4+\delta}$ Fergusonite material has a range of different oxygen enriched phases and is able to conduct oxygen ions. Its characteristic complex modulated structures also attracts much attentions. The details of its modulated oxygen-rich structures remained unclear for a long time. Recently the $CeNbO_{4.25}$ modulated structure has been fully solved[4] and opens opportunity for further theoretical studies. Molecular dynamics simulations using classical pair potentials are carried out on the stoichiometric $CeNbO_4$ and the modulated $CeNbO_{4.25}$ materials to study the oxygen diffusion pathways for the first time. The calculated oxygen ions' mean-squared displacements clearly show that the stoichiometric $CeNbO_4$ exhibits no oxygen self diffusion up to 1773 K. In addition, the oxygen diffusion coefficients in the $CeNbO_{4.25}$ are calculated and plotted over a range of temperatures. Three regions with different oxygen diffusion behaviours are found from the graph and the oxygen diffusion activation energies are calculated for each of the regions. The differences and similarities between the computed oxygen diffusion behaviours and the experimentally observed oxygen diffusion behaviours are explored and discussed. Finally, the oxygen diffusion trajectory snapshots are taken from the MD simulation. The exact oxygen diffusion pathways and possible diffusion anisotropicities of the $CeNbO_{4.25}$ material are analyzed and discussed based upon the diffusion trajectories.

Acknowledgements

I would like to thank my mentors, friends, family and everyone in the Solid State Ionics group for all your support, kindness, coffee powers and inspirations. In particular, I would like to express my most sincere gratitudes to Andrew, Stephen and John for all the advices, discussions, support and patience over all my years at Imperial College. The completion of this thesis would not be possible without you. Special thanks goes to Prof. Robin Grimes, Michael Rushton and Giuseppe Mallia, who taught me all the tricks in computer simulations. These tricks and skills I learned will certainly go a long way. I also want to thank Yongkun and Zhengrong. Being from different academic backgrounds, your insights always show me very enlightening and extremely useful perspectives.

Last but not least, I would like to thank KAUST for their continued financial support throughout this project.

Dedication

To Tongsheng Shu and Yulin Huang, My dearest Grandmother and Grandfather.

Declaration

I hereby declare that the contents of this thesis are original except where specific reference is made to the work of others. This thesis is my own work and any results from work done in collaboration with others are stated specifically in the text.

Copyrights

The copyright of this thesis rests with the author and is made available under a Creative Commons Attribution Non-Commercial No Derivatives licence. Researchers are free to copy, distribute or transmit the thesis on the condition that they attribute it, that they do not use it for commercial purposes and that they do not alter, transform or build upon it. For any reuse or redistribution, researchers must make clear to others the licence terms of this work.

©2016 Ji Wu

‘Now the general who wins a battle makes many calculations in his headquarters ere the battle is fought. The general who loses a battle makes but few calculations beforehand. Thus do many calculations lead to victory, and few calculations to defeat: how much more no calculation at all!’

Sun Tzu: The Art of War

Contents

Abstract **i**

Acknowledgements **iii**

1 Introduction **1**

1.1 Motivation 1

1.2 Overview of Fuel Cells 3

1.3 Materials for Solid Oxide Fuel Cells 5

1.3.1 Lanthanum Nickelate Ruddlesden-Popper Materials 6

1.3.2 La_2NiO_4 structures 8

1.3.3 La_2NiO_4 magnetism 11

1.3.4 Electronic and electrical properties of La_2NiO_4 13

1.3.5 Surface analysis of La_2NiO_4 15

1.4 Lattice Defects and Defect Notations 16

1.4.1 Kröger-Vink Notation 17

1.4.2 Schottky Defects 17

1.4.3 Frenkel Defects 18

2 Methodology **19**

2.1 Equilibrium Thermodynamics 20

2.1.1 Gibbs phase rule 22

2.1.2 Shomate equation 23

2.2 Classical Potential Simulations 23

2.2.1 Coulombic Interaction 24

2.2.2 Short Range Interactions 24

2.2.3 Molecular Dynamics 26

2.3 Quantum Mechanic Simulations 28

2.3.1 Density Functional Theory 28

2.3.2 Exchange-Correlation Approximation 30

2.3.3 Bloch's Theorem 32

2.3.4 Basis Sets 34

2.4 Defect Energy Calculation 38

2.4.1 Supercell Method 38

2.4.2 Mott-Littleton Approximation 39

2.5 Surfaces 41

2.5.1 Types of Surfaces 42

2.5.2 Simulating Surfaces 43

3 LNO214: the surface mystery **44**

3.1 Introduction 44

3.2 The LNO214 surface energy 46

3.2.1 Calculation details 47

3.2.2 Results and discussion 49

3.3 Thermodynamic stability of the LNO214 material 52

3.3.1 Gibbs energy of reaction for stoichiometric cases 52

3.3.2 DFT augmented Gibbs free energy for non-stoichiometric reactions . . . 54

3.3.3 Thermodynamic stability for perfect LNO214 57

3.3.4 Defective La-Ni-O compounds 66

3.4 Conclusion 67

4 LNO214 defects and diffusion kinetics 70

4.1 Introduction 70

4.2 Evaluation of simulation setup 71

4.3 La defect formation energy 78

4.3.1 Calculations of metal chemical potentials 80

4.4 La vacancy migration energy in La_2NiO_4 85

4.5 Conclusion 86

5 Oxygen diffusion in $CeNbO_{4.25}$ 89

5.1 Introduction 89

5.2 $CeNbO_4$ and $CeNbO_{4.25}$ Crystallography 90

5.3 Computational Details 93

5.4 Oxygen diffusion in $CeNbO_4$ and $CeNbO_{4.25}$ 95

5.5 Conclusion 104

6 Summary and Further Work **106**

6.1 $La_2NiO_{4+\delta}$ Ruddlesden-Popper materials 106

6.1.1 La_2NiO_4 surface energy 106

6.1.2 $La_2NiO_{4+\delta}$ surface stability 108

6.1.3 La vacancy in $La_2NiO_{4+\delta}$ 111

6.2 $CeNbO_{4+\delta}$ Fergusonite material 114

Bibliography **116**

List of Tables

1.1 Different types of fuel cell and relevant operation specifics[9] 5

1.2 Summary of phase morphology and lattice parameters of $La_2NiO_{4+\delta}$ at various temperature; a, b, c are three lattice parameters of the $La_2NiO_{4+\delta}$ structure. R.T. refers to room temperature with no additional in situ temperature control. LTT, RTO, HTT stands for low temperature tetragonal phase, room temperature orthorhomic phase and high temperature tetragonal phase respectively. Non-stoichiometric data is marked with * and noted as N.A. for phase information, as these non-stoichiometric cases are not parts of the ideal phase morphology. . . 9

1.3 (La+Sr):Ni ratio calculated from the fitted XPS spectra taken on the (001) surfaces at different angles as reported by Burriel. The heat treated sample were heated at 450°C for 72 hours in air.[1] 16

2.1 Comparison of calculated and experimental lattice parameters of relevant La-Ni-O RP materials. Expt. is experimental structure, and Calc. is calculated structure. Old basis sets refer to the literature La basis sets which La f-orbital is not included. New basis sets refer to the La basis sets with tuned f-orbital from this work. All literature experimental structures are measured at 298K. 38

3.1 Comparison of calculated and literature surface energies of two possible La_2NiO_4 surface terminations. NiO2/LaOOLa and LaO are the labels of the respective termination surfaces as discussed. The literature value for the Ni surface is from a simulation based on the low temperature LNO214 (001) surface. This value is not suitable for a direct comparison and is listed for indicative purpose only. . . 51

3.2 Thermodynamic parameters used to evaluate the change in Gibbs free energy for La_2NiO_4 decomposition. Note that for the phase transition of $La_3Ni_2O_7$ at 490K, we have $\Delta_{tr}H = 1800\text{Jmol}^{-1}$, $\Delta_{tr}S = 3.674\text{Jmol}^{-1}K^{-1}$.[92] The values here are applicable from 305K to 1673K 52

3.3 Oxygen thermodynamic constants from NIST handbook for various temperature ranges.[95] 54

3.4 Comparison of calculated and experimental lattice parameters of relevant La-Ni-O species. Expt. is experimental structure, and Calc. is calculated structure. All literature experimental structures are measured at 298K. 66

4.1 Summary of La_2NiO_4 experimental lattice parameters used in this work. These phases are measured at temperature T as listed. LTT, RTO and HTT stands for low temperature tetragonal phase, room temperature orthorhombic phase and high temperature tetragonal phase respectively. 72

4.2 Summary of different optimised La_2NiO_4 phases with ferromagnetic (FM) and antiferromagnetic (AFM) ordering. For the high temperature phase, a calculation using no magnetic ordering is also included (labelled as NM). The energy difference per unit cell (ΔE) between the AFM and the FM calculations are also included. The percentage differences between each calculated and experimental lattice constants are listed below the relevant calculated data. The AFM calculations are used as the reference state in each case. Mag. Config. stands for magnetic configuration. In the case of experimental values, the magnetic configuration is listed as Exp. 73

4.3 The magnetic coupling constant (J) calculated are listed in milli-electronvolt. The experimental value reported was measured at 35 K. The Néel temperature measured for the ideal La_2NiO_4 is 328 K. The literature simulation results were calculated using unrestricted Hartree-Fock method and a modified B3LYP functional (mixing 35% Hartree-Fock exchange instead of 20%). The literature calculations used the I4/mmm experimental structure without geometric optimisation. 76

4.4 Comparison of calculated and experimental Gibbs free energy of formation (eV per formula unit) of relevant La-Ni-O Ruddlesden-Popper materials. The experimental Gibbs free energy of formation are measured at 298.15 K. 81

5.1 Buckingham pair potential parameters considered for relevant ion pairs. For both potential set A and B, the Ce^{3+} - O^{2-} and Ce^{4+} - O^{2-} potential parameters are taken from Vyas and Minervini's works[132,133]; the Nb^{5+} - O^{2-} potential is taken from Sepliarsky's work[134]. For the potential set A, the O^{2-} - O^{2-} potential is taken from Vyas and Minervini's works[132,133]. For the potential set B, the O^{2-} - O^{2-} potential is taken from Sepliarsky's work[134] and different from the one used in potential set A. 94

5.2 Comparison of experimental and calculated lattice parameters of $CeNbO_4$ and $CeNbO_{4.25}$. The percentage differences are calculated with respect to the experimental lattice constants. The calculated lattice parameters are resulted from two different sets of pair potentials. The experimental lattice parameters are measured at room temperature. See Table 5.1 for the details of the pair potential sets' parameters. 95

List of Figures

1.1 Schematic of an integrated renewable energy cycle. Hydrogen/short-chain hydrocarbon fuels and solid oxide electrolyser cell - solid oxide fuel cell (SOEC-SOFC) systems can play an important role to support wider usage and grid-level integration of solar and wind powers. 3

1.2 Illustration of a typical first order Ruddlesden-Popper structure; grey spheres are A site atoms, black spheres are B site atoms, and red spheres are oxygen atoms. 7

1.3 Illustration of the LTT (P42/ncm), RTO (Fmmm) and HTT (I4/mmm) La_2NiO_4 structures, produced with experimental crystallographical information reported in Table 1.2. Both (001) top views and (010) side views of the three phases are shown in this figure. In the (001) top view, the grey octahedra are NiO_6 octahedra and the grey spheres are Ni atoms. La atoms are omitted in the (001) top view for clarity. In the (010) side views, grey spheres are La atoms, red spheres are oxygen atoms, black spheres are Ni atoms. Tilting of the NiO6 octahedra can be seen clearly for the LTT phase. 10

1.4 Illustration of the relationship between orthorhombic and tetragonal representations of $La_2NiO_{4+\delta}$. Left is othorhombic x-y plane. Right is tetragonal x-y plane. Ni atoms are grey; La atoms are green; O atoms are red. 11

1.5 Illustration of the g_x magnetic spin configuration of pure La_2NiO_4[32]. The green arrows' directions indicate spin directions. The unit cell illustrated is the 1 × 1 × 1 conventional crystallographic cell of La_2NiO_4. The top xy NiO_2 layer is linked to the bottom xy NiO_2 layer by translational symmetry and therefore these two layers are identical. 12

1.6 Illustration of the Kröger-Vink notation rules.[52] 17

2.1 Comparison of total pair potential and its constituent long range Coulombic potential and short range Buckingham potential of an example ion pair. 26

2.2 Change in the energy differences between the SCF test runs with respect to the reference energy state in eV. The reference energy is the input La_2NiO_4 structure's SCF total energy computed using literature La basis sets. Only the exponent of the primitive Gaussian type function (GTF) for the La f-orbital is altered between the runs. 37

2.3 Schematic representation of the regions considered in the Mott-Littleton method. Region I contains the defect and is calculated explicitly. In region IIa, ions are displaced based on the polarisation effects of the defects. The interactions between the region I ions and region IIa ions are still calculated explicitly. Region IIb includes the rest of the bulk lattice and extends to infinity. 40

2.4 Three types of Tasker's surfaces for ionic solids. From left to right: Type I, Type II and Type III 42

2.5 Schematic representation of the surface evaluation method. 43

3.1 LNO214 slabs cleaved at different terminations along the [001] direction. These different terminations are named as NiO2, LaOOLa, NiO/LaOOLa and LaO respectively as shown. The charge listed in the bracket is the total charge of that particular layer. The total charge listed is the charge accumulated by summing the charges from that particular layer and all layers above up to the top surface layer. 47

3.2 Surface energies of LaO terminated La_2NiO_4 slabs plotted with respect to the thickness of the slabs. The slabs with 5, 10, 15 and 20 atomic layers are calculated. The surface energies are computed with respect to 50

3.3 A schematic showing the interstitial oxygen position added in the La_2NiO_4 structure. The highlighted light blue sphere represents the intersitial oxygen. Lattice oxygen atoms are coloured in red. La atoms are coloured in grey. Ni atoms are coloured in black. The crystal structure shown here is a calculated relaxed structure. Distortions caused by the interstial oxygen can be seen clearly in this figure. A Ni atom at the corner is not drawn on this sketch due significant distortion from its ideal lattice position. This Ni atom is still properly treated in the calculations. 58

3.4 A representation of the proposed layered structure, with reconstructed La_2O_3 exposed as the surface layer, $La_3Ni_2O_7$ or $La_4Ni_3O_{10}$ being the intermediate layer between the surface and the bulk La_2NiO_4 60

3.5 Gibbs energy change for the reaction La_2NiO_4 decomposing into $LaNiO_3$, $La_3Ni_2O_7$ or $La_4Ni_3O_{10}$ and La_2O_3 at 0.2 bar oxygen partial pressure over the temperature range of 305-1673 K. In the legend, the label LNO327 is for decomposition into $La_3Ni_2O_7$, LNO4310 is for $La_4Ni_3O_{10}$, and LNO113 is for $LaNiO_3$. 60

3.6 Gibbs reaction energy for La_2NiO_4 into $La_3Ni_2O_7$ and La_2O_3 over the range of 1 bar to 1×10^{-25} bar oxygen partial pressure, and 305K to 1673K. The colour bar reflects the Gibbs energy of reaction in kJ/mol. The Gibbs energy of reaction is equal to zero at the edge between the blue and yellow regions. 61

3.7 Gibbs reaction energy for La_2NiO_4 into $La_4Ni_3O_{10}$ and La_2O_3 over the range of 1 bar to 1×10^{-25} bar oxygen partial pressure, and 305K to 1673K. The colour bar reflects the Gibbs energy of reaction in kJ/mol. The Gibbs energy of reaction is equal to zero at the edge between the blue and yellow regions. 62

3.8 Comparison of Gibbs reaction energy for La_2NiO_4 decomposition into $La_3Ni_2O_7$ (labelled as ideal), $La_2NiO_{4.25}$ decomposition into $La_3Ni_2O_7$ (214-defect) and La_2NiO_4 decomposition into $La_3Ni_2O_{6.75}$ (327-defect) at 0.2 bar oxygen partial pressure over the range of 305-1673 K. 64

3.9 Comparison of Gibbs reaction energy for La_2NiO_4 decomposition into $La_4Ni_3O_{10}$ (labelled as ideal), $La_2NiO_{4.25}$ decomposition into $La_4Ni_3O_{10}$ (214-defect) and La_2NiO_4 decomposition into $La_4Ni_3O_{9.5}$ (4310-defect) at 0.2 bar oxygen partial pressure over the range of 305-1673 K. 65

4.1 Density of states map for the low temperature (P42/ncm), room temperature (Fmmm) and high temperature (I4/mmm) phases of La_2NiO_4 with ferromagnetic ordering. The gray line is for La, the black line is for Ni and the red line is for O. The Fermi energies are marked as zero on the energy axes. 78

4.2 Density of states map for the low temperature (P42/ncm), room temperature (Fmmm) and high temperature (I4/mmm) phases of La_2NiO_4 with antiferromagnetic ordering. The gray line is for La, the black line is for Ni and the red line is for O. The Fermi energies are marked as zero on the energy axes. 79

4.3 Two dimensional phase diagrams plotted using calculated Gibbs formation energies of La_2NiO_4, La_2O_3 and NiO. Top is the La energetic phase diagram. Bottom is the Ni energetic phase diagram. The regions above the La_2NiO_4 line and below the La_2O_3 or NiO line are the La_2NiO_4 stability regions in both diagrams. . . . 83

4.4 Schematics of two La diffusion pathways via vacancy mechanism in a LNO214 2×1×1 supercell with one La vacancy. In the figure, grey is La atom, black is Ni atom and red is O atom. The semi-transparent atom represents La vacancy. (a) shows the La migration pathway in the rocksalt layer. (b) shows the La migration pathway in the perovskite layer. 85

5.1 Projected crystal structures of $CeNbO_4$ (right) and $CeNbO_{4.25}$ (left)[4,128] along [100] and [010] axes are compared. The interstitial oxygens clearly distort the $CeNbO_{4.25}$ structure and symmetry is broken. Ce^{3+}, Ce^{4+}, Nb^{5+} and O^{2-} are represented with yellow, blue, green and red spheres respectively. 91

5.2 Comparison of projected crystal structures of $CeNbO_4$ (a) and $CeNbO_{4.25}$ (b) along [100] axes with polyhedra highlighted.[4] NbO_6, NbO_7 and NbO_8 polyhedra are coloured with green, purple and orange respectively. The NbO_7 and NbO_8 polyhedra are connecting different x-z planes of NbO_6 in $CeNbO_{4.25}$ and possibly enhancing diffusion by providing extra intermediate interstitial sites. 92

5.3 Comparison of MD calculated mean-squared displacements (MSDs) of oxygen ions in (a) $CeNbO_{4.25}$ and (b) $CeNbO_4$ materials over temperatures ranging from 1173 K to 1773K. Data from the first 60 ps are omitted to ensure equilibration and low noise.[4] 96

5.4 Summary of calculated oxygen diffusion coefficients in $CeNbO_{4.25}$ over a temperature range of 1073 K to 2173K. Three regions with different diffusion activation energies are labelled. Diffusions at additional temperatures are calculated to ensure the trends in all the three regions are represented reliably.[4] 97

5.5 Oxygen diffusion trajectories over 100 ps captured in $CeNbO_4$ (a, d) at 673 K and $CeNbO_{4.25}$ (b, c, e, f) at 673 K and 1073 K. Local oxygen diffusion trajectories over 20 ps in $CeNbO_{4.25}$ at 1573 K are enlarged and shown in (g). The cyan, dark blue and red dots are representing $Ce^{3+/4+}$, Nb^{5+} and O^{2-} ions respectively. Oxygen diffusions in the x-z planes can be seen clearly. Occasional diffusions in y-direction are also observed (circled region).[4] 100

5.6 The MSDs of oxygen ions in $CeNbO_{4.25}$ at 1573 K separated into x, y and z directions are summarized together with the total oxygen MSD. The O_ x, O_ z and O_ y labels correspond to the oxygen MSD in x-direction, y-direction and z-direction respectively. Note that the angles between the x and z directions are about 105 ° and y-directon is perpendicular to the x-z plane. Please refer to Fig. 5.1 and Fig. 5.2 for illustration of the directions. The x and z directions The first 60 ps is still omitted and the starting 0 ps in this graph is the same time as the 60 ps in Fig. 5.3. The MSD data agrees with trajectory projections and shows the majority of oxygen diffusion is in the x-z plane. The diffusion in y-direction is not zero though. 102

5.7 All the oxygen ions in the minimum cell of $CeNbO_{4.25}$ are labelled from O1 to O204. The distribution of the labelled oxygen ions' calculated diffusion coefficient in the enlarged $CeNbO_{4.25}$ supercell at 1773 K is summarized in this figure. The x-axis is starting from $1.40\times10^{-7}cm^2s^{-1}$ to $18.05\times10^{-7}cm^2s^{-1}$ and is evenly divided into 10 regions. Each of the bars represents the number of interstitial oxygen ions with diffusion coefficients inbetween the previous x-axis label and the current one. For example, the first bar shows the number of interstitial oxygen ions with diffusion coefficient inbetween $1.40\times 10^{-7}cm^2s^{-1}$ to $3.07\times 10^{-7}cm^2s^{-1}$. The distribution peak is quite close to the median of diffusion coefficients. 103

Chapter 1

Introduction

1.1 Motivation

In our era, securing energy supply and combating climate change are two of the most pressing issues. These two issues are certainly interconnected. According to the United Nations (IPCC reports)[5], one of the major causes of the climate change is greenhouse gas emitted from energy generation with fossil fuels. While we need more energy to lift more people from poverty and hunger, greenhouse gas emission must be reduced to control climate change. To achieve these two goals at the same time, a significant increase of renewable energy generation is required.

To make renewable energy affordable and secure, a number of clean energy sources need to be harvested. The most promising candidates are solar, wind and nuclear energy. However, these energy sources all have limitations, e.g. limited sunshine time in winter at high-latitude regions or unstable wind flow. Nuclear power plants (to be more specifically, the fission power plants) are robust sources of energy compared to wind and solar power. However, there is always a concern of possible accidents. The risk of a major nuclear accident is very low for newer generations of nuclear power plants, but the consequences of a single major accident can be devastating, as seen in Chernobyl and Fukushima. In addition, the management of nuclear wastes (including depleted fuels and contaminated sites) remains a challenge. To utilize the clean but relatively unstable wind and solar powers at grid level, advanced energy storage

technologies must be combined to form an integrated energy supply system to ensure robustness. In such an integrated system, surplus energy produced by wind and solar power is stored in some systems. The stored energy is then released later to fill the gap between consumption need and generation capability. Among several available energy storage technologies, solid oxide fuel cell (SOFC) based energy storage systems are very promising.

The solid oxide fuel cell (SOFC) system consumes hydrogen (or short-chain hydrocarbons) and oxygen to produce electricity and water. It is a very clean system and emits no greenhouse gas if hydrogen fuel is used. When short-chain hydrocarbons are used as SOFC fuels, carbon neutrality can be achieved if the amount of carbon contained in the products is equal to the amount of carbon consumed during the fuel production cycle. Surplus energy from wind and solar power can be used for hydrogen or simple hydrocarbon fuel production via water electrolysis or direct photocatalytic water splitting. When energy is needed, the SOFC system converts hydrogen or short-chain hydrocarbon fuel into electricity. As the surplus energy is stored in the form of hydrogen (or methane for high temperature SOFC), the SOFC storage system has potential to achieve an energy density comparable to gasoline[6]. Direct transportation of hydrogen is indeed challenging, but converting hydrogen into methane or methanol can solve the problem: methane or methanol can be transported through existing fossil fuel transportation infrastructures. For such a system, the fuel flexibility of the SOFC becomes crucial. In addition, it is relatively easy to scale SOFC systems to produce a large power throughput. The SOFC units can be simply stacked to produce required voltage without the need of sophisticated control systems. Combining easy transportation, high energy density and large power throughput, the SOFC system becomes a very attractive option for grid scale energy storage. A more recent proposal of a combined solid oxide electrolyser cell - solid oxide fuel cell (SOEC-SOFC) system[7], which uses a single device to produce hydrogen or electricity as required, further increases the technology's attractiveness as the energy storage in an integrated renewable energy cycle as shown in Fig. 1.1.

Currently, the main question in the field of SOFC is how to make it more economic. This can be achieved by reducing the working temperature of SOFC (operational cost), alleviating materials degradation (operational cost), cutting fabrication cost or a combination of these. Novel func-

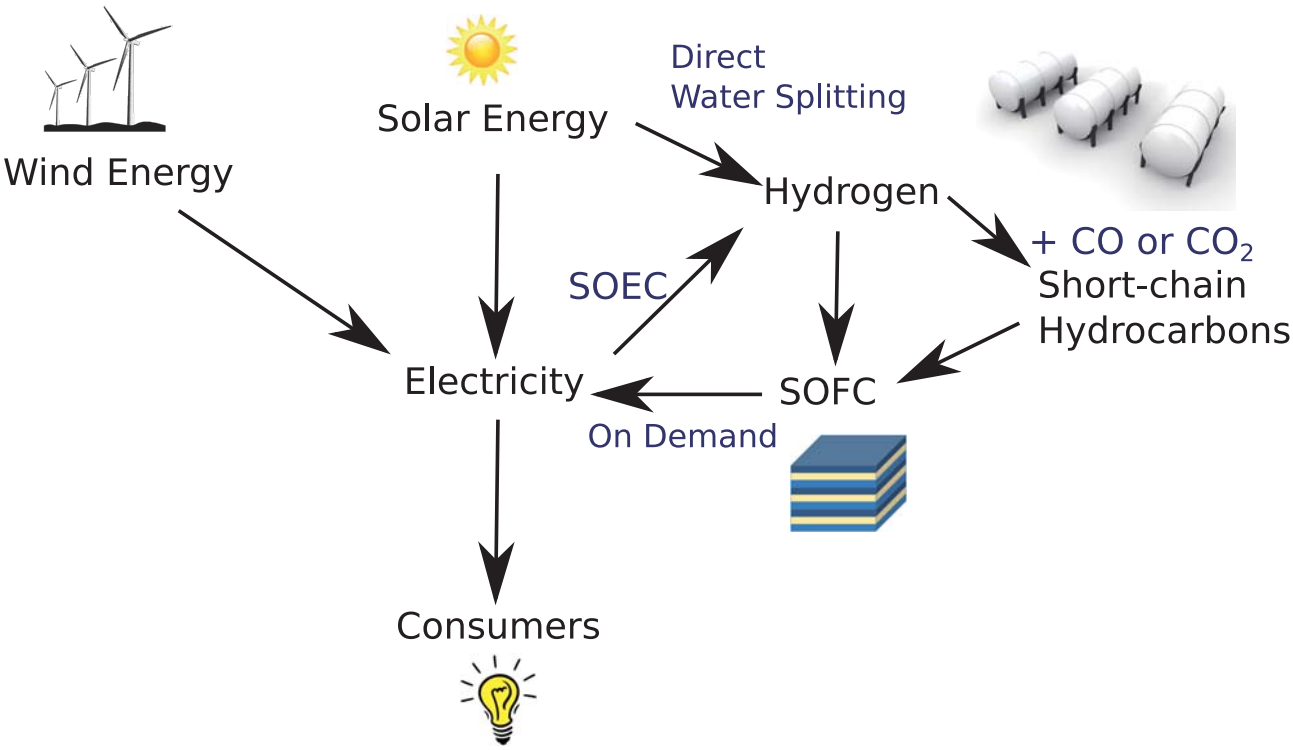


Figure 1.1: Schematic of an integrated renewable energy cycle. Hydrogen/short-chain hydrocarbon fuels and solid oxide electrolyser cell - solid oxide fuel cell (SOEC-SOFC) systems can play an important role to support wider usage and grid-level integration of solar and wind powers.

tional oxide materials are key to address these questions. The ruddlesden-popper lanthanum nickelate $La_2NiO_{4+\delta}$ (LNO214+δ) and fergusonite cerium niobate $CeNbO_{4.25}$ (CNO425) are two interesting oxygen conducting oxides for potential SOFC applicaton. These two materials are investigated using computational simulation techniques in this thesis.

1.2 Overview of Fuel Cells

The idea of a fuel cell dates back to Sir William Grove's work in 1839[8]. Till today, all fuel cells still share the same three basic components: the cathode, the electrolyte, and the anode. Although named as electrical cells, the fuel cells should be better considered as generators. Unlike lead-acid batteries or Li-ion batteries, fuel cells do not store energy in the electrodes. Instead, the fuel cells consume fuels (usually hydrogen or simple hydrocarbons) to generate electricity through redox reactions, somewhat similar to the generation of mechanical energy

through burning fuels in the combustion engines. As the energy is stored in the fuels, the fuel cell systems can achieve a quite high energy density, depending on the type of fuel and conversion efficiency.

The underlying chemical reactions in a fuel cell are as follows: At the cathode

$$O_2 + 4e^- \rightarrow 2O^{2-} \tag{1.1}$$

At the anode

$$O^{2-} + H_2 \rightarrow H_2O + 2e^- \tag{1.2}$$

It is easy to see that the main product in fuel cell operation is water. No hazardous byproduct is produced. This fundamental reaction also defines the materials selection requirements for the anode, electrolyte and cathode materials. At the cathode, or the oxygen electrode, the electrode will experience an oxidising environment. Ideally, to enhance reaction efficiency and speed, the cathode material should be able to transport electrons and oxygen ions at the same time. For the fuel electrode (anode) side, the material experiences a reducing environment. The anode must be a good electronic conductor to produce electrical output, as the reaction equation suggests. The solid electrolyte's duty is to transport the oxygen ions produced at the cathode to the anode, where the oxygen ions react with hydrogen to produce water and electricity. Naturally, the electrolyte material is required to be a good oxygen ionic conductor but an electron insulator to prevent current leakage. Usually, the two redox reactions take place at the gas-electrode-electrolyte triple phase boundaries. Therefore, both the cathode and the anode are made porous to maximize the triple phase boundaries' area in applications. On the other hand, dense materials are produced for property characterisations, as it is much easier to compare performances of standardized dense materials.

Sharing the same operation principles, fuel cells can be classified into many different types based on their electrolyte material, fuel and working temperature. The following table (Table 1.1) gives a list of common fuel cell types and some operation specifics:

Table 1.1: Different types of fuel cell and relevant operation specifics[9]

Type of fuel cell	Electrolyte	Operation Temperature	Fuel	Efficiency
Polymer Exchange Membrane Fuel Cell	Polymer (proton exchange membrane)	50-80^{o}C	Hydrogen, produced hydrocarbons or methanol	40-50%
Alkaline Fuel Cell	Potassium hydroxide	50-200^{o}C	Pure hydrogen or hydrazine liquid methanol	50-55%
Phosphoric Acid Fuel Cell	Phosphoric Acid	160-210^{o}C	Hydrogen, produced hydrocarbons or methanol	40-50%
Molten Carbonate Fuel Cell	Molten salts, e.g. NO_3 and SO_4	630-650^{o}C	Hydrogen, CO, natural gas, propane	50-60%
Direct Methanol Fuel Cell	Polymer	60-200^{o}C	Liquid methanol	40-55%
Solid Oxide Fuel Cell	Ceramics, e.g. Yttrium stablized Zirconia(YSZ) and Ceria-doped Gadolinium Oxide (CGO)	600-1200^{o}C	Hydrogen, produced hydrocarbons, natural gas or propane	45-60%

1.3 Materials for Solid Oxide Fuel Cells

Among the various types of fuel cells, solid oxide fuel cell (SOFC) attracts particular interest due to its compactness and high efficiency. In addition to the standard hydrogen fuel, the SOFC's capability to use certain hydrocarbons, like methane or natural gas, directly is also an advantage. However, a conventional SOFC suffers several performance and longevity problems as it requires a high operation temperature (about 800 - 1200 °C). These issues are associated with the materials selected in conventional fuel cell design. For example, the cathode materials used in association with YSZ electrolyte, $La_{1-x}Sr_xMnO_{3-\delta}$(LSM) and $La_{1-x}Sr_xCo_{1-y}Fe_yO_{3-\delta}$ (LSCF), will crack at the operation temperature due to significant thermal expansion coefficient differences.[10] The high operation temperature also increases maintenance cost of SOFCs. These issues potentially limit widespread application of SOFCs.

To resolve these issues, new electrolyte materials that possess great ionic conductivity at

intermediate temperature (around 600^{o}C) have been discovered, e.g. ceria-doped gadolinia $Ce_{1-x}Gd_xO_{2-\delta}$ (CGO)[11] and lanthanum-strontium-magnesium-gallates $La_{1-x}Sr_xMg_{1-y}Ga_yO_{3-\delta}$(LSGM). Meaningwhile, novel cathode materials must also be identified to suit these new electrolytes at the relevant operation temperature. To be specific, the cathode material must be a good mixed ionic-electronic conductor, which could allow quick O^{2-} ions and electrons movement at the same time. These requirements present a unique materials challenge.

1.3.1 Lanthanum Nickelate Ruddlesden-Popper Materials

During the search for novel SOFC cathode materials, $La_2NiO_{4+\delta}$, and the Ruddlesden-Popper(RP) family of materials, have attracted significant attentions in recent years.[12–14] $La_2NiO_{4+\delta}$ possesses relatively large ionic conductivity and reasonable electrical conductivity at the same time. Compared to conventional perovskite cathode materials, $La_2NiO_{4+\delta}$ exhibits at least an order of magnitude larger oxygen ionic conductivity at intermediate temperature[10,15]. This unusual property could be attributed to the significant number of excess oxygen ions accommodated in the RP structure. Experimental analysis of $La_2NiO_{4+\delta}$ showed that the oxygen hyperstoichiometry δ could take a wide range of $0 \leq \delta \leq 0.25$[16,17]. An illustration of a first order Ruddlesden-Popper structure is displayed in Fig. 1.2.

Apart from a structural investigation of $La_2NiO_{4+\delta}$, the details of the oxygen ionic diffusion process has also attracted significant attention, due to direct connection between this ionic diffusion process and SOFC cathode performance. Experimental investigation with O^{18} isotope tracer analysis[14,15,18] and modelling work using molecular dynamics simulation[19] together give a quite satisfactory description of the oxygen ion diffusion process in $La_2NiO_{4+\delta}$.

While the bulk O^{2-} ionic diffusion process in $La_2NiO_{4+\delta}$ is rather well understood, the surface properties, including surface structure and surface chemistry of O_2 reduction, still remain largely unexplored[20]. Understanding the $La_2NiO_{4+\delta}$ surface structure and related chemical reactions might suggest possible improvements of performance, as the surface O_2 reduction process could potentially be the reaction rate-determining step. Therefore, $La_2NiO_{4+\delta}$ is selected to be the focus of study. The Ruddlesden-Popper (RP) family of materials shares a general chemical

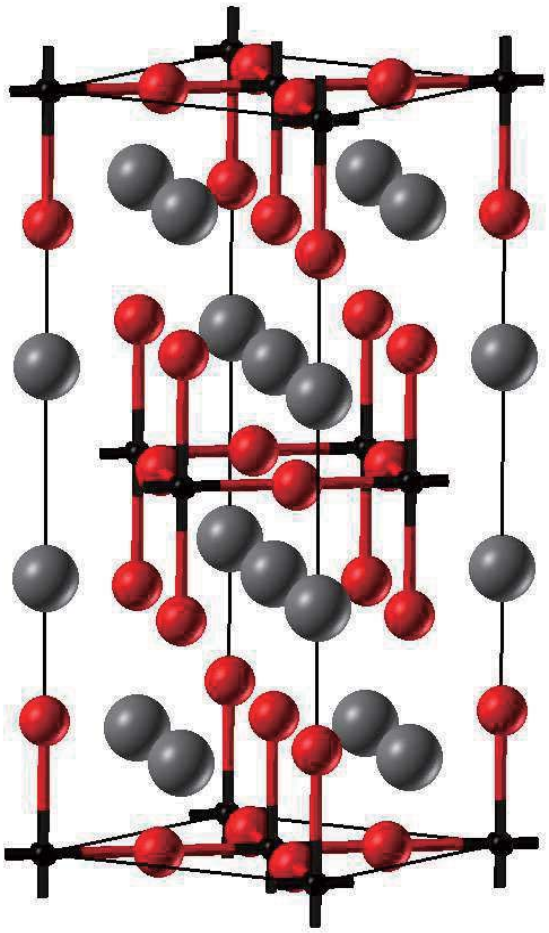


Figure 1.2: Illustration of a typical first order Ruddlesden-Popper structure; grey spheres are A site atoms, black spheres are B site atoms, and red spheres are oxygen atoms.

formula ($A_{n+1}B_nO_{3n+1}$; n = 1, 2, 3 ...). It is comprised of alternating Perovskite (ABO_3) and rock-salt (AO) layers. Based on this general formula, La_2NiO_4 is the first member of La-Ni-O RP series.

To fully utilize the potential of La_2NiO_4 as a promising cathode material for an intermediate temperature SOFC, its relevant properties must be well characterised and understood. These understandings might also suggest improvements on this particular structure to further enhance the performance as a SOFC cathode.

It is worth to note that much work on La_2NiO_4 was done in the 1990s, long before it was proposed to be a candidate for SOFC cathode application. The interest in La_2NiO_4 during that time was mainly due to its structural similarity to La_2CuO_4, which is a known high temperature ceramic superconductor. Therefore, both experimental and modelling efforts at that time have a quite different focus (mainly at cryogenic temperatures) compared to more recent works. Nonetheless, this knowledge still helps to understand this interesting material.

1.3.2 La_2NiO_4 structures

Significant amounts of high quality synchrotron x-ray and neutron powder diffraction work has been done to reveal the $La_2NiO_{4+\delta}$ crystal structure. These works covers a wide temperature range (1.5 K to 1073 K). The phase morphology and lattice parameters of $La_2NiO_{4+\delta}$ at various temperatures are summarised in Table 1.2.

Among the works quoted in Table 1.2, reference 23 measured powder samples with synchrotron x-ray diffraction; references 16,22,27 and 17 measured powder samples with neutron diffraction; reference 21 measured single crystal samples with neutron diffraction; references 24–26 measured powder samples with x-ray diffraction.

It is important to note that the tetragonal symmetry groups (I4/mmm) use a different primitive and crystallographical cell symmetry from the orthorhombic ones. Thus, there can be a significant apparent difference in the a and b lattice parameters. This apparent difference in lattice parameters will disappear once the lattice parameters are transformed to follow the

Table 1.2: Summary of phase morphology and lattice parameters of $La_2NiO_{4+\delta}$ at various temperature; a, b, c are three lattice parameters of the $La_2NiO_{4+\delta}$ structure. R.T. refers to room temperature with no additional in situ temperature control. LTT, RTO, HTT stands for low temperature tetragonal phase, room temperature orthorhomic phase and high temperature tetragonal phase respectively. Non-stoichiometric data is marked with * and noted as N.A. for phase information, as these non-stoichiometric cases are not parts of the ideal phase morphology.

Symmetry Group	a (Å)	b(Å)	c(Å)	Temperature (K)	Phase	Ref.
P42/ncm (138)	5.4995	5.4995	12.5052	1.5	LTT	17
	5.502	5.502	12.504	10	LTT	21
Bmab (64)	5.4419	5.5364	12.4896	120	RTO	17
	5.4618	5.4957	12.561	180	RTO	17
	5.4499	5.5275	12.5188	250	RTO	17
Bbcm (64)	5.4324	5.5277	12.488	R.T.	RTO	22
Fmmm (69)	5.46520	5.46869	12.67804	R.T.	RTO	23
I4/mmm (139)*	3.8690	3.8690	12.620	R.T.	N.A.	24
	3.8616	3.8616	12.6672	293	N.A.	25
	3.868	3.868	12.684	293	N.A.	26
Bbcm (64)	5.4656	5.5327	12.5547	295	RTO	16
Fmmm (69)	5.45869	5.46360	12.68524	298	RTO	27
I4/mmm (139)	3.8843	3.8843	12.7529	723	HTT	27
	3.9008	3.9008	12.7310	873	HTT	27
	3.9103	3.9103	12.7843	1073	HTT	27

same symmetry setup. The relationship between these two symmetry group representations is shown in Fig.1.4.

An illustration including all the three La_2NiO_4 phases is shown in Fig. 1.3. In this figure, we can see that only low temperature tetragonal phase La_2NiO_4 have significant tilting. The other two phases at higher temperatures do not have any significantly tilted NiO6 octahedra. For the LTT phase, a NiO6 octahedral's apical oxygen is tilted along an equatorial O-Ni-O direction, and all its 4 neighbouring NiO6 octahedra will tilt to the opposite direction.

Results showing a room-temperature I4/mmm symmetry group (indicated by '*' in Table1.2) are un-annealed oxygen-rich $La_2NiO_{4+\delta}$ species ($\delta > 0$) according to the literature[24–26]. As La_2NiO_4 readily absorbs oxygen during the synthesis process and when exposed to air, pure La_2NiO_4 must be characterised in a controlled atmosphere to prevent undesirable oxygen adsorption, especially at elevated temperatures. This also indicates that small hyperstoichiometry oxygen content could change the morphology of $La_2NiO_{4+\delta}$ from an orthorhombic phase to a tetragonal phase, without increase in temperature.

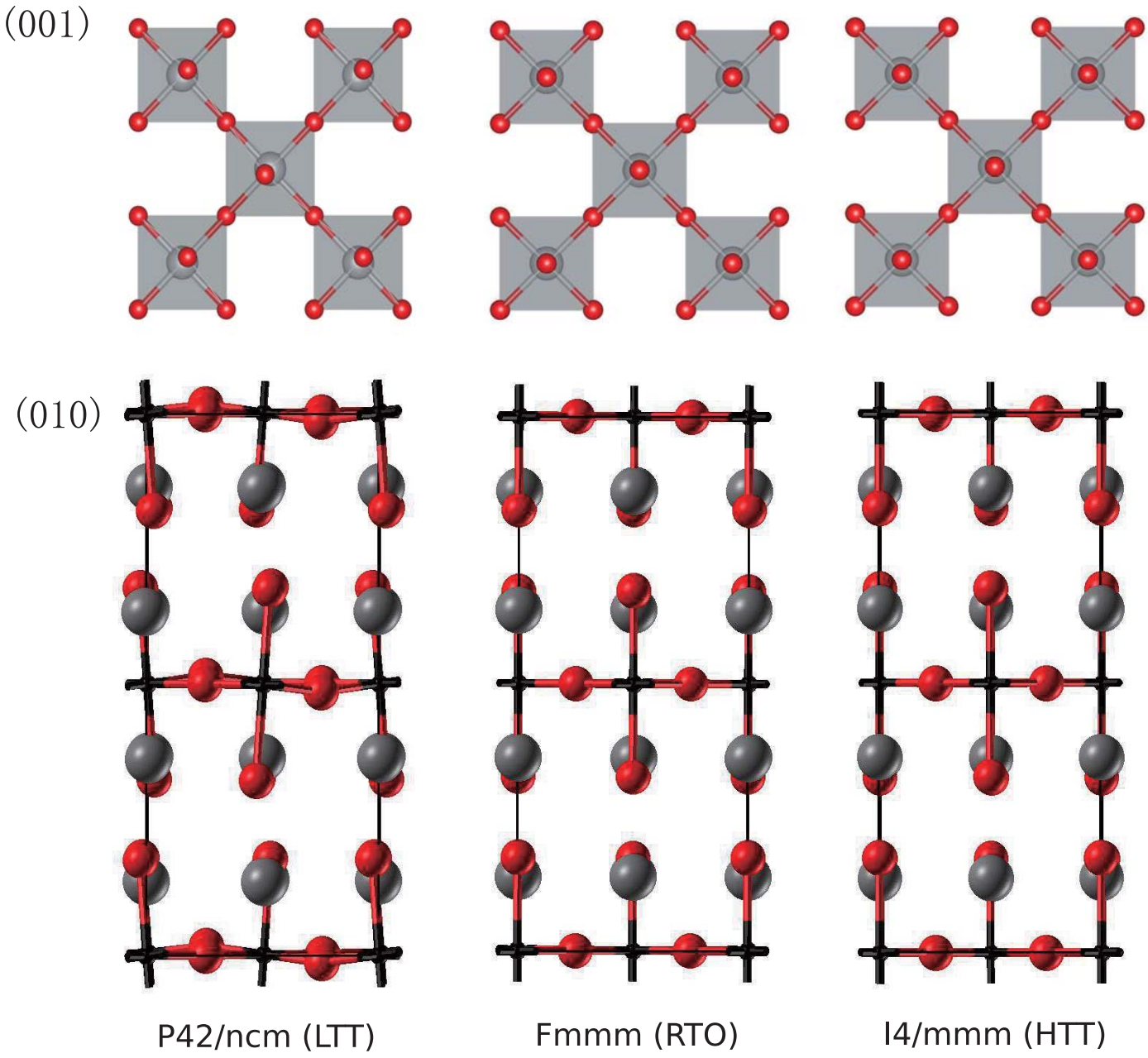


Figure 1.3: Illustration of the LTT (P42/ncm), RTO (Fmmm) and HTT (I4/mmm) La_2NiO_4 structures, produced with experimental crystallographical information reported in Table 1.2. Both (001) top views and (010) side views of the three phases are shown in this figure. In the (001) top view, the grey octahedra are NiO_6 octahedra and the grey spheres are Ni atoms. La atoms are omitted in the (001) top view for clarity. In the (010) side views, grey spheres are La atoms, red spheres are oxygen atoms, black spheres are Ni atoms. Tilting of the NiO6 octahedra can be seen clearly for the LTT phase.

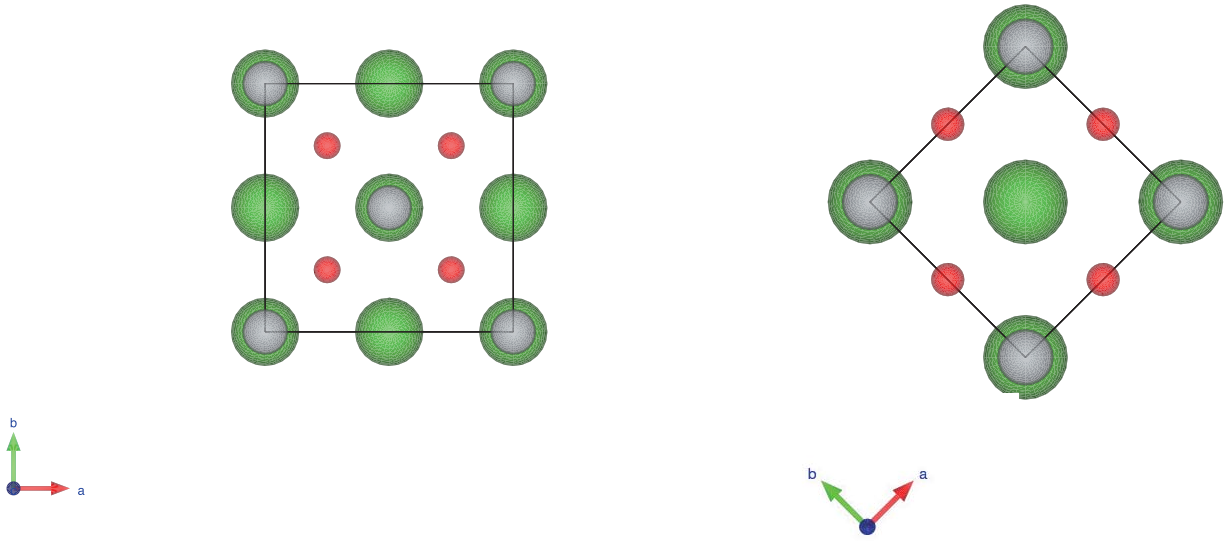


Figure 1.4: Illustration of the relationship between orthorhombic and tetragonal representations of $La_2NiO_{4+\delta}$. Left is othorhombic x-y plane. Right is tetragonal x-y plane. Ni atoms are grey; La atoms are green; O atoms are red.

Based on information in Table 1.2, La_2NiO_4 has three different phases at various temperatures, namely, low temperature tetragonal phase (LTT), room temperature orthorhombic phase (RTO) and high temperature tetragonal phase (HTT). Two phase transformations occur at about 80 K (from LTT to RTO) and 400 K (from RTO to HTT), according to Rodriguez's and Skinner's work respectively[17,27].

1.3.3 La_2NiO_4 magnetism

Magnetism related properties of La_2NiO_4 have been extensively investigated by both experimental and modelling works[17,21,28–33]. The magnetic spin configuration of $La_2NiO_{4+\delta}$ has been analyzed over a temperature range of 1.5 K to 600K with the neutron powder scattering technique. Results from these experiments suggest that stoichiometric La_2NiO_4 possesses a g_x mode antiferromagnetic structure[17,21,32], as depicted in Fig. 1.5. Density functional theory simulations done by Guo et al. agree with the experimentally observed magnetic structure[31].

As seen in Fig. 1.5, the g_x type antiferromagnetic setup consists of antiferromagnetically aligned atomic spins within the x-y plane. Each Ni atom is surrounded by nearest neighbouring Ni

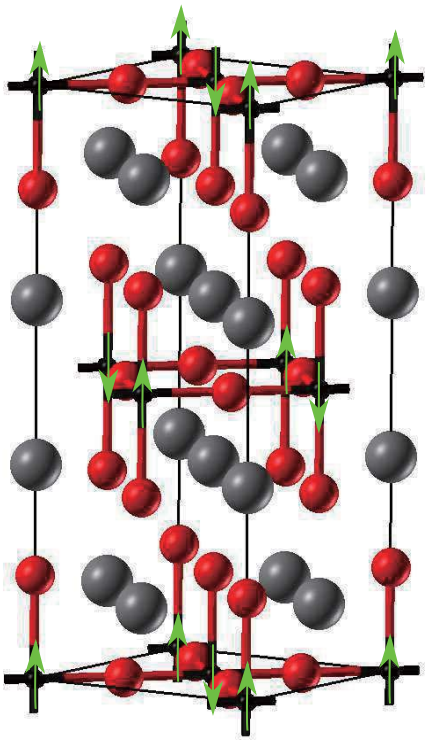


Figure 1.5: Illustration of the g_x magnetic spin configuration of pure La_2NiO_4[32]. The green arrows' directions indicate spin directions. The unit cell illustrated is the $1 \times 1 \times 1$ conventional crystallographic cell of La_2NiO_4. The top xy NiO_2 layer is linked to the bottom xy NiO_2 layer by translational symmetry and therefore these two layers are identical.

atoms with opposite spin. The top xy NiO_2 layer illustrated in this figure is related to the bottom xy NiO_2 layer by translational symmetry. Similar to the La_2CuO_4, the La_2NiO_4 is determined to be mainly a two-dimensional Heisenberg antiferromagnet and the inter-plane spin interaction is determined to be at least 10^{-4} smaller than the intra-plane spin interactions[29,34,35].

The Néel temperature of stoichiometric La_2NiO_4 was determined to be around 330K[17]. It was also reported that the magnetic properties of $La_2NiO_{4+\delta}$ are highly dependent on the amount of nonstoichiometrical oxygen content. Changing the nonstoichiometry coefficient δ by 0.05 could result in a shift of Néel temperature from 330K to 70K[17,32]. The strong dependency of $La_2NiO_{4+\delta}$ magnetic susceptibility and Néel temperature might be related to the changed oxidation state of Ni atoms during accommodation of extra oxygen. For every one extra oxygen ion accommodated in the $La_2NiO_{4+\delta}$ structure, two Ni^{2+} ions would turn into Ni^{3+} ions and lose one electron each. During this process, lone electrons on the two Ni^{3+} ions would increases from two to three. Depending on the position of these Ni^{3+} ions, they might significantly distort the magnetic configuration and hence affect the magnetic susceptibility and Néel temperature.

In another study done by Nakajima et al. , the Néel temperature of nonstoichiometric $La_2NiO_{4+\delta}$ was reported to vary in the range of ± 5 K for samples with identical composition but different thermal history[29].

The knowledge on $La_2NiO_{4+\delta}$ magnetism will be particularly useful in density functional simulation for this materials. Adopting the correct magnetic configuration will give more accurate modelling predictions when compared with experimental results.

1.3.4 Electronic and electrical properties of La_2NiO_4

The electronic and electrical properties of La_2NiO_4 have attracted significant attention both in the 1990s[30,36–39](in the search of new high temperature superconductors) and recently[13,38,40–42] (for application in SOFC cathodes). It is noted that no sign of superconductivity is observed even when the sample is cooled down to 1.5 K, despite the similarities between La_2NiO_4 and La_2CuO_4 (a well-known high temperature superconductor). At room temperature, La_2NiO_4

has a bandgap measured to be about 4 eV.[36] Hence, pure La_2NiO_4 is clearly an insulator at this temperature. By introducing oxygen intersitials, the band gap of $La_2NiO_{4+\delta}$ can be reduced to about 1.5 eV which is comparable to common semiconductors like GaAs.[43] The oxygen interstitials introduce extra low-lying acceptor levels and effectively convert $La_2NiO_{4+\delta}$ into a p-type semiconductor.[36]

Electrical conductivity of $La_2NiO_{4+\delta}$ over a temperature range of 293 K - 1200 K has been measured with *in situ* electrical impedance apparatus by several groups[13,38,40–42]. At room temperature, the electrical conductivity of $La_2NiO_{4+\delta}$ was reported to be around 45 Scm^{-1}. This total electrical conductivity is typical for a semiconductor. The electrical conductivity of $La_2NiO_{4+\delta}$ increases with temperature and reaches a peak value of about 70-90 Scm^{-1} at around 800 K (exact peak conductivity partially depending on the exact composition of the $La_2NiO_{4+\delta}$ sample). Beyond this temperature, its electrical conductivity gradually decreases. It is proposed that this trend is due to the combined effect of electronic conduction and ionic conduction in $La_2NiO_{4+\delta}$. Below 800 K, the increase of ionic conductivity due to rising temperature dominates and results in an increasing total electrical conductivity. Above 800 K, the reduction in electronic conductivity with temperature increase has the stronger influence and causes an overall decrease of electrical conductivity. In situ electrical impedance measurements under a controlled atmosphere also suggested dependence of electrical conductivity on oxygen partial pressure[38].

Direct experimental investigation of the oxygen ionic diffusion in $La_2NiO_{4+\delta}$ has been done by using the O^{18} isotope tracer exchange technique at elevated temperature (255 ^oC to 900 ^oC) for both dense ceramic and crystal samples[14,15]. The samples were investigated with focused ion beam - secondary ion mass spectroscopy (FIB-SIMS) to evaluate the diffusion depth profile of O^{18} in aforementioned experimental works. Later molecular dynamics simulation results agreed well with experimentally obatined oxygen diffusivity[12,19,44,45]. These modelling works suggested the main oxygen diffusion mechanism is oxygen interstitial diffusion. The atomistic diffusion pathway was also given in the simulation results.

It is noted that, while a number of modelling works computed the formation and migration

energy of oxygen defects[19,20,45–49],which related to the oxygen ionic conductivity, the energetic profile of the anion defects remains largely untouched[50].

1.3.5 Surface analysis of La_2NiO_4

As previously mentioned, surface analysis of La_2NiO_4, while important to the material performance as a SOFC cathode, is very limited both experimentally and from modelling. To the best of the author's knowledge, there is only one modelling work on the surface structure and termination of La_2NiO_4 by Read et al. using a molecular dynamics method[20]. In Read's work, only the low temperature tetragonal phase (described by the space group P42/ncm) was considered. His simulation results suggested that the (001) surface of La_2NiO_4 terminated with Ni sites has the lowest energy. Thus it is the most stable surface-termination on the (001) surfaces. However, these simulation results contradict Burriel's experimental findings presented in the group. Experimentally, $La_{2-x}Sr_xNiO_4$ single crystal samples prepared with the floating-zone technique (described in[51]) were analyzed with low energy ion scattering (LEIS), x-ray photoelectron spectroscopy (XPS) and X-ray crystal truncation rod techniques. The surfaces analyzed were confirmed to be (001) surfaces with surface x-ray diffraction. LEIS analysis, as a very surface sensitive technique, showed that instead of Ni termination, the (001) surfaces are terminated with A-site atoms (La and Sr). No significant Ni signal is detected on the (001) surface. XPS results on both as cleaved single crystal and heat treated samples are summarized in Table 1.3. The XPS results also support the LEIS findings: very little Ni was present in the near-surface layers compared to the bulk stoichiometry. In addition, the increased overall (La+Sr):Ni ratio after heat treatment suggested that Ni vacancies might be moving towards the (001) surfaces via a thermally activated process. This could also be related to the transformation between orthorhombic and tetragonal phases reported at ~400K[27], as the annealing temperature is well above this threshold. X-ray crystal truncation rod spectra fitting suggested that the near-surface region might undergo a structural reconstruction and was no longer a perfect Ruddlesden-Popper structure.

Besides the structural uncertainty in the La_2NiO_4(001) near-surface structure, the absence of

Table 1.3: (La+Sr):Ni ratio calculated from the fitted XPS spectra taken on the (001) surfaces at different angles as reported by Burriel. The heat treated sample were heated at 450°C for 72 hours in air.[1]

	(La+Sr):Ni	
Depth (nm)	As cleaved single crystal	Heat treated single crystal
0.6	5.34	6.71
1.8	8.50	5.51
3.5	6.50	5.21
4.8	3.93	4.35
5.9	3.44	4.60
6.6	3.09	4.73
6.9	2.32	4.50
bulk (theoretical)	2.00	2.00

Ni at the surface and deficiency near surface also raises another question. Unlike multiple-oxidation-state Ni ions (+2 and +3), La exhibits only one oxidation state (+3) in compound. The La^{3+} ions are unable to donate electrons for the reduction of oxygen gas to O^{2-} ions. While it is known that oxygen gas can reduce and permeate into La_2NiO_4 on the (001) surfaces[14], details of the oxygen reduction process on the La-terminated surface remain mysterious. It is proposed that the reduction of oxygen might be related to the highly defective surface structure, which could allow the oxygen gas molecules to interact with either the Ni atoms lying under the surface or the oxygen vacancies at the defective LaO surface.

1.4 Lattice Defects and Defect Notations

A perfect lattice is, as its name suggests, a lattice that contains no mismatch, vacancies and impurities. In reality, crystal lattices usually will contain some forms of defects. For solid state ionics applications, the defects are crucial as they will determine the ionic transportation properties. Most of the time, the defects, be they vacancies or interstitials, are the mobile species in the crystal lattice. Therefore, it is particularly important to understand and model defective lattices. To describe defects in a lattice efficiently, a set of notation named "Kröger-Vink notation" is used. An explanation of this notation is provided below.

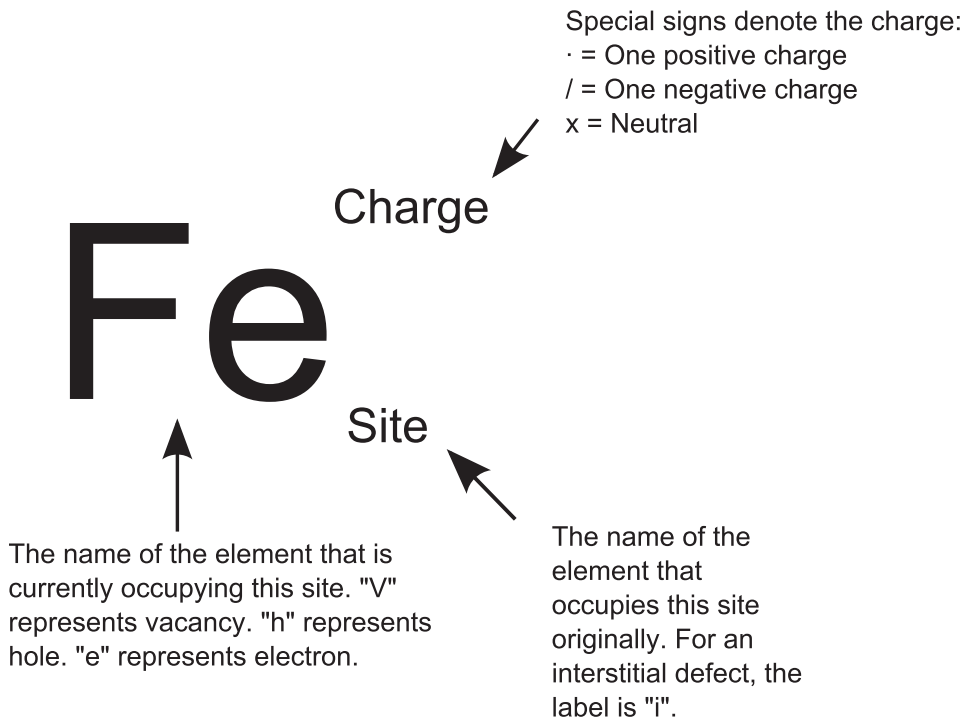


Figure 1.6: Illustration of the Kröger-Vink notation rules.[52]

1.4.1 Kröger-Vink Notation

The Kröger-Vink notation is named after its original proposers, Kröger and Vink[52]. This notation rule gives a convenient and elegant way to describe defects and defect processes. Fig. 1.6 shows the general notation rule of the Kröger-Vink notation. In the following sections, two of the most common defect processes, Schottky defects and Frenkel defects, are explained using the Kröger-Vink notation.

1.4.2 Schottky Defects

The Schottky defects involve the creation of lattice vacancies. In an ionic oxide, MO, if the M and O vacancies' sites are created in a stoichiometric ratio, then we say it is a Schottky defect process. The missing M and O ions will form MO again somewhere else. The Schottky defect process can be expressed in the Kröger-Vink notation, using CaO as an example, as in Eqn.

1.3.

$$\mathrm{Ca}_{\mathrm{Ca}}^{X} + \mathrm{O}_{\mathrm{O}}^{X} \rightarrow \mathrm{V}_{\mathrm{Ca}}^{''} + \mathrm{V}_{\mathrm{O}}^{\cdot\cdot} + \mathrm{CaO} \tag{1.3}$$

1.4.3 Frenkel Defects

The most common interstitial defect is the Frenkel defect, where an ion goes into an interstitial site and leaves a vacancy behind at its original lattice site. Taking CaO as an example again, its two possible Frenkel defect processes are shown in Eqns. 1.4 and 1.5, using the Kröger-Vink notation.

$$\mathrm{Ca}_{\mathrm{Ca}}^{X} \rightarrow \mathrm{Ca}_{\mathrm{i}}^{\cdot\cdot} + \mathrm{V}_{\mathrm{Ca}}^{''} \tag{1.4}$$

$$\mathrm{O}_{\mathrm{O}}^{X} \rightarrow \mathrm{O}_{\mathrm{i}}^{''} + \mathrm{V}_{\mathrm{O}}^{\cdot\cdot} \tag{1.5}$$

Chapter 2

Methodology

Computer-based materials simulation methods can be dated back to the 1940s, when modern Monte Carlo methods were invented and used in the Manhattan project. Later on, classical inter-atomic potential based methods and quantum mechanical electronic structure based methods were developed and became two groups of mainstream simulation methods till today. Thanks to the fast increase in computational power, materials simulation can now explore many interesting properties and difficult systems that were deemed not possible 20 years ago. The insights gained from simulation are valuable additions to experiments, especially in areas where direct experimental investigations are challenging or costly, e.g. surface processes or detailed diffusion pathways.

In this thesis, both classical molecular dynamics (MD) and quantum mechanical (QM) methods are employed to evaluate different properties of materials. The classical MD method excels at evaluating dynamic processes, while it only costs a small amount of computational resources. The QM method can give an accurate electronic structure description, but is too computationally expensive to be used for large systems or dynamic processes. In addition, empirical equilibrium thermodynamics is also used to aid the aforementioned methods. The empirical thermodynamic method, while not strictly a computer simulation method, provides a solid basic understanding of the target material's thermodynamic stabilities and can direct a clever usage of the computationally expensive QM method.

2.1 Equilibrium Thermodynamics

Equilibrium thermodynamics is a very powerful tool to evaluate the stability of phases and compute phase diagrams. It relies on classical thermodynamics and has its roots in the definition of the internal energy U, which can be defined by the Euler relation:

$$U = TS - PV + \sum_{k=1}^{r} \mu_k N_k \tag{2.1}$$

where P is pressure, V is volume, T is temperature, S is entropy, μ_k is the chemical potential of component k and N_k is the amount of component k. Using a partial Legendre transformation, two important thermodynamic quantities, the enthalpy (H) and the Gibbs energy (G), can be defined based on Eqn. 2.1:

$$H = U + PV \tag{2.2}$$

$$G = U + PV - TS \tag{2.3}$$

We can also express the enthalpy in its differential form:

$$\mathrm{d}H = T\mathrm{d}S + V\mathrm{d}P + \sum_{k=1}^{r} \mu_i \mathrm{d}N_i \tag{2.4}$$

It is easy to see that the heat absorbed by a fixed amount of material which causes a temperature increase T at constant pressure P is just the enthalpy. Therefore, the heat capacity c_P at constant pressure, which is the heat required for a mole of substance to increase its temperature by 1 Kelvin, is defined as

$$c_P = \left(\frac{\partial h}{\partial T}\right)_P = \left(T\frac{\partial s}{\partial T}\right)_P \tag{2.5}$$

where h is the molar enthalpy and s is the molar entropy.

The Gibbs energy G is a very useful function to describe equilibrium at constant temperature and pressure. Such a condition is very common in experiments. Combining Eqn. 2.3 and 2.1,

we can see that the molar Gibbs energy g is simply

$$g = \frac{G}{N} = \sum_{k=1}^{r} \mu_k x_k \tag{2.6}$$

where x_k is the molar fraction of component k. Consider the differential form of g and the definition of heat capacity c_P as in Eqn. 2.5 at constant pressure

$$\mathrm{d}g = -s\mathrm{d}T + v\mathrm{d}P \tag{2.7}$$

$$\left(\frac{\partial^2 g}{\partial T^2}\right) = -\left(\frac{\partial s}{\partial T}\right) = -\left(\frac{c_P}{T}\right) \tag{2.8}$$

Eqn. 2.8 has practical significance, as it links the Gibbs energy and chemical potential to an experimentally measurable quantity c_P. Detailed usage of this relationship is discussed later in this section.

At a given temperature, pressure and ratio of components, the total Gibbs energy of the system is the sum of the Gibbs formation energies of possible mixtures of the competing phases. The amount of the Gibbs formation energies contained in the sum is weighted by the amount of the corresponding phases. The mixture with the lowest total Gibbs energy will be the stable state of the system at the given condition. Therefore, the construction of the phase diagram, which summarizes the relationship between phases, can be calculated by comparing Gibbs energies of formation, ΔG_f^0, of the competing phases. The 0 in ΔG_f^0 stands for the standard condition which is 1 bar pressure and 298.15 K temperature. By definition, for an oxide phase with general formula $\mathrm{A_xO_y}$, its Gibbs formation energy can be expressed as:

$$\Delta G^0_{f\mathrm{A_xO_y}} = \mu_{\mathrm{A_xO_y}} - x\mu_A^0 - y\mu_O^0 \tag{2.9}$$

Assuming negligible entropic and volumetric contribution to the Gibbs energy, $\mu_{\mathrm{A_xO_y}}$ can be approximated using the unit ground state energy of $\mathrm{A_xO_y}$ calculated by density functional methods. Therefore, the determination of the respective standard chemical potential μ^0 will be crucial to the evaluation of Gibbs formation energy. The 'standard' refers to the standard condition: 298.15 K and 1 bar pressure.

The chemical potential μ^0 is calculated by combining the ground state DFT calculated μ (0K) and empirical oxygen gas chemical potential change due to temperature increase from the NIST database. Due to the limitation of certain DFT approximation's ability (e.g. the hybrid B3LYP functional) to predict a pure metal's chemical potential, an indirect determination of a metal's chemical potential must be used to avoid errors. The indirect method's details will be discussed in Chapter 3.

2.1.1 Gibbs phase rule

Suppose r components forms M different phases in equilibrium, where the phases are denoted as I, II, ... , M, what limits the number M at a given condition (specific temperature T, pressure P or fractional amounts of the components x_i)? A degree of freedom analysis can solve this problem. A Gibbs-Duhem equation can be written for each of the phases.

$$\begin{aligned} 0 &= S^I \mathrm{d}T - V^I \mathrm{d}P + \sum_{k=1}^{r} N_k^I \mathrm{d}\mu_k \\ &\vdots \\ 0 &= S^M \mathrm{d}T - V^M \mathrm{d}P + \sum_{k=1}^{r} N_k^M \mathrm{d}\mu_k \end{aligned}$$

It is easy to see that we have M equations for the M phases. In all these equations, there are $2 + r$ independent variables, where the 2 comes from T and P, and there are r μ_k terms. If a total number f of the variables are known among the $2 + r$ variables, the number of equations (M) required to solve for the unknown variables has the following relationship:

$$f = 2 + r - M \tag{2.10}$$

The above equation is the Gibbs phase rule. The f is also the degrees of freedom available when M phases are in equilibrium. This simple rule is very handy when determining the possible phases coexisting at a given condition or constructing phase diagrams.

2.1.2 Shomate equation

Shomate proposed an empirical equation to relate a phase's Gibbs energy $G^o(T)$ to temperature T.[53,54] It is the most widely used experimentally fitted general thermodynamic equation and has the form:

$$\Delta G^o(T) = G(T) - H^{SER} = a + bT + cT\ln(T) + \sum_n d_n T^n \tag{2.11}$$

where H^{SER} is the phases' Stable Element Reference of its constituent elements at 298.15 K and 1 bar, and the coefficients a, b, c and d_n are constants related to the material.

Using the relationship stated in Eqn. 2.8, the second derivative of $\Delta G^o(T)$ becomes:

$$c_P(T) = -c - \sum_n n(n-1)d_n T^{n-1} \tag{2.12}$$

where $c_P(T)$ is the heat capacity of the material, n is an integer and usually takes the values of 2 and -1. This derived form is especially useful, as the heat capacity can be easily measured using differential scanning calorimetry (DSC). Thus, by using the experimentally measurable heat capacity, the compound's Gibbs formation energy can be determined and employed to construct the related phase diagrams.

2.2 Classical Potential Simulations

A Born-Mayer potential is used to describe the interaction between atoms in the molecular dynamics simulations. In the model, the atoms are treated as point charges and an ionic lattice can be sufficiently described with the interactions between ion pairs (i and j) only. The total lattice energy $E_{lattice}$ is therefore the summation of the ion pairs' interactions (Φ_{ij} as a function of a particular ion pair i and j with a separation r_{ij}):

$$E_{lattice} = \sum_i \sum_{j>i} \Phi_{ij}(r_{ij}) \tag{2.13}$$

The ion pair interaction can be naturally separated into two parts; the long range Coulombic interaction (Φ_{LR}) and the short range interactions (Φ_{SR}) which comprise nucleus-nucleus interactions, electron cloud overlaps and van der Waals forces. Equation 2.13 can then be rewritten as:

$$E_{lattice} = \sum_i \sum_{j>i} (\Phi_{LR,ij}(r_{ij}) + \Phi_{SR,ij}(r_{ij})) \tag{2.14}$$

These two parts of the interaction are discussed in the following sections.

2.2.1 Coulombic Interaction

The ion pairs' long range interactions due to charges follow Coulomb's law. An ion pair's Coulombic energy can be written as:

$$\Phi_{LR}(r_{ij}) = \frac{q_i q_j}{4\pi\epsilon_0 r_{ij}} \tag{2.15}$$

where q_i and q_j are charges of ion i and j respectively, and ϵ_0 is the permittivity of free space.

When calculating the summation of the Coulombic interaction given above in an ionic lattice, it is quickly noticed that the Coulombic potential diminishes with $1/r_{ij}$ and converges slowly. Therefore it is impractical to do a direct summation. An alternative summation method proposed by Ewald can be used to alleviate this problem. The Ewald summation method exploits the properties of reciprocal space and Gaussian distribution functions to accelerate convergence of the sum. A complete description of the Ewald summation method is not within the scope of this thesis and can be found in many standard textbooks, e.g. Frenkel and Smit's 'Understanding Molecular Simulation'[55].

2.2.2 Short Range Interactions

The Coulombic interaction term in equation 2.15 accounts only for the long range interaction of all ion pairs' interactions. The Coulombic interaction approaches infinity when the ion pair separation approaches zero. Therefore, all ions will collapse into one point if only the Coulombic

term is present. This is clearly not physical. The short range term introduced in equation 2.14 must correct the infinite Coulombic attraction.

With the knowledge of quantum mechanics, it is known that a part of the strong short range repulsion is due to the Pauli Exclusion Principle. According to the Pauli Exclusion Principle, no two fermions (which electrons are) may occupy the same quantum state. Therefore, when the electron clouds of two ions overlap at close range, the ground state charge distribution must move to a higher energy state to allow more quantum states for electrons in the same space. The increased electronic energy exhibits as a repulsive force. Born and Mayer introduced the following equation to account for this repulsion with a spherical charge distribution assumption[56]:

$$\Phi_{SR}^{Born}(r_{ij}) = A_{ij}\exp(\frac{-r_{ij}}{\rho_{ij}}) \tag{2.16}$$

Where A_{ij} and ρ_{ij} are parameters specific to the ion species i and j.

In addition to the short range repulsion, a weak attractive force named van der Waal's force is also present at small to intermediate ionic separation. The van der Waals force originates from the instantaneously induced dipoles caused by electron density fluctuations.[57] Due to this nature, the van der Waals force is much more significant for large polarisable ions like oxygen. By considering the relationship between the instantaneous dipole and its induced dipole, London gives the expression of the attraction potential[58]:

$$\Phi_{SR}^{London}(r_{ij}) = -\frac{C_{ij}}{r_{ij}^6} \tag{2.17}$$

where C_{ij} is a parameter specific to the ion species i and j.

By combining the two short range interactions in equation 2.16 and 2.17, the two-body Buckingham potential is obtained[59]:

$$\Phi_{SR}(r_{ij}) = A_{ij}\exp(\frac{-r_{ij}}{\rho_{ij}}) - \frac{C_{ij}}{r_{ij}^6} \tag{2.18}$$

where A_{ij}, ρ_{ij} and C_{ij} are the potential parameters.

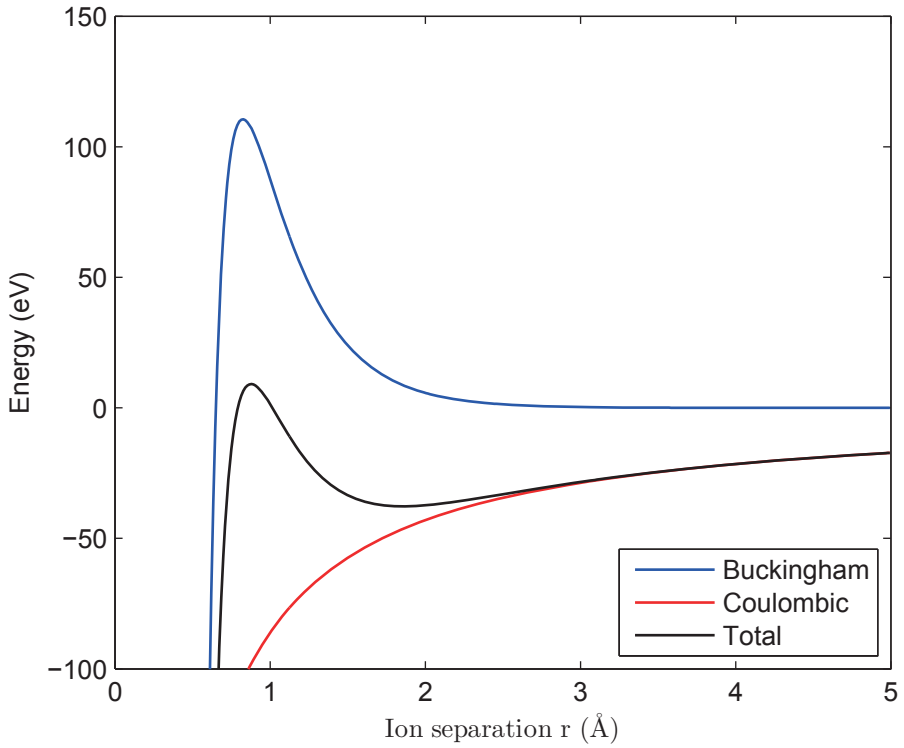


Figure 2.1: Comparison of total pair potential and its constituent long range Coulombic potential and short range Buckingham potential of an example ion pair.

It is noted, as shown in figure 2.1, the Buckingham potential will fail again at very short range due to the fast decrease of the $-\frac{C_{ij}}{r_{ij}^6}$ term. In reality, this failure only occurs for nuclear radiation studies where high energy collisions of atoms are common. This scenario is not applicable to this thesis and therefore will not be discussed in detail.

Combining the short range potential and the long range Coulombic potential, the total lattice energy, $E_{lattice}$, is given by:

$$E_{lattice} = \sum_i \sum_{j>i} \left(\frac{q_i q_j}{4\pi\epsilon_0 r_{ij}} + A_{ij} \exp\left(\frac{-r_{ij}}{\rho_{ij}}\right) - \frac{C_{ij}}{r_{ij}^6}\right) \tag{2.19}$$

2.2.3 Molecular Dynamics

The Molecular Dynamics (MD) method has its roots in Newtonian mechanics and Laplace's deterministic view of the physical world (popularly embodied in 'Laplace's demon'). This method evaluates the positions and velocities of an atom over a period of time using the initial

positions, velocities and descriptions of the interatomic forces. Thus, MD is an ideal choice to study a material's time and temperature related properties, e.g bulk diffusion of defects. These kinds of properties are particularly relevant for functional oxides used as ionic conductors.

In MD simulations, all ions follow Newton's second law:

$$\mathbf{F}_i = m_i \mathbf{a}_i \tag{2.20}$$

assuming mass is constant and relativistic effects are negligible, where t is time, m_i is the mass of ion i, $\mathbf{F}_i$ and $\mathbf{a}_i$ are the force exerted on i and acceleration of i respectively.

Knowing that the force exerted on ion i is directly related to its potential energy (Φ_i) and position ($\mathbf{r}_i$), Newton's second law can be expressed as:

$$-\frac{\partial \Phi_i}{\partial \mathbf{r}_i} = m_i \frac{\partial^2 \mathbf{r}_i}{\partial t_i^2} \tag{2.21}$$

In this case, the interatomic potential is the sum of long range Coulombic interactions and short range interactions as discussed in equation 2.15 and 2.18 respectively. By solving this equation, the positions and velocities of ion i are known, given its interatomic potential Φ_i. Unfortunately, it is impractical to solve equation 2.21 analytically due to the large amount of simultaneous interactions dependant on time. Therefore, the velocity Verlet method is used to solve the equation numerically[60]. By considering position and velocity change after a small timestep, δt, we have two equations:

$$\mathbf{r}_i(t + \delta t) = \mathbf{r}_i(t) + \delta t \mathbf{v}_i(t) + \frac{1}{2}\delta t^2 \mathbf{a}_i \tag{2.22}$$

$$\mathbf{v}_i(t + \delta t) = \mathbf{v}_i(t) + \frac{1}{2}\delta t[\mathbf{a}_i(t) + \mathbf{a}_i(t + \delta t)] \tag{2.23}$$

With these equations, the position and velocity of an atom i at $t + \delta t$ can be calculated accurately using the atom's position and velocity known at time t, as long as the timestep δt is small enough. By repeating the calculation for n timesteps, all snapshots of the atom's positions and velocities between time t and $t + n\delta t$ can be obtained. These snapshots provide

valuable insights of possible atomic diffusion pathways if there is any diffusion.

2.3 Quantum Mechanic Simulations

For simplicity and lucidity, atomic units are used throughout the sections related to the quantum mechanic simulations. In atomic units, the reduced Planck constant ($\hbar$ or $\frac{h}{2\pi}$), the mass of an electron (m_e) and the charge of an electron (e) are all set to 1.

2.3.1 Density Functional Theory

Density functional theory is a quantum mechanical modelling method used to investigate the ground state electronic structure of condensed matter. It uses a functional of electron density to compute properties of a many-electron system.

The Born-Oppenheimer approximation suggests that the nuclei in a system can be treated as stationary with respect to the electrons, as their masses and speeds are hugely different.[61] This approximation allows the separation of nuclear and electronic contributions to the Hamiltonian of the system. Under this approximation, the energy of a many-atom system can be described by the time independent, non-relativistic Schrödinger's equation:

$$\hat{H}\mathbf{\Psi}(\mathbf{r}_1, \mathbf{r}_2, ..., \mathbf{r}_N) = E\mathbf{\Psi}(\mathbf{r}_1, \mathbf{r}_2, ..., \mathbf{r}_N) \tag{2.24}$$

where E is the system's energy, Ψ, is the wavefunction, and the Hamiltonian operator, $\hat{H}$, consists of three terms: the electrons' kinetic energy, the interaction with the external potential (V_{ext}) and the electron-electron interaction (V_{ee}). In the context of the Born-Oppenheimer approximation, the relevant external potential is just the interaction between the electrons and the nuclei.

The theoretical foundation of DFT lies in the Hohenberg-Kohn theorems proved in 1964[62]. The first theorem is stated as "the electron density determines the external potential (to within an

additive constant)". Following this theorem, it is immediately deduced that the Hamiltonian operator can be determined solely by the electron density. Hence, the energy of a many-electron system can be described as a functional of electron density, $E[\rho]$. The second theorem states "for any positive definite trial electron density, ρ_t, such that $\int \rho_t(\mathbf{r})d\mathbf{r} = N$,there is $E[\rho_t] \geq E_0$". Therefore, ground state energy E_0 can be found by minimising the energy functional $E[\rho]$.

Based on the form of the Schrödinger's equation (Eqn.2.24) and Hamiltonian operator, the energy functional ($E[\rho]$) contains three terms: kinetic energy ($T[\rho]$), interaction with external potential ($V_{ext}[\rho]$) and electron-electron interaction($V_{ee}[\rho]$):

$$E[\rho] = T[\rho] + V_{ext}[\rho] + V_{ee}[\rho] \tag{2.25}$$

where

$$V_{ext}[\rho] = \int \hat{V}_{ext}(\mathbf{r})\rho(\mathbf{r})d\mathbf{r} \tag{2.26}$$

However, the forms of kinetic and electron interaction functionals are unknown. To approximate these two unknown functionals, Kohn and Sham introduced a fictitious system of N non-interacting electrons with the same density as the interacting system[63].This fictitious system can be described by a single determinant wavefunction formed from N molecular "orbitals" ϕ_i. In such a system, the kinetic energy is produced exactly as:

$$T_s[\rho] = -\frac{1}{2}\sum_{i}^{N}\langle\phi_i|\nabla^2|\phi_i\rangle \tag{2.27}$$

Note that $T_s[\rho]$ is different from the exact kinetic functional of an interacting system, $T[\rho]$.

It is also noted that a significant contribution (Hartree energy) in the electron-electron interaction comes from the classical Coulomb interaction:

$$V_H[\rho] = \frac{1}{2}\int \frac{\rho(\mathbf{r}_1)\rho(\mathbf{r}_2)}{|\mathbf{r}_1 - \mathbf{r}_2|}d\mathbf{r}_1\mathbf{r}_2 \tag{2.28}$$

Therefore, the energy functional can be rewritten as:

$$E[\rho] = T_s[\rho] + V_{ext}[\rho] + V_H[\rho] + E_{xc}[\rho] \tag{2.29}$$

and the exchange-correlation functional $E_{xc}[\rho]$ is simply:

$$E_{xc}[\rho] = (T[\rho] - T_s[\rho]) + (V_{ee}[\rho] - V_H[\rho]) \tag{2.30}$$

The exchange-correlation functional sums the errors associated with using a non-interacting kinetic energy and a classical treatment of electron-electron interactions. Considering the energy functional explicitly with respect to the electron density described by the orbitals, it is found that the orbitals giving minimised energy must satisfy the following equation:

$$[-\frac{1}{2}\nabla^2 + v_{ext}(\mathbf{r}) + \int \frac{\rho(\mathbf{r}')}{|\mathbf{r} - \mathbf{r}'|} d\mathbf{r}' + v_{xc}(\mathbf{r})]\phi_i(\mathbf{r}) = \varepsilon_i \phi_i(\mathbf{r}) \tag{2.31}$$

In this equation, a local potential v_{xc} is introduced. It is the functional derivative of the exchange-correlation term with respect to electron density:

$$v_{xc}(\mathbf{r}) = \frac{\delta E_{xc}[\rho]}{\delta \rho} \tag{2.32}$$

This set of equations are the Kohn-Sham equations. Practical calculation starts with an initial guess for the density, which produces a Kohn-Sham potential via Eqn.2.32. Then, a new density is found by solving the Kohn-Sham equations with the given potential. This cycle continues until the difference between the input and output densities is negligible. At this point, a self-consistent field is achieved.

2.3.2 Exchange-Correlation Approximation

In practice, the exchange correlation functional, $E_{xc}[\rho]$, is approximated. A number of methods have been proposed to achieve this. Common methods include the local density approximation

(LDA), the generalized gradient approximation (GGA) and the hybrid-exchange approximation.

LDA is the simplest approximation with the form:

$$E_{xc}[\rho] = \int \rho(\mathbf{r})\varepsilon_{xc}(\rho)d\mathbf{r} \tag{2.33}$$

In the LDA, $\varepsilon_{xc}(\rho)$ is a function of local charge density value only. It can be further seperated into exchange and correlation contributions:

$$\varepsilon_{xc}(\rho) = \varepsilon_x(\rho) + \varepsilon_c(\rho) \tag{2.34}$$

The exchange contribution is described by Dirac as $\varepsilon_x(\rho) = -C\rho^{1/3}$, with C, a constant determined from the homogeneous electron gas model; and the correlation contribution is first calculated using correlated electronic structure methods for the homogeneous electron gas and accurately parameterized[64]. LDA gives structural properties such as lattice parameter and elastic moduli in good agreement with respect to experiments. However, it generally has significant errors in calculation of energy differences, e.g. binding energy of molecules.

To obtain more accurate energetics, GGA, which includes dependence on the charge density gradient is usually used. The form of a GGA functional is:

$$E_{xc} = \int \rho(r)\varepsilon_{xc}(\rho, \nabla\rho)d\mathbf{r} \tag{2.35}$$

Several functionals under the GGA archetype have been developed[65–69]. Although GGA gives much better results in terms of energetics than the LDA, it still produces significant errors when describing strongly correlated materials. To overcome this, hybrid-exchange methods have been developed. It is the third approximation method described in this section.

The third commonly used approximation is a hybrid method that mixes a fraction of the exact Hartree-Fock exchange energy with an appropriate GGA functional. The general form of a

hybrid functional's exchange part is:

$$E_x = aE_{Fock} + bE_x^{GGA} \tag{2.36}$$

where the coefficients a and b are determined with reference to a system with a known exact result. One of the most commonly used hybrid functional is the Becke, three-parameter, Lee-Yang-Parr (B3LYP)[70] functional.

In this work, all density functional calculations are performed using the B3LYP[70] hybrid-exchange density functional, as implemented in the CRYSTAL09 and CRYSTAL14 software packages[71]. The B3LYP functional is well documented to provide accurate descriptions of localized and correlated systems (particularly for transition metal oxides like La_2NiO_4)[72–78]. Therefore, this functional is chosen to be adopted for this work.

2.3.3 Bloch's Theorem

A direct description and calculation of macroscopic amounts of material certainly exceed the capability of any available computer systems, as the total number of the orbitals is at the order of 10^{23} or more. Therefore, macroscopic lattices are approximated using a very small unit cell (usually 10s to 100s of atoms) with periodic boundary conditions (PBC) in DFT simulations. For DFT simulations, the PBC is simply:

$$\hat{V}_{ext}(\mathbf{r} + \mathbf{T}) = \hat{V}_{ext}(\mathbf{r}) \tag{2.37}$$

$$\rho(\mathbf{r} + \mathbf{T}) = \rho(\mathbf{r}) \tag{2.38}$$

where $\hat{V}_{ext}(\mathbf{r})$ and $\rho(\mathbf{r})$ are defined as the interaction with external potential at $\mathbf{r}$ and local electron density at $\mathbf{r}$, the same as in Eqn. 2.26. The periodic unit cell's translation is $\mathbf{T}$.

Unfortunately, the orbital wavefunction $\phi(\mathbf{r})$ is not periodic. Bloch's theorem solves the problem by expressing the wavefunction as a product of a periodic function ($u_{\mathbf{k}}(\mathbf{r})$) and a wave-like part

$(\exp(i\mathbf{k}\cdot\mathbf{r}))$ where k is a vector in reciprocal space (also called $\mathbf{k}$-space)[79]:

$$\phi_{\mathbf{k}}(\mathbf{r}) = \exp(i\mathbf{k}\cdot\mathbf{r})u_{\mathbf{k}}(\mathbf{r}) \tag{2.39}$$

so that

$$\phi_{\mathbf{k}}(\mathbf{r}+\mathbf{T}) = \exp(i\mathbf{k}\cdot\mathbf{T})\phi_{\mathbf{k}}(\mathbf{r}) \tag{2.40}$$

where the periodic function $(u_{\mathbf{k}}(\mathbf{r}))$ satisfies

$$u_{\mathbf{k}}(\mathbf{r}+\mathbf{T}) = u_{\mathbf{k}}(\mathbf{r}) \tag{2.41}$$

The function $u_{\mathbf{k}}(\mathbf{r})$ (named a Bloch function) is much easier for computer programmes to handle than the wavefunction $\phi(\mathbf{r})$. To exploit this feature, the kinetic energy term T_s and the electron density $\rho(\mathbf{r})$ can be expressed with $u_{\mathbf{k}}(\mathbf{r})$ too. Based on Eqn. 2.27, we have

$$T_s = \int_{BZ} \mathrm{d}\mathbf{k} \int_{UC} \mathrm{d}\mathbf{r}\, u^*_{\mathbf{k}}(\mathbf{r})(-i\nabla + \mathbf{k})^2 u_{\mathbf{k}}(\mathbf{r}) \tag{2.42}$$

where the first integral is over the Brillouin Zone (BZ, the equivalent of periodic unit cell in the reciprocal space), the second integral is over the unit cell (UC) in real space. For charge density $\rho(\mathbf{r})$, there is

$$\rho(\mathbf{r}) = \sum_N \int_{BZ} \mathrm{d}\mathbf{k}\, u^*_{N\mathbf{k}}(\mathbf{r}) u_{N\mathbf{k}}(\mathbf{r}) \tag{2.43}$$

where the integrals of all the occupied eigenstates N are summed. At this point, all the important property functions or functionals depend on cell-periodic functions, the Bloch function $u^*_{N\mathbf{k}}(\mathbf{r})$. For practical uses, a computer programme can just store this function for a single simulation cell in calculations.

The computation load for the DFT simulation can be further reduced by approximating the integral over the BZ with a sum over a set of discrete wavevectors in the BZ, $\sum_{\mathbf{k}}^{BZ}$ (also known as the "k-points"). The sampling criteria of the k-points follows the Monkhorst-Pack method, which creates a uniform grid for 3d integration.[80] The approximation's accuracy increases with the number of k-points used at the cost of more computational time. Since this method

approximates an integral in the reciprocal space and the volume of the first BZ is inversely proportional to the volume of the computational cell, calculations on larger real unit cells will require less k-points to achieve total energy and potential convergence. Only one k-point may be sufficient for some very large systems.

2.3.4 Basis Sets

Essentially, the DFT simulations are just solving the many-electron Schrödinger equations using approximations. Apart from the approximation methods themselves, another accuracy-determining factor is the quality of the orbital wavefunctions' descriptions. In a periodic solid crystal, elements can form various types of chemical bondings, from highly covalent to highly ionic, which results from different orbital overlaps. Therefore, an orbital description must be selected that enables the electron densities and the bondings to be correctly simulated in the calculations.

As discussed in the previous subsection, the wavefunctions stored in computers are expressed in the form of a product of a Bloch function ($u_{N\mathbf{k}}(\mathbf{r})$) and a wave-like part ($\exp(i\mathbf{k}\cdot\mathbf{r})$). Usually, the Bloch functions are represented with linearly combined function sets. Such function sets are called the basis sets. Its constituent functions are called basis functions. There are several types of basis sets currently in use. Each is named after the type of the basis functions in use, e.g. Gaussian basis sets, plane wave basis sets and augmented plan wave (APW) basis sets. In this thesis, the Gaussian basis sets are used, as they have good integration properties which can accelerate calculations with hybrid density functionals. Therefore, the discussions will be focused on the Gaussian basis sets used in this work.

The general form of a Gaussian basis function for a specific electronic shell is given as a linear combination (or 'contraction') of primitive Gaussian type functions (GTF), $g_j(\mathbf{r})$,

$$\phi_i(\mathbf{r}) = \sum_j d_j g_j(\mathbf{r}) \tag{2.44}$$

where d_j is the contraction coefficient. The function $g_j(\mathbf{r})$ takes the form:

$$g_j(\mathbf{r}) = N_{lm}(\alpha_j) r^l Y_{lm}(\theta, \phi) \exp(-\alpha_j r^2) \tag{2.45}$$

where l is the orbital quantum number, $N_{lm}(\alpha)$ is a normalization function, $Y_{lm}(\theta, \phi)$ is a spherical harmonic function and α_j is the contraction exponent. A suitable set of contraction coefficients and contraction exponents can lead to a basis function with desired properties, e.g. a 'cusp' at the origin or asymptotic behaviours, which the primitive GTF do not have. These properties are important features of the orbital wavefunctions. At the same time, efficient integration algorithms for GTFs can still be exploited to reduce computation time.

For relatively light elements, it is possible to create all-electron basis sets with Gaussian basis sets. However, for heavy element like La, an all-electron basis set creates too much of a burden for computer simulations. The alternative way is to approximate the core electrons' wavefunction using a small optimized pseudopotential. It is also easy to embed the relativistic effects of the core electrons into the pseudopotential. Although the usage of pseudopotentials can significantly reduce computational time, it will also cause errors in the results. This is particularly relevant for first-row transition metals with unfilled 3d orbitals like Ni. The interactions between these metals' 3d electrons and the core electrons are strong. These interactions are not captured with a simple core pseudopotential.

The developers of the CRYSTAL package maintain a library of basis sets for different elements. Many of them have stood the test of time and give reliable simulation results. Therefore, the basis sets used in the thesis are taken from this library. All the basis sets selected have been tuned for solid ionic crystals and proven in the literature.[73–75] The Ni and O basis sets taken are triple-valence all-electron basis sets. A Ni atom is described by a 28-411d(41) contraction (one s, four sp, and two d shells). An O atom is described by an 8-411d(1) contraction (one s, three sp, and one d shells). The most diffuse sp(d) exponents are $\alpha_{Ni} = 0.6144(0.411)\text{bohrs}^{-2}$ and $\alpha_O = 0.1843(0.6)\text{bohrs}^{-2}$.[71] The La core electrons are described with a pseudopotential, which is adapted from Dolg *et al.*'s quasirelativistic La pseudopotential[81]. However, the La valence basis sets in the library only contains s, p and d shells. The literature basis func-

tions are 411p(411)d(311) contracted sets (three s, three p and three d) with the most diffuse exponent being $\alpha_{La} = 0.15\text{bohrs}^{-2}$ for each s, p, d shell.[73] The basis functions for the La f-orbitals are omitted due to the limitations of earlier versions of the CRYSTAL package. The f-orbital basis functions are support in the CRYSTAL09 and CRYSTAL14 packages used in this thesis. Therefore, a brief tuning of the La f-orbital basis functions for La_2NiO_4 is done. A 411p(411)d(311)f(11) basis set is constructed for La. The most diffuse f-orbital basis function's exponent is kept at $\alpha_{La} = 0.15\text{bohrs}^{-2}$. The other f-orbital basis function's exponent is tuned for La_2NiO_4. A set of SCF-only calculations with a series of varied f-orbital contraction exponents is carried out for the La_2NiO_4 material. The input unit cell for testing contains 28 atoms (4 units of La_2NiO_4) and is fully optimised using the aforementioned literature La basis set. The change in total energy per unit La_2NiO_4 with respect to the reference state is calculated for each of the f-orbital parameters. The reference state is selected to be the total energy per unit La_2NiO_4 of the same input lattice optimised using literature La basis sets. A plot of the changes in total energy per unit La_2NiO_4 versus f-orbital parameters is shown in Fig. 2.2. According to the plot, the total energy minimum is achieved when the exponent of the f-orbital's GTF is 0.5. At this point, the energy change per unit La_2NiO_4 is -0.55 eV. The La_2NiO_4 structure and two other La-Ni-O RP materials ($La_3Ni_2O_7$ and $La_4Ni_3O_{10}$) are then optimised again using the new La basis sets with f-orbital included. A comparison of the lattice parameters optimised with new basis sets, optimised with literature basis sets and obtained from experiments are summarised in Table 2.1. Combining the results from Fig. 2.2 and Table 2.1, it is sufficient to say that the new La basis sets give improved results for La_2NiO_4 relatively to the old La basis sets, as the new basis sets give a more energetically stable lattice and reflect the experimental structure better. The improvements due to the new La basis sets are also generally true for other associated La-based RP materials, especially in the lattice z-axis. Therefore, the improved La basis sets are employed for the rest of this thesis.

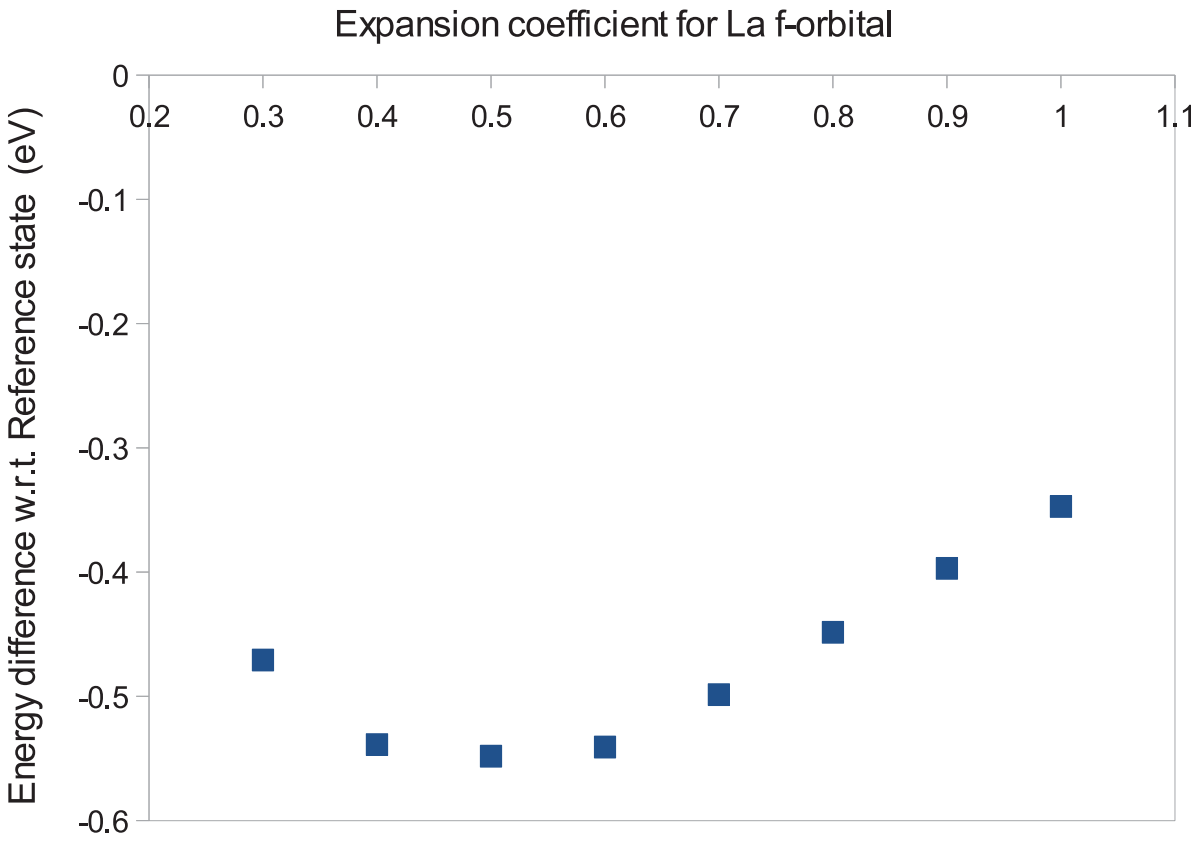


Figure 2.2: Change in the energy differences between the SCF test runs with respect to the reference energy state in eV. The reference energy is the input La_2NiO_4 structure's SCF total energy computed using literature La basis sets. Only the exponent of the primitive Gaussian type function (GTF) for the La f-orbital is altered between the runs.

Table 2.1: Comparison of calculated and experimental lattice parameters of relevant La-Ni-O RP materials. Expt. is experimental structure, and Calc. is calculated structure. Old basis sets refer to the literature La basis sets which La f-orbital is not included. New basis sets refer to the La basis sets with tuned f-orbital from this work. All literature experimental structures are measured at 298K.

Compound		a (Å)	b (Å)	c (Å)	Ref.
La_2NiO_4	Expt.	5.459	5.464	12.685	27
Old basis sets	Calc.	5.544(4)	5.546(3)	12.831(1)	
	Error	1.57%	1.51%	1.15%	
New basis sets	Calc.	5.538(8)	5.539(3)	12.752(2)	
	Error	1.47%	1.39%	0.52%	
$La_3Ni_2O_7$	Expt.	5.397	5.450	20.507	82
Old basis sets	Calc.	5.446(2)	5.584(0)	20.948(8)	
	Error	0.91%	2.46%	2.15%	
New basis sets	Calc.	5.435(0)	5.586(1)	20.868(3)	
	Error	0.70%	2.49%	1.76%	
$La_4Ni_3O_{10}$	Expt.	5.413	5.462	27.960	82
Old basis sets	Calc.	5.458(3)	5.574(0)	28.746(6)	
	Error	0.83%	2.05%	2.81%	
New basis sets	Calc.	5.448(3)	5.570(8)	28.512(2)	
	Error	0.65%	1.99%	1.97%	

2.4 Defect Energy Calculation

Defect energies are particularly relevant to the evaluation of functional oxides used in a SOFC, as the ionic conductivity (a key performance indicator) is related to the density of the defects. If the defect formation energy is small, it is more likely for the ionic defect to form and thus a higher defect density can be achieved.

To calculate the defect formation energy, two different approaches are used for the DFT simulation and classical mechanic simulation. The supercell method[83] is used for the DFT simulation, and the Mott-Littleton approximation[84] is used for the classical mechanic simulation.

2.4.1 Supercell Method

The supercell method puts the defect in a supercell of the original crystal lattice. The supercell consists of a few repeats of the primitive unit cells. Take an example of a defective cell containing one oxygen interstitial atom. By calculating the minimized ideal supercell energy (E_{ideal}), the

minimized defective supercell energy (E_{def}) and the chemical potential of the oxygen (μ_O), the defect formation energy (E^f_{def}) can be given as:

$$E^f_{def} = E_{def} - E_{ideal} - \mu_O \tag{2.46}$$

As periodic boundary conditions are used for the DFT simulation, the defect would interact with defects in neighbouring cells. This may results in an inappropriate inclusion of defect self-interaction energy. By using a large enough supercell, this effect can be made small enough to be neglected. However, a large supercell will also lead to a significant increase of computation time for DFT simulation. Therefore, a balance between accuracy and efficiency must be considered.

2.4.2 Mott-Littleton Approximation

The Mott-Littleton method, named after its developers, addresses the defect self-interaction problem while assessing a defective system. The method divides the lattice into two regions; the inner region I which contains the defect and the outer region II which is the rest of the lattice, as shown in figure 2.3. The defective lattice energy (E_{def}), is given as:

$$E_{def} = E_I + E_{I-II} + E_{II} \tag{2.47}$$

where E_I is the total ionic interaction energy in region I, E_{II} is the total ionic interaction in region II and E_{I-II} is the interaction energy between region I and region II.

The energy of region I (E_I) is explicitly calculated and minimized for all ions. Region I is defined as a sphere centred on the defect and includes all ions within. The size of region I is defined based on the convergence of the defect energy with respect to region I radius increase.

Region II is further divided into region IIa and region IIb, where region IIb is treated as a continuum region and in which we only consider the polarising effect of the defects. Region IIa is treated as a transition between region I and region IIb. Unlike region IIb, where ion displacements are not considered, the ions in region IIa are displaced from their original sites

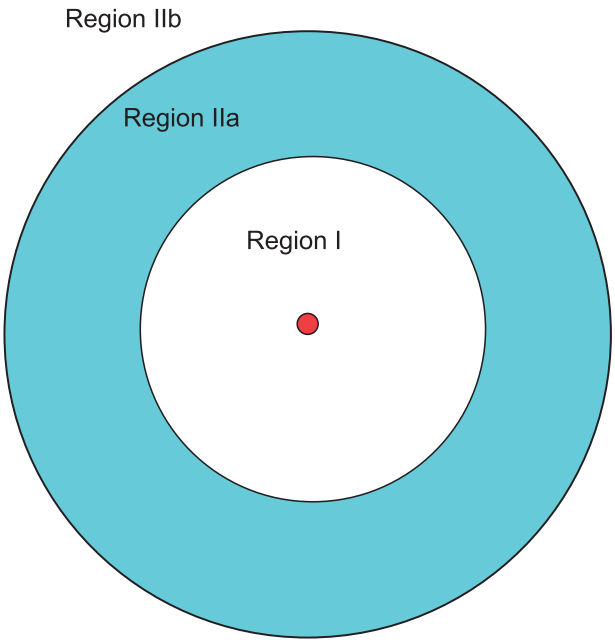


Figure 2.3: Schematic representation of the regions considered in the Mott-Littleton method. Region I contains the defect and is calculated explicitly. In region IIa, ions are displaced based on the polarisation effects of the defects. The interactions between the region I ions and region IIa ions are still calculated explicitly. Region IIb includes the rest of the bulk lattice and extends to infinity.

according to the defect's polarisation ($\mathbf{P}$) at distance $\mathbf{r}$ from the defect.[84] The polarisation is given as:

$$\mathbf{P} = \frac{q\mathbf{r}}{4\pi r^3}(1 - \frac{1}{\epsilon}) \tag{2.48}$$

where q is the charge of the defect and ϵ is the static dielectric constant of the lattice. The interaction energies between region I ions and region IIa ions (E_{I-II}) are still calculated explicitly. Such an approach is only valid if the perturbations due to the defect are small. In addition, the original ideal bulk lattice is fully relaxed and optimised before adding the defect.

The defect formation energy (E^f_{def}) is then given as:

$$E^f_{def} = E_{def} - E_{ideal} + E_\infty \tag{2.49}$$

where E_{ideal} is the energy of the ideal lattice and E_∞ is the potential of the defect species at infinity.

A careful selection of the regions' sizes is the key to a successful application of this method.

The explicitly calculated region I must be selected large enough to achieve accuracy, but not too large to damage computational efficiency. Usually, the selection process can be done by doing a set of pilot runs with increasing region I radius. The radius which the defect energy converges with respect to the increase of region I radius is selected.

2.5 Surfaces

Surfaces and interfaces are vitally important for materials' performances as SOFC electrodes. Most oxygen reduction and exchange processes happen on the surface. For a porous SOFC electrode, the surface exchange is usually the rate-determining process during operation. Thus, the surface exchange coefficient k, is one of the most critical performance factors for SOFC electrode materials. Unfortunately, surface processes are difficult to investigate in experiments due to the surface's sensitivity to its surrounding environments and past thermal history. It is difficult to find a common standard for sample preparations and measurements so that all experimental results are consistently comparable. Computational studies on the surface, while not easy, can be standardized to give important insights on how the surfaces might morph and react to its surroundings. The predictions of surface simulation studies can be compared to advanced experimental results to reveal important reactions associated with surface degradation or transformation.

A surface is created when a crystal lattice is cleaved. The surface exposed by cleaving has a thermodynamic penalty associated with it. This thermodynamic energy is named the surface energy ΔE_s and defined as:

$$\Delta E_s = \frac{E_{surf} - E_{ideal}}{A} \tag{2.50}$$

where E_{surf} is the total energy of the lattice with surface exposed, E_{ideal} is the total energy of the same lattice with no surfaces and A is the surface area.

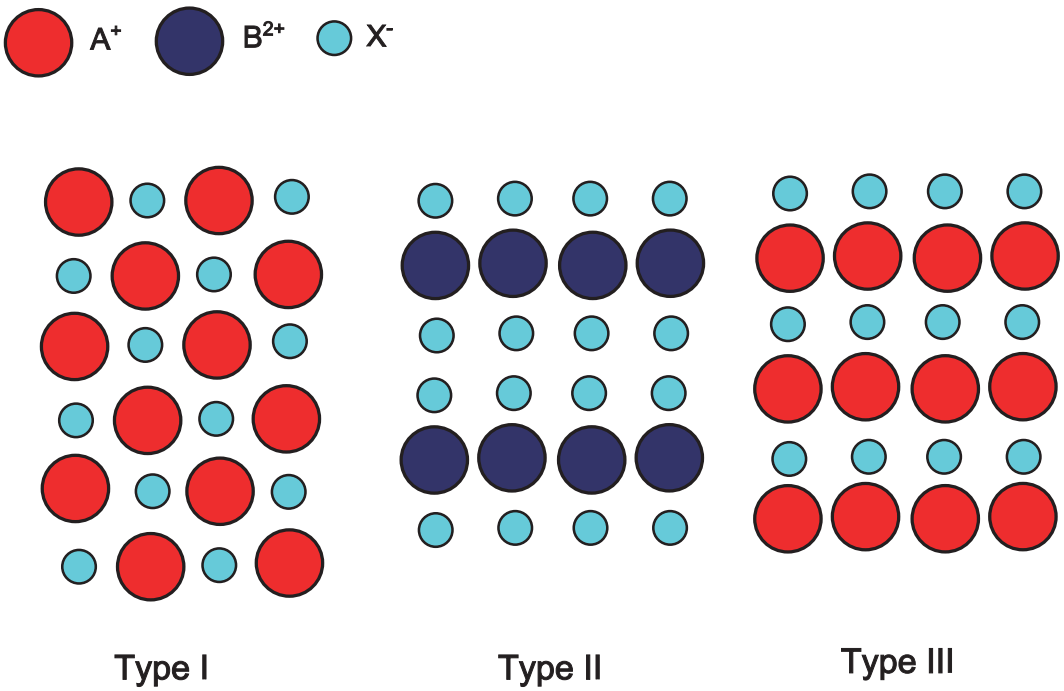


Figure 2.4: Three types of Tasker's surfaces for ionic solids. From left to right: Type I, Type II and Type III

2.5.1 Types of Surfaces

In 1979, Tasker proposed a classification of surfaces according to the surface's perpendicular dipoles.[85] This classification is particularly useful for studying ionic functional oxides' surfaces. Tasker categorizes ionic surfaces into three types, as shown in figure 2.4. For a type I surface, each of the layers in the crystal is charge neutral and incurs no dipole moments across the crystal. For a type II surface, charged ionic layers form a series of neutral repeating units and incur zero dipole perpendicular to the surface. A type III surface has charged planes and a resulting perpendicular dipole with respect to the surface. The type I and type II surfaces are considered to be stable and usually have small surface energies. On the other hand, the type III surface is destabilised by the large dipole due to the charged planes and requires significant surface reconstruction to achieve a stable state. Common stabilising reconstructions include incorporation of vacancies or extra external ions (usually O_2^- or OH^-) at the surface to counter the dipole moment.

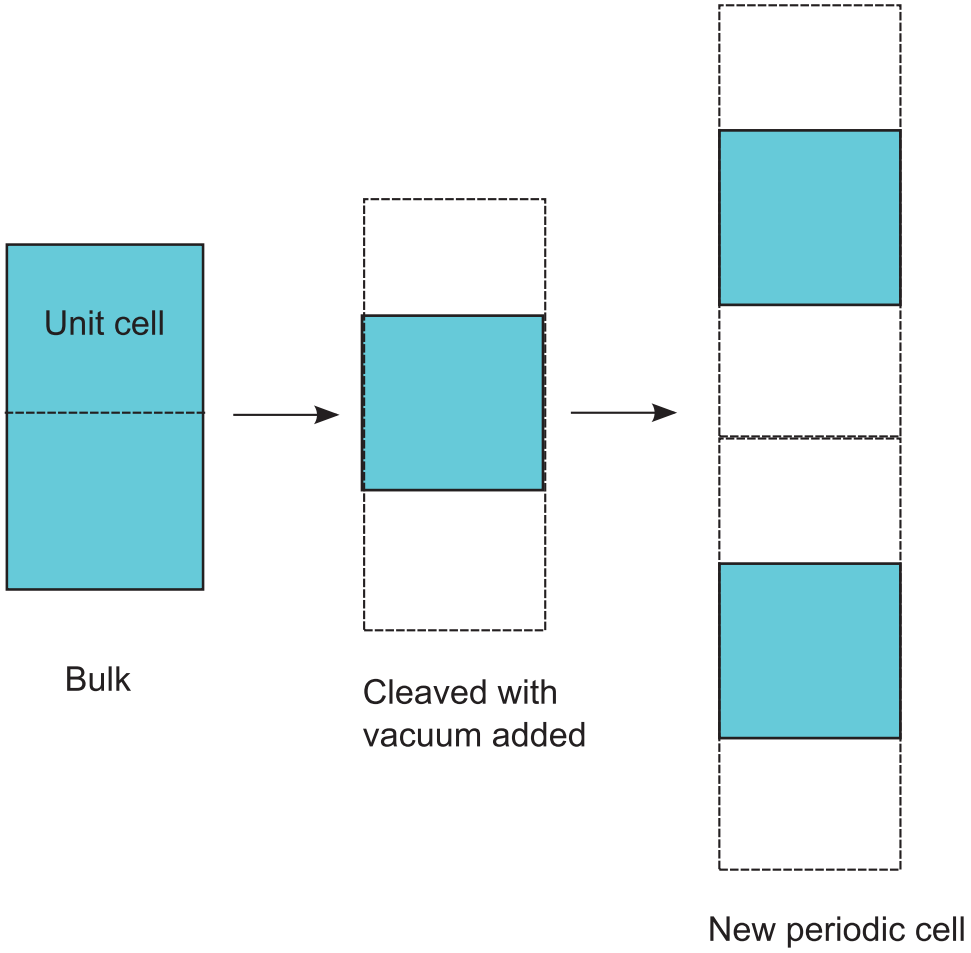


Figure 2.5: Schematic representation of the surface evaluation method.

2.5.2 Simulating Surfaces

All the previous simulation methods used periodic boundary conditions or infinitely filled spaces, while a crystal with surfaces exposed does not satisfy the periodic boundary condition at the surfaces obviously. One way to get around the problem is to treat surfaces as a huge continuous vacancy defect (or a vacuum). The perfect lattice is cleaved at desired surface planes to create a slab. Then a void is added on both sides of the slab and the void-slab composite is used as the input structure, as shown in figure 2.5. Under periodic boundary condition, the neighbouring slabs are effectively separated by the vacuum. The vacuum must be large enough to prevent interaction between the slabs. The slabs themselves should also be large enough to minimize interaction between the atoms on the opposite site of the same slab.

Chapter 3

LNO214: the surface mystery

Part of this work has been published and reprinted with permission from Ji Wu, Stevin S Pramana, Stephen J Skinner, John A Kilner, and Andrew P Horsfield. Why Ni Is Absent from the Surface of La 2 NiO 4+δ. J. Mater. Chem. A (2015): 2376023767. doi:10.1039/C5TA03759J. Copyright 2015 Royal Society of Chemistry.

3.1 Introduction

The Ruddlesden-Popper (RP) structured lanthanum nickelates (general formula $A_{n+1}B_nO_{3n+1}$), including La_2NiO_4 (LNO214), $La_3Ni_2O_7$ (LNO327) and $La_4Ni_3O_{10}$ (LNO4310), have attracted much interest in the past decade as potential novel cathode materials for intermediate temperature solid oxide fuel cells (IT-SOFC) operating at 600-800°C[12–15,19,27]. Among them, LNO214 deserves particular attention. Undoped LNO214 exhibits a decent mixed ionic and electronic conductivity (55-65 Scm^{-1} overall at 500-750°C)[86]. Comparing to the state-of-the-art IT-SOFC cathode materials, e.g. $La_{1-x}Sr_xCoO_{3-\delta}$(LSC) and $La_{0.6}Sr_{0.4}Fe_{0.2}Co_{0.8}O_{3-\delta}$ (LSCF), the LNO214 material does not possess a higher total electrical conductivity or oxygen self-diffusion coefficient at 500-750°C. However, both the LSC and the LSCF materials suffer from severe performance degradation over time (typically 0.05% efficiency loss per hour), which is believed to be due to the Sr-segregation.[86–88] The LNO214 material, being undoped, avoids this problem

and has advantages considering long-term stability and cost-effectiveness.

As a cathode material for IT-SOFC, two performance factors are of vital importance: the oxygen surface exchange coefficient, k, and the oxygen self diffusion coefficient, D. For LNO214, its bulk oxygen ion diffusion mechanism, which decides D, is understood well through both simulations[19] and experiments[15,27]. However, its surface structure and chemistry, which strongly affect the oxygen surface exchange coefficient, k, have not been explored in detail. Read *et al.* evaluated the LNO214 surfaces with static molecular mechanics and suggested that the Ni-terminated surfaces have lowest energies. According to them, the Ni sites should be exposed. The conventional oxygen adsorption/reduction mechanism also requires transition metal atoms like Ni to be exposed and directly involved to allow electron transfer. Zhou *et al.*[89] studied the oxygen adsorption/reduction mechanism at the exposed Ni sites based on Read's surface. More recently, with the development of the highly surface sensitive low energy ion scattering (LEIS) technique, a series of LEIS characterisation work on similar RP structured materials, including $La_2NiO_{4+\delta}$, $La_{2-x}Sr_xNiO_{4+\delta}$ (LSNO) and $PrLaNiO_{4+\delta}$ (PLNO), has revealed that these surfaces do not contain any detectable exposed Ni sites. Instead of exposing Ni ions, these surfaces are terminated with A-site cations (La, Sr, Pr).[1–3] These findings contradict earlier simulation results and pose questions about the morphology of the LNO214 surfaces and its related oxygen chemistry. On the other hand, depth profiling with focused ion beam secondary ion mass spectrometry (FIB-SIMS) on $La_2NiO_{4+\delta}$ and $La_{2-x}Sr_xNiO_{4+\delta}$ revealed a significant deviation from the stoichiometric Ni:La (or Ni:(La+Sr) for $La_{2-x}Sr_xNiO_{4+\delta}$) values down to about 10 nm.[1,3] Nonetheless, an earlier work on long term thermal degradation of LNO214 observed layers of LNO327 or LNO4310 on the LNO214 surface under transmission electron microscope (TEM), after two weeks heating at 1273K.[90] These two findings challenge our previous knowledge and assumptions of the LNO214 surface. The once thought-to-be resolved LNO214 surface becomes mysterious again. In this work, a number of theoretical methods, including the density functional theory (DFT) and classical thermodynamics, are used to explore different aspects of the LNO214 surface. A hypothesis is proposed to explain the experimental observations on the LNO214 surface.

3.2 The LNO214 surface energy

When studying the surface of a material, the first thing that comes into mind is usually the material's surface energy. For our revisit to the mysterious LNO214 surface, a natural starting point is to re-evaluate the surface energies associated with different possible LNO214 terminations and to compare them with literature values. A quick look at the LNO214 terminations along the common low lying orientations suggest that only the (001) terminations may present Ni only or La only surfaces. The (010) or (100) surfaces will always contain a mixture of La and Ni atoms. Druce *et al.*'s findings also suggest a (001) surface with only La observable[2,3]. We also believe that the surface energies and the surface terminations of LNO214's room temperature phase is more relevant to this material's application in the SOFC systems, as the SOFC systems work at intermediate to high temperature (LNO214 maintains its room temperature phase until about 723 K[27]). Most of the experimental observations are done at room temperature or higher too. Therefore, we decide to focus our study on the room temperature phase's (001) surfaces.

As detailed in Chapter 2, Tasker proposed that material surfaces can be classified into three types depending on the perpendicular dipoles associated with the studied surface[85]. In the case of LNO214, its room temperature Fmmm phase can have three kinds of distinctive surface terminations along the [001] direction. Three kind of slabs can be created by cleaving at these three terminations as shown in Fig. 3.1. These terminations are labelled as NiO2, LaOOLa and LaO respectively as shown in the figure. In Fig. 3.1, the charge from each layer and the accumulated charges which are summed from the top layer to each of the layers are also calculated and listed. It is important to notice that the NiO2 and the LaOOLa slabs shown in Fig. 3.1 are not stoichiometric as the surface layers are added to both sides of the slab. Therefore these slabs are not charge-neutral and so are unstable. If stoichiometry and charge neutrality are maintained, the NiO2 and the LaOOLa surfaces would always come together. This kind of termination is labelled as NiO/LaOOLa, as shown in Fig. 3.1. According to the charges calculated, the NiO/LaOOLa termination can be classified as Tasker's Type 3 surfaces as they have perpendicular dipoles along the [001] direction. On the other hand, the

NiO2			LaOOLa			NiO2/LaOOLa			LaO		
Comp.	Charge	Total Charge	Comp.	Charge	Total Charge	Comp.	Charge	Total Charge	Comp.	Charge	Total Charge
NiO2	(-2)	-2	LaO	(+1)	+1	NiO2	(-2)	-2	LaO	(+1)	+1
LaO	(+1)	-1	LaO	(+1)	+2	LaO	(+1)	-1	NiO2	(-2)	-1
LaO	(+1)	0	NiO2	(-2)	0	LaO	(+1)	0	LaO	(+1)	0
NiO2	(-2)	-2	LaO	(+1)	+1	NiO2	(-2)	-2	LaO	(+1)	+1
LaO	(+1)	-1	LaO	(+1)	+2	LaO	(+1)	-1	NiO2	(-2)	-1
LaO	(+1)	0	NiO2	(-2)	0	LaO	(+1)	0	LaO	(+1)	0
NiO2	(-2)	-2	LaO	(+1)	+1						
			LaO	(+1)	+2						

Figure 3.1: LNO214 slabs cleaved at different terminations along the [001] direction. These different terminations are named as NiO2, LaOOLa, NiO/LaOOLa and LaO respectively as shown. The charge listed in the bracket is the total charge of that particular layer. The total charge listed is the charge accumulated by summing the charges from that particular layer and all layers above up to the top surface layer.

LaO surface's perpendicular dipole along the [001] direction is cancelled and can be classified as Tasker's Type 2 surface. According to Tasker, his Type 3 surfaces are not stable due to the dipole moments and will need stabilization via other mechanisms like the introduction of extra defects or charge re-distribution among the atoms[85]. This analysis suggests that the Ni-terminated (001) surface is not stable unless some stabilization mechanisms are presented. Read *et al.* reported similar findings in their classic pair potential simulations on the low temperature P42/ncm phase of LNO214[20]. Still, we are interested in the values of the surface energies. To calculate the surface energies associated with the two different charge-neutral terminations, we use hybrid DFT methods.

3.2.1 Calculation details

The CRYSTAL14 software package is employed to perform density functional theory calculations in this work.[71,91] The CRYSTAL14 software package is based on the expansion of the crystalline orbitals as a linear combination of a local basis set consisting of atom-centred Gaussian orbitals. The basis sets used for Ni and O atoms are triple-valence all-electron basis sets. A Ni atom is described by a 28-411d(41) contraction (one s, four sp, and two d shells). An O atom is described by an 8-411d(1) contraction (one s, three sp, and one d shells). The most diffuse sp(d) exponents are $\alpha_{Ni} = 0.6144(0.411)\text{bohrs}^{-2}$ and $\alpha_O = 0.1843(0.6)\text{bohrs}^{-2}$.[71] The La core

electrons are described with a pseudopotential, which is adapted from Dolg *et al.*'s quasirelativistic La pseudopotential[81]. The La valence electron basis functions are 411p(411)d(311)f(11) contracted sets (three s, three p, three d and two f shells) with the most diffuse exponent being $\alpha_{La} = 0.15\text{bohrs}^{-2}$ for each s, p, d and f shell as discussed in Section 2.3.4.[73] These basis sets ensure we have an accurate description of electron density at the La vacancy site.

The B3LYP hybrid-exchange electron density functional[70], implemented in the CRYSTAL14 package, is used to approximate electron exchange and correlation. This hybrid functional is expected to give a reliable description of strongly correlated solid oxide systems such as the LNO-RP family oxides.[73–75] Numerical integration of the exchange and correlation potentials and energy functional are performed on an atom-centred grid of points. The XXLGRID option implemented in CRYSTAL14 was used for all calculations, which consisted of a pruned grid consisting of 99 radial points and 5 subintervals with (146, 302, 590, 1454 and 590) angular points[71]. The cutoff threshold parameters of direct summation of the Coulomb and exchange series are set to 7, 7, 7, 7 and 14 as described in the CRYSTAL14 manual[71]. A Pack-Monkhorst mesh with a shrinking factor of 8 was chosen for reciprocal space sampling for La_2NiO_4. The structures selected as initial input for DFT simulation are taken from Skinner's[27] La_2NiO_4 neutron diffraction works. The supercells used in the calculations are the minimum conventional crystallographic cells of La_2NiO_4 (28 atoms) pre-relaxed with a g-type anti-ferromagnetic setup. The relaxation step and related discussions on the cell's magnetic ordering are detailed in the next Chapter. For the surface energy calculations, two different slabs are constructed by cleaving the relaxed supercells at the LaO and NiO2/LaOOLa terminations shown in Fig. 3.1. Twenty layers (or eight 7-atom stoichiometric units) are included in each slab. The slabs are periodic in the x-y plane. Along the z-direction ([001] direction), 200 Å vacuum spaces are place on the top and the bottom of the slab to ensure no interaction between slabs in this direction. The energies of the fully relaxed slabs are then used to calculate associated surface energies. As the slabs simulated are much thinner than most bulk materials, the surface energy convergence with respect to the thickness of slab is checked by computing the surface energies of the LaO terminated slabs with 5, 10, 15, 20 layers each.

3.2.2 Results and discussion

As mentioned in Section 2.5, the surface energy ΔE_s is defined as:

$$\Delta E_s = \frac{E_{surf} - E_{ideal}}{A} \tag{3.1}$$

where E_{surf} is the total energy of the lattice with surface exposed after relaxation, E_{ideal} is the total energy of the same lattice with no surfaces after relaxation and A is the total surface area. In this case, the E_{ideal} can be calculated from the total energy of the relaxed bulk unit cell and E_{surf} is the total energy of the fully relaxed slab. The surface area is simply the total area of the two (001) surfaces on each slab. Numerical differences between the total energy of the slab, E_{surf}, and the total energy of the bulk, E_{ideal}, may lead to instability of the surface energy with respect to the number of the layers in the slab. Therefore, the surface energies of LaO terminated La_2NiO_4 slabs are plotted with respect to their slab thickness to check the convergence of surface energies. The plotted graph is included in Fig. 3.2.

Fig. 3.2 shows that the surface energies of the LaO teminated slabs converge reasonably quick. Although the surface energy is not fully converged yet at 20 atomic layers, the trend has shown that it is very close to full convergence. Also, it becomes very computationally expensive to calculate the total energy of slabs thicker than 20 layers due to the large number of atoms involved. Therefore, no further calculations are carried out to obtain the complete convergence of the surface energies. This kind of relatively quick surface energy convergence is expected, as La_2NiO_4 has a quite wide bandgap (4 eV). The surface energy of such a wide-bandgap insulator is usually well defined. As a well-known 2D antiferromagnet, the energy change in the La_2NiO_4 slabs due to magnetic effects along the (001) directions is also found to be insignificant to the surface energy convergence. The results calculated from our DFT surface simulation based on 20 layers slabs are summarized in Table 3.1. A literature (001) Ni surface energy result from Read *et al.*'s work is also included. It is important to remember that this literature result is calculated from a low temperature LNO214 phase (P42/ncm) and the LNO214 crystal is distorted at this low temperature. Therefore the literature value is not suitable for a direct comparison to our results. Unfortunately, no other literature results for the room temperature

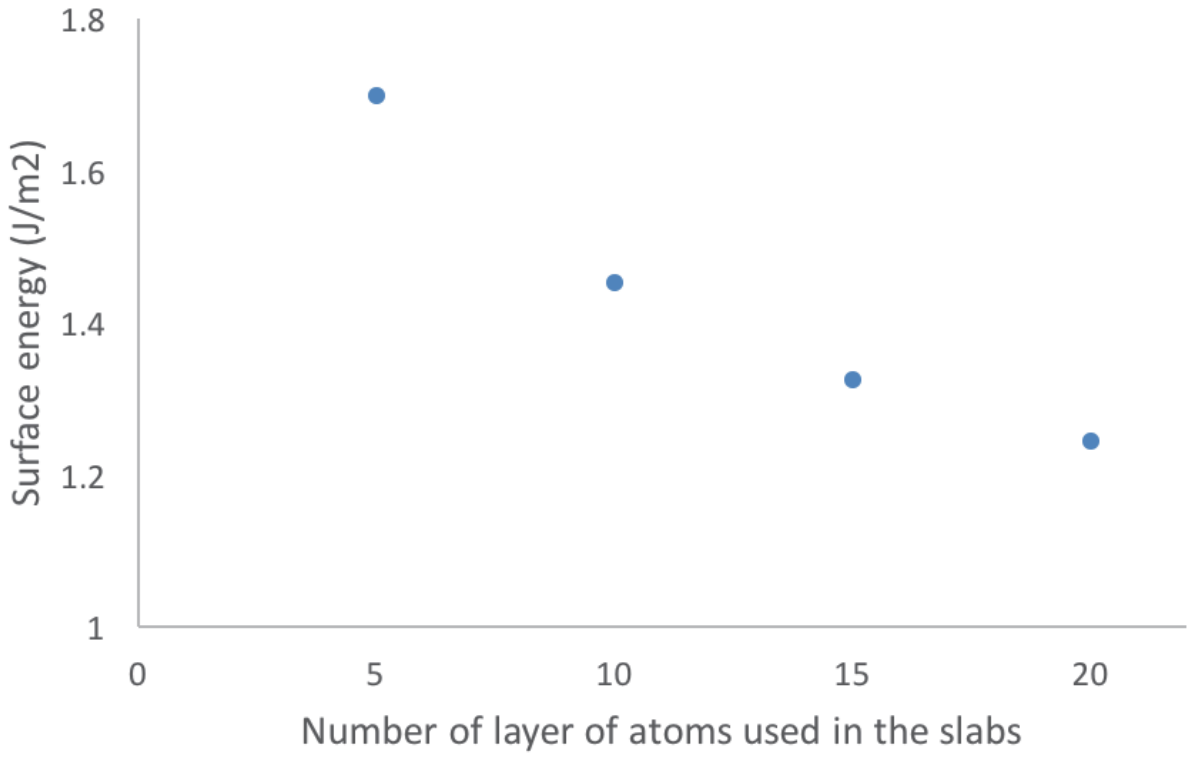


Figure 3.2: Surface energies of LaO terminated La_2NiO_4 slabs plotted with respect to the thickness of the slabs. The slabs with 5, 10, 15 and 20 atomic layers are calculated. The surface energies are computed with respect to

Table 3.1: Comparison of calculated and literature surface energies of two possible La_2NiO_4 surface terminations. NiO2/LaOOLa and LaO are the labels of the respective termination surfaces as discussed. The literature value for the Ni surface is from a simulation based on the low temperature LNO214 (001) surface. This value is not suitable for a direct comparison and is listed for indicative purpose only.

	NiO2/LaOOLa	LaO
Dipole (debyes)	7.327	0
Surface energy (J/m^2)	6.61	1.24
Literature value (J/m^2)	1.55[20]	N.A.

LNO214 (001) surface is available for comparison. Based on our results, the LaO termination, which presents a La-only surface, has a lower surface energy. The NiO2/LaOOLa surface has a much higher surface energy due to the dipole moments. It is also interesting that our LaO surface energy is lower than Read's Ni-containing surface energy. While a direct comparison between these energies cannot be justified, our lower LaO surface energy may still be indicative of some subtle electron redistribution and associated stabilization effect that cannot be revealed by the classical pair potential simulation done by Read. The LaO termination is suppose to be the stable room temperature LNO214 (001) termination and this will give a La-only (001) surface as observed in the experiments.

However, our simple surface energy calculations are not sufficient to explain all of the experimental findings, especially those results reporting an almost La-only surface on a multi-crystalline LNO214 sample[1]. The ideal room temperature LNO214 (010) and (100) terminations will always contain some Ni no matter where we cut. This certainly suggest that these surfaces are altered and are no longer ideal. Gauquelin's work on the long-term decomposition of the LNO214 offers some insights[90]. Gauquelin observed that higher order La-Ni-O Ruddlesden-Popper materials had formed on the surface of LNO214 after heating. Based on this, we suspect that the LNO214 material may decompose into its higher ordered cousins like LNO327 or LNO4310 with the presence of oxygen. The by-product of these decompositions, La_2O_3, may be present on the material and give a La surface no matter what the surface orientation is. To validate this hypothesis, the thermodynamic stability of LNO214 is evaluated with respect to other compounds in the La-Ni-O system.

Table 3.2: Thermodynamic parameters used to evaluate the change in Gibbs free energy for La_2NiO_4 decomposition. Note that for the phase transition of $La_3Ni_2O_7$ at 490K, we have $\Delta_{tr}H = 1800\text{Jmol}^{-1}, \Delta_{tr}S = 3.674\text{Jmol}^{-1}K^{-1}$.[92] The values here are applicable from 305K to 1673K

	a (J mol^{-1})	b (J mol^{-1}K^{-1})	c (J mol^{-1}K^{-1})	d_2 (J mol^{-1}K^{-2})	d_{-1} (J K mol^{-1})	Ref.
La_2NiO_4	-2095507.6	1035.849	-178.04	-0.007089	1214190	[92]
$La_3Ni_2O_7$	-3358980.1	1781.990	-301.86	-0.01712	1580000	[92]
$La_4Ni_3O_{10}$	-4599431.3	2368.174	-405.25	-0.0326	2130000	[92]
$LaNiO_3$	-1248967.7	696.185	-118.12	-0.0096	648000	[92]
La_2O_3	-1835600	674.72	-118	-0.008	620000	[93]

3.3 Thermodynamic stability of the LNO214 material

3.3.1 Gibbs energy of reaction for stoichiometric cases

The thermodynamic stability of LNO214 at any given temperature and oxygen partial pressure can be determined by considering the change in Gibbs free energy for its possible decomposition reactions. In this work, the following reactions are considered:

$$4La_2NiO_4 + \frac{1}{2}O_2 \rightarrow 2La_3Ni_2O_7 + La_2O_3 \tag{3.2}$$

$$3La_2NiO_4 + \frac{1}{2}O_2 \rightarrow La_4Ni_3O_{10} + La_2O_3 \tag{3.3}$$

$$2La_2NiO_4 + \frac{1}{2}O_2 \rightarrow 2LaNiO_3 + La_2O_3 \tag{3.4}$$

These reactions are selected as all of them are assumed to be under an oxygen-rich environment and react with oxygen to form another ternary compound. For ease of comparison, all reactions were normalised and balanced to consume half a mole of oxygen gas and produce one mole of La_2O_3.

As discussed in chapter 2, the change in Gibbs free energy for the above reactions at different temperatures and oxygen partial pressures can be written as:

$$\begin{aligned}\Delta G^{327}_{reaction}(T, p_{O_2}) = {} & 2\Delta G_{La_3Ni_2O_7}(T) + \Delta G_{La_2O_3}(T) \\ & - 4\Delta G_{La_2NiO_4}(T) - \frac{1}{2}\Delta\mu_{O_2}(T, p_{O_2})\end{aligned} \tag{3.5}$$

$$\begin{aligned}\Delta G^{4310}_{reaction}(T, p_{O_2}) = \Delta G_{La_4Ni_3O_{10}}(T) + \Delta G_{La_2O_3}(T) \\ - 3\Delta G_{La_2NiO_4}(T) - \frac{1}{2}\Delta\mu_{O_2}(T, p_{O_2})\end{aligned} \tag{3.6}$$

$$\begin{aligned}\Delta G^{113}_{reaction}(T, p_{O_2}) = 2\Delta G_{LaNiO_3}(T) + \Delta G_{La_2O_3}(T) \\ - 2\Delta G_{La_2NiO_4}(T) - \frac{1}{2}\Delta\mu_{O_2}(T, p_{O_2})\end{aligned} \tag{3.7}$$

where $\Delta G_{reaction}(T, p_{O_2})$ is the change in Gibbs free energy of the respective reactions depending on temperature, T, and oxygen partial pressure p_{O_2}, $\Delta G_{component}(T)$ is the Gibbs formation energy of the component at temperature T and $\Delta\mu_{O_2}(T, p_{O_2})$ is the relative chemical potential (with respect to the respective chemical potentials at the standard conditions) of oxygen molecules at temperature T and oxygen partial pressure p_{O_2}. The standard conditions are set to be 298.15 K and 1 bar pressure.

Using the Shomate equation presented in chapter 2, the standard molar Gibbs formation energy, $\Delta G^o(T)$, of a compound phase can be expressed as:

$$\Delta G^o(T) = G(T) - H^{SER} = a + bT + cT\ln(T) + \Sigma d_n T^n \tag{3.8}$$

where H^{SER} is the phases' Stable Element Reference of its constituent elements at 298.15 K and 1 bar. The coefficients a, b, c and d_n presented in Table 3.2 are taken from fits to experimental heat capacity measurements of the respective compounds using differential scanning calorimetry (DSC)[92,93].

The chemical potential of oxygen is given by[94,95]

$$\Delta\mu_{O_2}(T, p_{O_2}) = H^0_{O_2} - H^0_{O_2\text{-}RT} - TS^0_{O_2} + k_B T\ln\left(\frac{p_{O_2}}{p^0_{O_2}}\right) \tag{3.9}$$

where

$$H^0_{O_2} - H^0_{O_2\text{-}RT} = At + B\frac{t^2}{2} + C\frac{t^3}{3} + D\frac{t^4}{4} - \frac{E}{t} + F - H \tag{3.10}$$

and

$$S^0_{O_2} = A\ln(t) + Bt + C\frac{t^2}{2} + D\frac{t^3}{3} - \frac{E}{(2t^2)} + G \tag{3.11}$$

Table 3.3: Oxygen thermodynamic constants from NIST handbook for various temperature ranges.[95]

Temperature (K)	100-700	700-2000	2000-6000
A (kJ $mol^{-1}K^{-1}$)	31.32234	30.03235	20.91111
B (kJ $mol^{-1}K^{-2}$)	-20.23531	8.772972	10.72071
C (kJ $mol^{-1}K^{-3}$)	57.86644	-3.988133	-2.020498
D (kJ $mol^{-1}K^{-4}$)	-36.50624	0.788313	0.146449
E (kJ K mol^{-1})	-0.007374	-0.741599	9.245722
F (kJ mol^{-1})	-8.903471	-11.32468	5.337651
G (kJ mol^{-1})	246.7945	236.1663	237.6185
H (kJ mol^{-1})	0.0	0.0	0.0

The constants A, B, C, D, E, F, G, H are given in Table 3.3, and are taken from the NIST chemical data handbook.[95] The temperature coefficient t is $\frac{T}{1000}$, where T is temperature in kelvin. The unit of $H^0_{O_2} - H_{O_2\text{-}RT}$ is $kJmol^{-1}$, where RT stands for room temperature (298.15K), and the unit of $S^0_{O_2}$ is $Jmol^{-1}K^{-1}$. The equations 3.10 and 3.11 are effectively extended Shomate equations.

The Gibbs free energy of selected decomposition reactions can now be calculated at various temperatures and oxygen partial pressures, based on the thermodynamic equations and associated constants given above. Hence, the thermodynamic stability of LNO214 with respect to other La-Ni-O ternary compounds can be obtained. A negative Gibbs free energy of reaction means the LNO214 decomposition reaction is energetically favourable at given conditions.

3.3.2 DFT augmented Gibbs free energy for non-stoichiometric reactions

It is important to note that the lanthanum nickelates are not stoichiometric when operating as a cathode under SOFC working conditions, where oxygen partial pressure is equal or more than 0.2 bar. La_2NiO_4 is usually oxygen rich, while the higher order $La_3Ni_2O_7$ and $La_4Ni_3O_{10}$ are oxygen deficient. These non-stoichiometries allow oxygen transportation via interstitial or vacancy mechanisms. In this study, the thermodynamic equation constants of the compounds used are fitted as stoichiometric phases based on thermal measurements on real, non-stoichiometric phases[92,93,96]. To provide a better prediction under experimental conditions, the error due to

this difference must be estimated. For example, the Gibbs free energy of formation of the non-stoichiometric $La_2NiO_{4+\delta}$ is given as:

$$\Delta G_{\mathrm{La_2NiO_{4+\delta_{214}}}}(T, p_{\mathrm{O_2}}) = \mu_{\mathrm{La_2NiO_{4+\delta_{214}}}} - (2\mu_{La} + \mu_{Ni} + 2\mu_{\mathrm{O_2}} + \frac{\delta_{214}}{2}\mu_{\mathrm{O_2}}) \tag{3.12}$$

where $\Delta G_{\mathrm{La_2NiO_{4+\delta_{214}}}}$ is the Gibbs free energy of formation of $La_2NiO_{4+\delta_{214}}$ at temperature, T, and oxygen partial pressure, $p_{\mathrm{O_2}}$. The chemical potential of $La_2NiO_{4+\delta_{214}}$ at this temperature and pressure is $\mu_{\mathrm{La_2NiO_{4+\delta_{214}}}}$, while μ_{La}, μ_{Ni} and $\mu_{\mathrm{O_2}}$ are the chemical potentials of reference elemental La, Ni and oxygen gas at standard temperature and pressure.

To get the difference in the experimental value, we need the stoichiometric Gibbs free energy of formation to compare with. The formation free energy of stoichiometric La_2NiO_4 is given by:

$$\Delta G_{\mathrm{La_2NiO_4}}(T, p_{\mathrm{O_2}}) = \mu_{\mathrm{La_2NiO_4}} - (2\mu_{La} + \mu_{Ni} + 2\mu_{\mathrm{O_2}}) \tag{3.13}$$

where $\Delta G_{\mathrm{La_2NiO_4}}$ is the Gibbs free energy of formation of La_2NiO_4 at temperature, T, and oxygen partial pressure, $p_{\mathrm{O_2}}$. The chemical potential of La_2NiO_4 at this temperature and pressure is $\mu_{\mathrm{La_2NiO_4}}$. The definition of μ_{La}, μ_{Ni} and $\mu_{\mathrm{O_2}}$ are the same as above.

The difference between the experimental $\Delta G_{La_2NiO_{4+\delta}}$ and ideal $\Delta G_{\mathrm{La_2NiO_4}}$ is then:

$$\begin{aligned}
\Delta G^{diff}_{\mathrm{La_2NiO_4}} &= \Delta G_{\mathrm{La_2NiO_{4+\delta_{214}}}} - \Delta G_{\mathrm{La_2NiO_4}} \\
&= \mu_{\mathrm{La_2NiO_{4+\delta_{214}}}} - \mu_{\mathrm{La_2NiO_4}} - \frac{\delta_{214}}{2}\mu_{\mathrm{O_2}} \\
&= \mu^{diff}_{\mathrm{La_2NiO_4}} - \frac{\delta_{214}}{2}\mu_{\mathrm{O_2}}
\end{aligned} \tag{3.14}$$

which defines $\Delta G^{diff}_{\mathrm{La_2NiO_4}}$, and $\mu^{diff}_{\mathrm{La_2NiO_4}}$ is equal to $\mu_{\mathrm{La_2NiO_{4+\delta_{214}}}} - \mu_{\mathrm{La_2NiO_4}}$.

Similarly, for the higher order $La_3Ni_2O_7$ and $La_4Ni_3O_{10}$, there is:

$$\begin{aligned}
\Delta G^{diff}_{\mathrm{La_3Ni_2O_7}} &= \Delta G_{\mathrm{La_3Ni_2O_{7-\delta_{327}}}} - \Delta G_{\mathrm{La_3Ni_2O_7}} \\
&= \mu_{\mathrm{La_3Ni_2O_{7-\delta_{327}}}} - \mu_{\mathrm{La_3Ni_2O_7}} + \frac{\delta_{327}}{2}\mu_{\mathrm{O_2}} \\
&= \mu^{diff}_{\mathrm{La_3Ni_2O_7}} + \frac{\delta_{327}}{2}\mu_{\mathrm{O_2}}
\end{aligned} \tag{3.15}$$

$$\begin{aligned}\Delta G^{diff}_{La_4Ni_3O_{10}} &= \Delta G_{La_4Ni_3O_{10-\delta_{4310}}} - \Delta G_{La_4Ni_3O_{10}} \\ &= \mu_{La_4Ni_3O_{10-\delta_{4310}}} - \mu_{La_4Ni_3O_{10}} + \frac{\delta_{4310}}{2}\mu_{O_2} \\ &= \mu^{diff}_{La_4Ni_3O_{10}} + \frac{\delta_{4310}}{2}\mu_{O_2}\end{aligned} \tag{3.16}$$

where $\mu^{diff}_{La_3Ni_2O_7}$ and $\mu^{diff}_{La_4Ni_3O_{10}}$ are defined in the same way as $\mu^{diff}_{La_2NiO_4}$.

The differences in the chemical potential of respective LNO RP compounds can be estimated using their DFT calculated ground state energies, assuming a small free energy change due to entropy. The chemical potential of oxygen gas can be calculated using data from the NIST chemical database.[95] The defect structures selected for DFT calculation are $La_2NiO_{4.25}$, $La_3Ni_2O_{6.75}$ and $La_4Ni_3O_{9.5}$. These non-stoichiometries are selected to represent extreme cases observed in experiments.[82,97] The energy differences between these defective structures and their respective ideal structures are used to plot the Gibbs free energies of reaction when defective species are involved.

Taking the reaction between $La_2NiO_{4.25}$ and $La_3Ni_2O_7$ as an example, for the overall reaction, we have:

$$4La_2NiO_{4.25} \rightarrow 2La_3Ni_2O_7 + La_2O_3 \tag{3.17}$$

Its Gibbs free energy of reaction will be:

$$\begin{aligned}\Delta G^{327}_{def.r.}(T, p_{O_2}) &= 2\Delta G_{La_3Ni_2O_7}(T) + \Delta G_{La_2O_3}(T) - 4\Delta G_{La_2NiO_{4.25}}(T) \\ &= 2\Delta G_{La_3Ni_2O_7}(T) + \Delta G_{La_2O_3}(T) \\ &\quad - 4(\Delta G_{La_2NiO_4}(T) + \mu^{diff}_{La_2NiO_4} - \frac{1}{8}\mu_{O_2})\end{aligned} \tag{3.18}$$

The other three defect reactions considered are:

$$4La_2NiO_4 + \frac{1}{4}O_2 \rightarrow 2La_3Ni_2O_{6.75} + La_2O_3 \tag{3.19}$$

$$3La_2NiO_{4.25} + \frac{1}{8}O_2 \rightarrow La_4Ni_3O_{10} + La_2O_3 \tag{3.20}$$

$$3La_2NiO_4 + \frac{1}{4}O_2 \rightarrow La_4Ni_3O_{9.5} + La_2O_3 \tag{3.21}$$

Free energy changes for these reactions are then plotted together with their respective ideal reactions.

The CRYSTAL14 software package is also employed to perform density functional theory calculations for this part.[71,91] Most of the computational details are the same as detailed in Section 3.2.1 except a few things. A "ghost" atom is used to describe an atomic vacancy by removing the nucleus and all associated electronic basis sets except the two most diffuse contractions of each original s, p, d and f shells. For the larger $La_3Ni_2O_7$ and $La_4Ni_3O_{10}$ cells, a shrinking factor of 4 is used. The structures selected as initial input for DFT simulation are taken from Ling's[82] neutron diffraction works for $La_3Ni_2O_7$ and $La_4Ni_3O_{10}$. The supercells used in the calculations are the respective minimum conventional crystallographic cells of La_2NiO_4 (28 atoms), $La_3Ni_2O_7$ (24 atoms) and $La_4Ni_3O_{10}$ (34 atoms). For the defective cases, $La_2NiO_{4.25}$ calculation uses a cell containing 29 atoms (1 oxygen interstitial), $La_3Ni_2O_{6.75}$ calculation uses a cell containing 47 atoms (1 oxygen vacancy) and $La_4Ni_3O_{9.5}$ calculation uses a cell containing 33 atoms (1 oxygen vacancy). Fig. 3.3 illustrates the position of the interstitial oxygen used in $La_2NiO_{4.25}$. Initial interstitial oxygen position is chosen based on experimental results. In Fig. 3.3, the lattice structure shown is already relaxed using DFT calculation. Charge neutrality is maintained by promoting or demoting appropriate numbers of Ni atoms.

3.3.3 Thermodynamic stability for perfect LNO214

The Gibbs free energy of the reactions given in equations 3.5 to 3.7 are calculated to evaluate the thermodynamic stability of La_2NiO_4 for temperatures over the range of 305 K to 1673 K, and oxygen partial pressure ranging from 1×10^{-25} bar to 1 bar. Plots of the results are given in Fig. 3.5 to Fig. 3.7.

As shown in Fig. 3.5, the decomposition of La_2NiO_4 into higher order RP La-Ni-O materials is thermodynamically favourable up to about 1400 K at 0.2 bar oxygen partial pressure (atmospheric pressure of oxygen). $La_3Ni_2O_7$ is the energetically favourable phase below 1000 K, while $La_4Ni_3O_{10}$ will be more favourable above 1000 K. $LaNiO_3$ is never the preferred phase over the entire temperature range considered. According to the results, once in touch with ambient

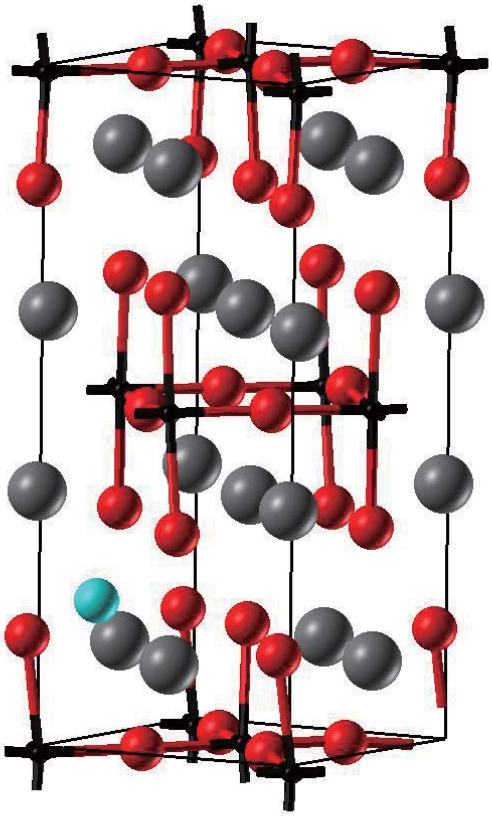


Figure 3.3: A schematic showing the interstitial oxygen position added in the La_2NiO_4 structure. The highlighted light blue sphere represents the intersitial oxygen. Lattice oxygen atoms are coloured in red. La atoms are coloured in grey. Ni atoms are coloured in black. The crystal structure shown here is a calculated relaxed structure. Distortions caused by the interstial oxygen can be seen clearly in this figure. A Ni atom at the corner is not drawn on this sketch due significant distortion from its ideal lattice position. This Ni atom is still properly treated in the calculations.

air, the LNO214 material can start to decompose and form the higher ordered $La_3Ni_2O_7$ even at room temperature. At the designated IT-SOFC operation temperature (500-800°C), this decomposition will also proceed.

These results show that LNO would start to decompose when it is in contact with air even at room temperature. The decompositions will also take place at the designated IT-SOFC operation temperature (600-800°C). We suspect that the decomposition products La_2O_3 and $La_3Ni_2O_7$ will form a layered structure on top of the bulk La_2NiO_4. Taking the (001) surface as an example, there are two possible stacking orders, $La_3Ni_2O_7$-La_2O_3-La_2NiO_4 and La_2O_3-$La_3Ni_2O_7$-La_2NiO_4, with both being ordered from the surface to the bulk. The latter one is predicted to be the favourable stacking order, as shown in Fig. 3.4. The first stacking order contains a large lattice mismatch between La_2O_3 and the two La-Ni-O RP phases, while the second one only contains one such large mismatch and one very small interfacial strain between the two La-Ni-O RP phases. The lattice mismatch between $La_3Ni_2O_7$ and La_2NiO_4 is only about 1% at the (001) interface[27,82,98]. This predicted stacking order is consistent with Druce *et al.*'s secondary ion mass spectrometry (SIMS) - low energy ion scattering (LEIS) depth profiling of polycrystalline La_2NiO_4. Druce's depth profile also showed a La enriched - Ni enriched - stoichiometric layered structure from the surface to the bulk of the crystal.[3] The peak Ni:La ratio they observed in the Ni enriched region is about 2:3, which agrees to the Ni:La ratio in our predicted sub-surface $La_3Ni_2O_7$ layer.

These results also agree partly with the long-term decomposition experiment on $La_2NiO_{4+\delta}$. In this experiment Gauquelin *et al.* heated $La_2NiO_{4+\delta}$ to 1273 K in flowing air for two weeks[90]. Characterisation of the heated surface with transmission electron microscopy (TEM) revealed layers of $La_3Ni_2O_7$ and $La_4Ni_3O_{10}$ with thicknesses of about 700 nm. On the (100) surface, both $La_3Ni_2O_7$ and $La_4Ni_3O_{10}$ were found, but only $La_4Ni_3O_{10}$ was present on the (001) surface. According to our calculations, $La_4Ni_3O_{10}$ should be the most stable phase at 1273K. The mixed layer of $La_4Ni_3O_{10}$ and $La_3Ni_2O_7$ may be due to incomplete conversion of $La_3Ni_2O_7$ formed at a lower temperature during the heating process and previous thermal history.

To form the transformed layers, La needs to move from the bulk to the surface. As there are

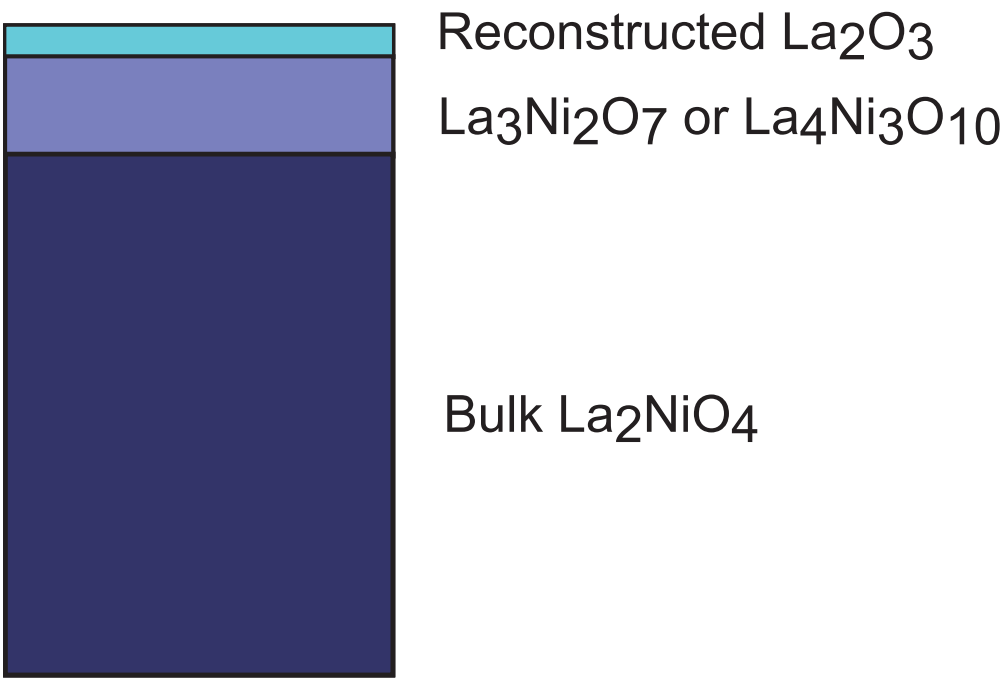


Figure 3.4: A representation of the proposed layered structure, with reconstructed La_2O_3 exposed as the surface layer, $La_3Ni_2O_7$ or $La_4Ni_3O_{10}$ being the intermediate layer between the surface and the bulk La_2NiO_4

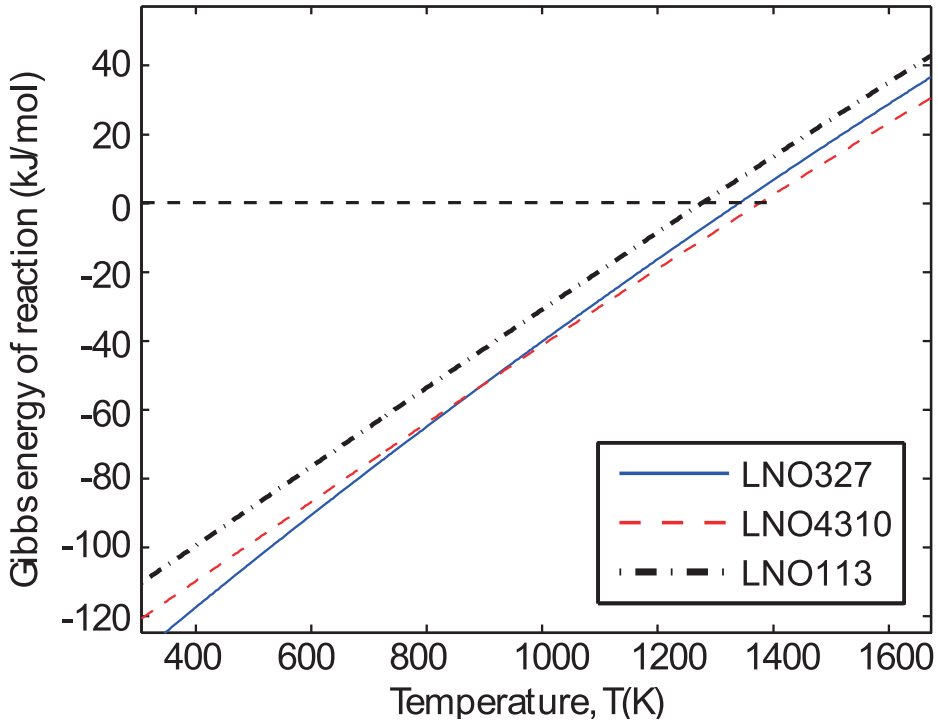


Figure 3.5: Gibbs energy change for the reaction La_2NiO_4 decomposing into $LaNiO_3$, $La_3Ni_2O_7$ or $La_4Ni_3O_{10}$ and La_2O_3 at 0.2 bar oxygen partial pressure over the temperature range of 305-1673 K. In the legend, the label LNO327 is for decomposition into $La_3Ni_2O_7$, LNO4310 is for $La_4Ni_3O_{10}$, and LNO113 is for $LaNiO_3$.

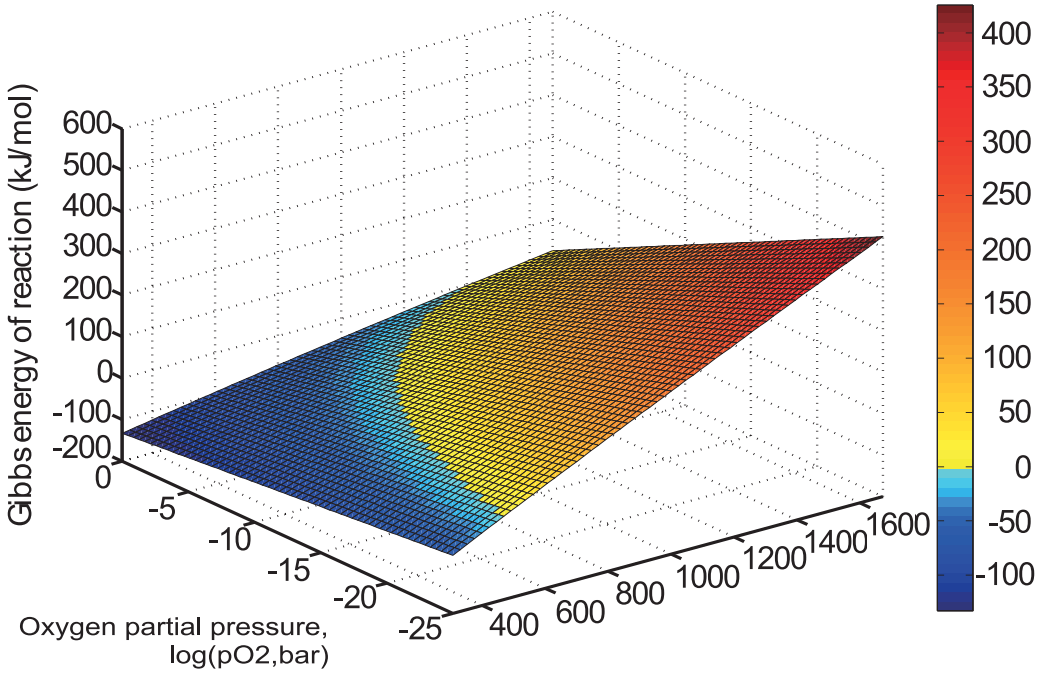


Figure 3.6: Gibbs reaction energy for La_2NiO_4 into $La_3Ni_2O_7$ and La_2O_3 over the range of 1 bar to 1×10^{-25} bar oxygen partial pressure, and 305K to 1673K. The colour bar reflects the Gibbs energy of reaction in kJ/mol. The Gibbs energy of reaction is equal to zero at the edge between the blue and yellow regions.

different diffusion paths for La to the (001) and (100) surfaces we expect different La diffusion rates, and hence different growth rates for the transformed layers at these surfaces. One significant difference between our prediction and Gauquelin's experiment is that the other predicted product, La_2O_3, was not observed in the experiment[90]. A surface layer only containing La_2NiO_4 and its higher order RP counterparts cannot give the La rich region observed with XPS[1] and SIMS-LEIS depth profiling[3] but rather the opposite (La deficient region[90]). Burriel *et al.* reported that the La and Sr rich surface layer is about 7 nm thick in the related $La_{2-x}Sr_xNiO_{4+\delta}$ phase. In Druce's more recent work[3], the La enriched layer is only about 1 nm thick in the depth profile of polycrystalline ceramic La_2NiO_4. Such a thin layer may be damaged by the destructive Focused Ion Beam (FIB) technique, which was used to cut a suitable lamellar cross-section at the surface for TEM study in Gauquelin's experiment.

Despite the thermodynamically favoured decomposition process (about -100kJ/mol for La_2O_3 production at room temperature), La_2NiO_4 is stable and does not transform into its higher

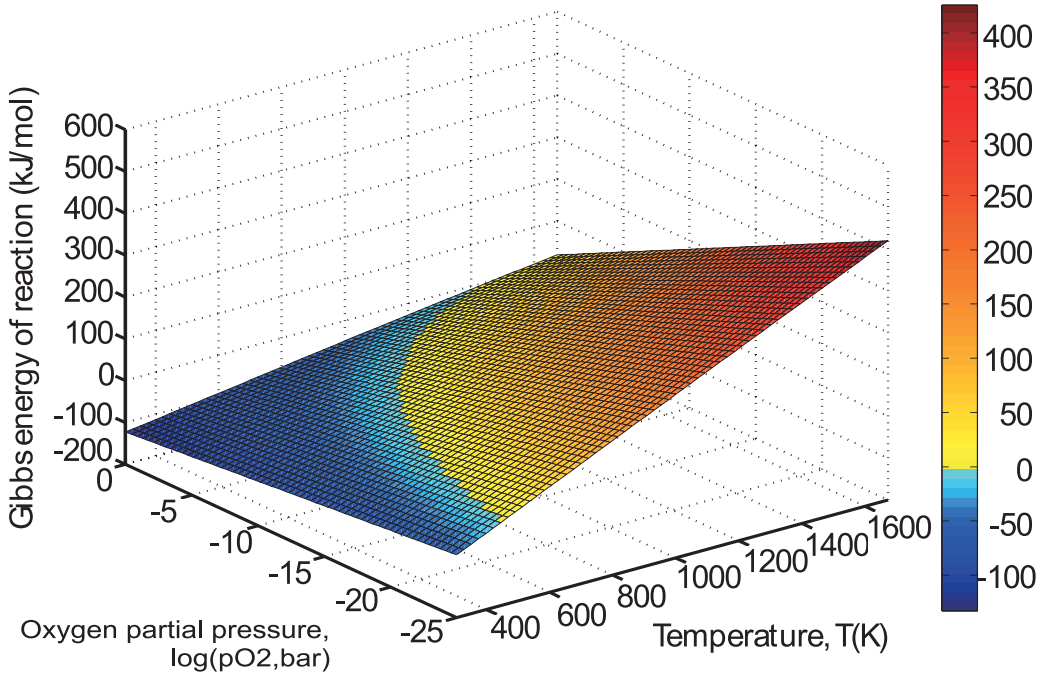


Figure 3.7: Gibbs reaction energy for La_2NiO_4 into $La_4Ni_3O_{10}$ and La_2O_3 over the range of 1 bar to 1×10^{-25} bar oxygen partial pressure, and 305K to 1673K. The colour bar reflects the Gibbs energy of reaction in kJ/mol. The Gibbs energy of reaction is equal to zero at the edge between the blue and yellow regions.

order R-P phases completely at room temperature. In the long-term decomposition experiment, only about 700 nm of the surface La_2NiO_4 was converted into $La_3Ni_2O_7$ or $La_4Ni_3O_{10}$ after two weeks[90]. Therefore, there must be a very slow rate determining step or a surface passivation mechanism to prevent complete decomposition of La_2NiO_4. The three experimental works mentioned earlier treated their samples differently (1273 K for two weeks (Gauquelin), 723 K for 72 hours (Burriel) and 1273K for 12 hours (Druce)). A shorter heating time at a lower temperature gives a thinner transformed layer (only a few nanometers) than the high temperature, long-term heated sample (about 700 nm).[1,3,90] Heating temperature and duration do have significant impact on the amount of La_2NiO_4 transformed. The reactions that result in the formation of the surface oxide layer must therefore include at least one activated process. A strong candidate is the diffusion of La, a process that is necessary for the oxide formation, and which will be activated. The diffusion barriers of several possible La diffusion paths are briefly evaluated in the next section. The large difference in the thickness of A-site enriched layers reported by Burriel and Druce, despite having a similar thermal treatments, is believed to be mainly due to Sr segregation which only occurs in Burriel's Sr-doped $La_{2-x}Sr_xNiO_{4+\delta}$. This would lead to a much thicker (7 nm compared to Druce's 1 nm) A-site (La+Sr) enriched region despite similar thermal history. In addition, Burriel's sample is a single crystal while Druce tested a polycrystalline ceramic sample. The different natures of the samples should also affect the amount of decomposed La_2NiO_4.

Fig. 3.6 and Fig. 3.7 clearly show that oxygen partial pressure has a significant impact on the Gibbs free energy of these reactions. According to the graphs, the critical oxygen partial pressure required to allow decomposition varies with temperature. Therefore, the thickness of maximum decomposition layers formed at different temperatures after long heating times will vary with critical oxygen partial pressure. In a controlled low p_{O_2} or high vacuum environment, this maximum transformation thickness can be measured to verify the hypothesis. If this proves to be true, controlling the oxygen partial pressure and the temperature might provide a way to suppress or reverse the decomposition when desired.

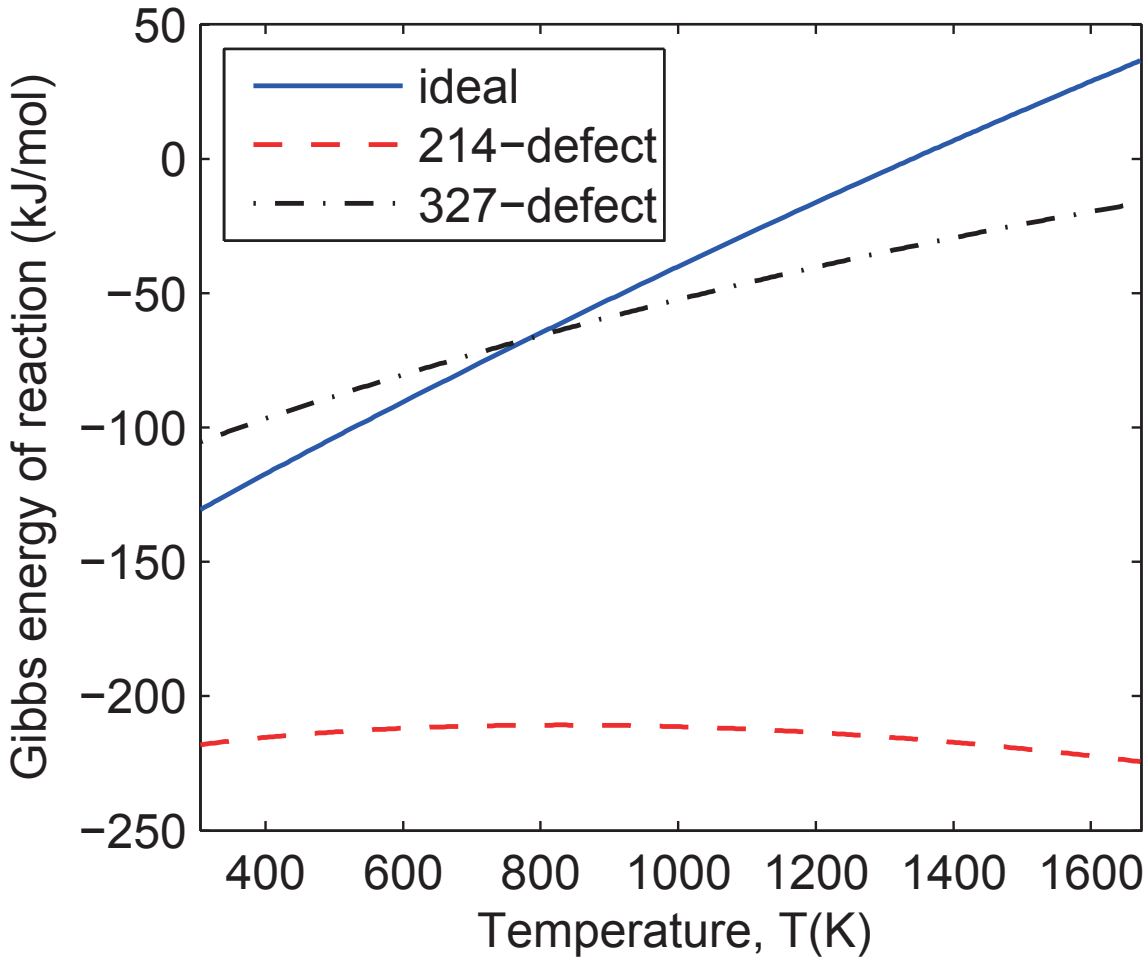


Figure 3.8: Comparison of Gibbs reaction energy for La_2NiO_4 decomposition into $La_3Ni_2O_7$ (labelled as ideal), $La_2NiO_{4.25}$ decomposition into $La_3Ni_2O_7$ (214-defect) and La_2NiO_4 decomposition into $La_3Ni_2O_{6.75}$ (327-defect) at 0.2 bar oxygen partial pressure over the range of 305-1673 K.

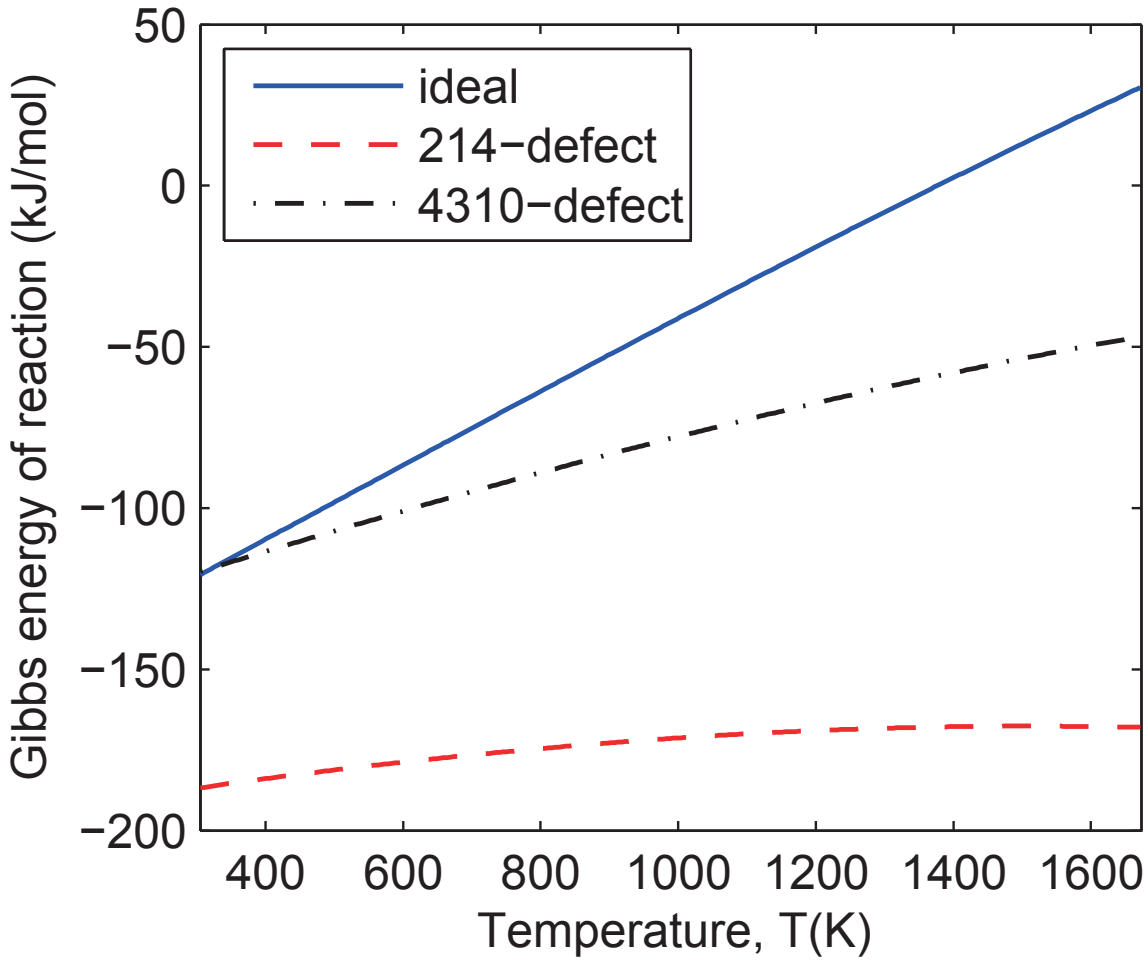


Figure 3.9: Comparison of Gibbs reaction energy for La_2NiO_4 decomposition into $La_4Ni_3O_{10}$ (labelled as ideal), $La_2NiO_{4.25}$ decomposition into $La_4Ni_3O_{10}$ (214-defect) and La_2NiO_4 decomposition into $La_4Ni_3O_{9.5}$ (4310-defect) at 0.2 bar oxygen partial pressure over the range of 305-1673 K.

Table 3.4: Comparison of calculated and experimental lattice parameters of relevant La-Ni-O species. Expt. is experimental structure, and Calc. is calculated structure. All literature experimental structures are measured at 298K.

Compound		a (Å)	b (Å)	c (Å)	Ref.
La_2NiO_4	Expt.	5.459	5.464	12.685	[27]
	Calc.	5.538(8)	5.539(3)	12.752(2)	
	Error	1.47%	1.39%	0.52%	
$La_3Ni_2O_7$	Expt.	5.397	5.450	20.507	[82]
	Calc.	5.435(0)	5.586(1)	20.868(3)	
	Error	0.70%	2.49%	1.76%	
$La_4Ni_3O_{10}$	Expt.	5.413	5.462	27.960	[82]
	Calc.	5.448(3)	5.570(8)	28.512(2)	
	Error	0.65%	1.99%	1.97%	

3.3.4 Defective La-Ni-O compounds

To obtain a more complete picture of the decomposition thermodynamics, we use density functional theory simulations to estimate the effect of oxygen defects on the reactions as described in the method section. Ideal experimental structures of the La-Ni-O compounds are fully relaxed and optimised first with g_x type antiferromagnetic ordering. A more detailed discussion of the perfect La-Ni-O compounds' energetics based on DFT simulation is included in the next chapter.

The lattice parameters of optimised La-Ni-O RP structures are summarised in table 3.4. The differences between the experimental structures and the calculated structures are small (less than 3%) in all three cases. Therefore, the choice of the basis sets and functionals indeed describe these Ruddlesden-Popper compounds quite well. Respective compounds with defects are constructed by adding oxygen interstitials or vacancies to the relaxed ideal structures. The position of interstitials or vacancies are chosen according to experimentally determined literature values.[27,82] After the introduction of the defects, these altered lattices are then relaxed and optimised again. The energies of the perfect and defective lattices are recorded for the evaluation of the Gibbs reaction energies' change due to the defects. The resulting Gibbs energies of reaction for the different defect cases are plotted in Fig. 3.8 and Fig. 3.9.

In Fig. 3.8 and 3.9 we can see that all the defective reactions still have negative reaction Gibbs energy in the IT-SOFC working temperature range (873 -1073 K). The defective reactions seem

to be always favourable even at temperatures beyond 1673 K according to the trend shown in Figs. 3.8 and 3.9. However, the assumption of small energy change due to entropy will not hold at temperatures much higher, so the estimated trends based on ground-state DFT calculations should only be used to predict reactions at lower temperature ranges. On the other hand, for applications like IT-SOFC, the assumption is safe for the most relevant temperature range (873 - 1073K). Over the temperatures in which we are interested, the four reactions considered can at least give an idea of the order of magnitude of the decomposition Gibbs energies under experimental condition since the involved phases are some of the extreme defective cases. It is noted that the 214-defect reactions are particularly favourable as shown in the figures (about 100 kJmol^{-1} more favourable than ideal reactions). This suggests that a significant amount of energy is required to accommodate the oxygen interstitials in $La_2NiO_{4.25}$ at the ground state (DFT simulation condition). At ground state (0K), it is more difficult for the ideal lattice to take in an interstitial oxygen (like defective LNO214) than to lose an oxygen and form a vacancy (like defective LNO327 and LNO4310) due to contraction of the lattice at low temperature. Therefore, it appears to be very favourable for the $La_2NiO_{4.25}$ to decompose and lose the extra oxygen. In reality, the $La_2NiO_{4.25}$ may not so readily decompose at room temperature or above. This is one of the sources of errors when using DFT simulation to estimate the Gibbs energies of reaction for the defective reactions. The actual Gibbs free energy of reaction will be affected by specific experimental conditions, including temperature, oxygen partial pressure, thermal histories and the initial composition of the materials, but they will fall somewhere close to the calculated region, and the Gibbs energy of decomposition is likely to be still negative at lower temperatures. Therefore, the simple conclusion drawn from these estimations is that the decomposition will be favoured at IT-SOFC operation temperatures even for the extremely defective compositions.

3.4 Conclusion

In this particular study, we attempt to provide theoretical explanations to the mysterious La-terminated surfaces observed on the La_2NiO_4 material in many experiments. The surfaces are

studied using both DFT and thermodynamic methods. Several possible room temperature La_2NiO_4 (001) terminations are suggested and evaluated using Tasker's surface classification method. Two of the charge-neutral surface slabs are simulated with hybrid DFT method. Our DFT surface simulation suggest that the LaO termination is the most stable one for the La_2NiO_4 (001) surface, as this termination has the lowest surface energy and zero dipole moment. This is the only surface simulation result on the room temperature La_2NiO_4 (001) surface.

On the other hand, the thermodynamic stabilities of La_2NiO_4 and a chosen defective variant $La_2NiO_{4.25}$ with respect to their competing La-Ni-O compounds, $La_3Ni_2O_7$, $La_4Ni_3O_{10}$ and $LaNiO_3$ are evaluated over a temperature range of 305K - 1673K. The Gibbs formation energies of the perfect respective compounds involved are calculated using the Shomate equation based on experimentally fitted thermodynamic constants. The calculated Gibbs formation energies are put into selected equations of La_2NiO_4 decomposition reaction to plot related Gibbs energy of reaction with change in temperature and oxygen partial pressure. The plotted graphs suggest that the decomposition of ideal La_2NiO_4 is thermodynamically favourable up to 1400K. The decomposition products varies with temperature. At temperature less than 1000K, $La_3Ni_2O_7$ will be formed, while at higher temperature, $La_4Ni_3O_{10}$ will be formed. At all temperatures, La_2O_3 is always formed as a by-product. The change of favoured compounds with temperature also hints that the $La_3Ni_2O_7$ formed at lower temperature may transform into $La_4Ni_3O_{10}$ if subjected to significantly extended heating over 1000 K later.

To provide a better description of La_2NiO_4 stability under experimental condition, the defective cases of possible decomposition reactions are investigated with the support of DFT calculations. The energy difference between the perfect compounds and a few representative defective compounds are calculated using hybrid DFT simulations. The error due to entropy is assumed small, as the compounds calculated are all solids and the defect concentration is not high. The DFT augmented Gibbs energies of reaction are plotted over the same range of temperature as the perfect cases. Among the defective reactions considered, all of them are still favourable for La_2NiO_4 decomposition. Therefore, we can conclude that the decomposition La_2NiO_4, no matter perfect or not, is favourable for the temperatures relevant to IT-SOFC application.

The limited decomposition of La_2NiO_4 observed in experiments is also discussed. A layered surface model based on the minimisation of interfacial strain is proposed, where La_2O_3 cannot be formed within the bulk La_2NiO_4 due to large strain and distortion of structure. This model can provide an explanation to the purely La terminated surface observed, especially for the La-Ni mixed (100) surfaces. In this model, the decomposition of bulk La_2NiO_4 is suggested to be hindered by the slow diffusion of La ions through the perovskite layers of the material, as all the La_2O_3 formed must precipitate at the surface. Combining our simulation results, we suggest that a freshly made La_2NiO_4 sample should terminate with the LaO layer along the [001] direction, while fresh (100) and (010) surfaces terminate with a mixture of La and Ni atom. When these surfaces are exposed to oxygen, they will transform into $La_3Ni_2O_7$ or $La_4Ni_3O_{10}$ with a layer of La_2O_3 depending on the temperature. The La_2O_3 formed will always give a La surface no matter what the surface's orientation is. According to this proposed model, La diffusion will play a significant role in the formation of the transformed surface. Some kinetic evaluation of the La diffusion is included in the next chapter.

In addition, the calculated energies of the perfect and defective La-Ni-O compounds can be used to calculate respective oxygen defect formation energy using equation 2.46 mentioned in chapter 2. Details of the oxygen defect formation energy, together with the calculation of La defect energy, will be discussed in the next chapter.

Chapter 4

LNO214 defects and diffusion kinetics

Part of this work has been published and reprinted with permission from Ji Wu, Stevin S Pramana, Stephen J Skinner, John A Kilner, and Andrew P Horsfield. Why Ni Is Absent from the Surface of La 2 NiO 4+δ. J. Mater. Chem. A (2015): 2376023767. doi:10.1039/C5TA03759J. Copyright 2015 Royal Society of Chemistry.

4.1 Introduction

In the previous chapter, classic thermodynamic calculations and Ab Initio simulation methods are combined to provide an explanation for the origin of the La-enriched surface observed on the La_2NiO_4 material. Based on our calculations, we suggest that a decomposition of the $La_2NiO_{4+\delta}$ material is thermodynamically favourable and may be the cause of the La-terminated surfaces observed in the experiments. A natural question that follows is "why the favourable decomposition does not proceed all the way to consume the entire bulk of $La_2NiO_{4+\delta}$"? Indeed, the $La_2NiO_{4+\delta}$ materials remain largely intact at room temperature in reality despite that its decomposition is thermodynamically favourable at this temperature. There must be some mechanism hindering the complete decomposition of the $La_2NiO_{4+\delta}$ materials. One of the possible explanations is that the rate determining step of the decomposition reaction is very slow. Therefore, it is of interest to figure out what the rate-determining step might be and how

difficult the rate-determining step is. Understanding this problem can provides hints on how to control or engineer the $La_2NiO_{4+\delta}$ decomposition reaction and achieve the desired conditions in real SOFC applications.

By comparing the crystal structures of the La_2NiO_4 and $La_3Ni_2O_7/La_4Ni_3O_{10}$ materials, it can be easily seen that the main difference between them is the number of $LaNiO_3$ perovskite layers in-between the rock-salt like LaO layers. The transformation of the La_2NiO_4 into its higher order cousins would certainly involve the transportation and relocation of the atoms in the LaO layer. The La and O atoms from this layer can diffuse to the material's surface and form La_2O_3. Since it is known that the O ions in the La_2NiO_4 material's LaO layer are mobile[15,19,27], the diffusion of the La ions looks more likely to be the slow rate-determining step. Therefore, the value of the calculated La ionic diffusion barrier can be used as an indicator of the La_2NiO_4 decomposition's reaction rate. The diffusion of the La ion is also likely to create a La vacancy at its original site. The calculated vacancy formation energy of La may also give us an idea of how easily this kind of diffusion may happen. In this study, the hybrid density functional method is used to calculate the La ionic diffusion barrier and the La vacancy formation energy. To facilitate the delicate transition state calculation, it is important to evaluate and choose proper simulation setups before conducting the product run.

4.2 Evaluation of simulation setup

As discussed in chapter 1, the La_2NiO_4 material has three slightly different phases depending on the temperature. In addition, the presence of spin-polarised Ni ions brings in the problem of magnetic ordering. As we are interested in the properties of La_2NiO_4 at room temperature and up to about 873 K, the choice of input structure and magnetic ordering may affect our simulation results. In some cases, inappropriate simulation inputs may be the main source of error when comparing simulation results and experimental values. To evaluate the effects of various simulation setups for the La_2NiO_4 calculation, a number of La_2NiO_4 simulations are carried out using different input structures and magnetic orderings.

Table 4.1: Summary of La_2NiO_4 experimental lattice parameters used in this work. These phases are measured at temperature T as listed. LTT, RTO and HTT stands for low temperature tetragonal phase, room temperature orthorhombic phase and high temperature tetragonal phase respectively.

La_2NiO_4 Phase	Space Group	a (Å)	b (Å)	c (Å)	T (K)	Ref.
LTT	P42/ncm	5.502	5.502	12.504	10	21
RTO	Fmmm	5.459	5.464	12.685	298	27
HTT	I4/mmm	3.884	3.884	12.753	723	27

As shown in section 1.3.2, there have been a large number of studies on the structures of La_2NiO_4 at various temperatures. Due to technical limitations, some of the earlier characterisation works were not able to fully eliminate the oxygen interstitials in the $La_2NiO_{4+\delta}$ and reported the non-stoichiometric structure as the stoichiometric La_2NiO_4. Currently, the consensus is that the stoichiometric La_2NiO_4 has three phases depending on the temperature; the low temperature tetragonal phase (LTT, up to 80 K), the room temperature orthorhombic phase (RTO, 80 K to about 400 K) and the high temperature tetragonal phase (HTT, above 400 K)[17,27]. The latter two phases (RTO and HTT) are more relevant to La_2NiO_4's application in SOFC. Nonetheless, we decided to carry out a thorough comparison of the three different phases. For consistency, the input experimental structures of the RTO and HTT phases are taken from Skinner's neutron diffraction work[27]. The LTT input lattice constants are taken from Lander's work[21]. The input experimental lattice constants are summarised in table 4.1.

In addition to the different phases, the input magnetic ordering is also a factor that may affect simulation results. As mentioned in chapter 1, the magnetic ordering in La_2NiO_4 has been studied extensively. The La_2NiO_4 material possesses a g_x type antiferromagnetic ordering where each of the Ni ions has an opposite spin to its neighbouring Ni ion (as shown in Fig. 1.5). The stoichiometric La_2NiO_4 material's Néel temperature has been measured to be around 330K[17]. Although the bulk La_2NiO_4 material will be paramagnetic above the Néel temperature, the antiferromagnetic ordering may still be relevant in small simulation supercells at these high temperatures. The DFT simulation supercell usually only contains tens to hundreds of atoms. In such a small crystal cell, the short-range ordering may still follow the antiferromagnetic ordering. To see how the magnetic ordering affect the simulation results of the La_2NiO_4 material, we have carried out a set of simulations with combinations of different input phases and

magnetic orderings. The software (CRYSTAL14) and settings used are the same as discussed in the previous chapter and section 3.2.1. The calculated results are summarized in table 4.2. From table 4.2, we can see that the choice of magnetic ordering clearly affects the quality of the

Table 4.2: Summary of different optimised La_2NiO_4 phases with ferromagnetic (FM) and antiferromagnetic (AFM) ordering. For the high temperature phase, a calculation using no magnetic ordering is also included (labelled as NM). The energy difference per unit cell (ΔE) between the AFM and the FM calculations are also included. The percentage differences between each calculated and experimental lattice constants are listed below the relevant calculated data. The AFM calculations are used as the reference state in each case. Mag. Config. stands for magnetic configuration. In the case of experimental values, the magnetic configuration is listed as Exp.

Space Group	Mag. Config.	**a** (Å)	**b** (Å)	**c** (Å)	V (Å^3)	ΔE (eV/unit)
P42/ncm	Exp.	5.502	5.502	12.504	378.52	-
	FM	5.629	5.629	12.704	402.57	+0.1366
		2.31%	2.31%	1.60%	6.35%	
	g_x AFM	5.607	5.607	12.732	400.25	0
		1.91%	1.91%	1.82%	5.75%	
Fmmm	Exp.	5.459	5.464	12.685	378.33	-
	FM	5.562(33)	5.562(37)	12.822	396.66	+0.1436
		1.89%	1.79%	1.08%	4.85%	
	g_x AFM	5.538(8)	5.539(3)	12.752	391.17	0
		1.47%	1.39%	0.52%	3.39%	
I4/mmm	Exp.	3.884	3.884	12.753	192.41	-
	FM	3.933	3.933	12.822	198.37	+0.1434
		1.26%	1.26%	0.54%	3.10%	
	g_x AFM	3.924	3.924	12.832	197.62	0
		1.02%	1.02%	0.62%	2.69%	
	NM	3.756	3.756	13.769	194.28	+0.8503
		-3.30%	-3.30%	7.97%	0.79%	

simulation results. Those structures optimised with the AFM magnetic structures agree with experimental values systematically better than the simulations using FM or non-magnetic (NM) magnetic structures. The lattice energies of the simulated AFM structures are the smallest for all the three different phases, which agree with literature experimental and computational results[17,21,28–33]. The FM lattice energies are larger than the AFM lattice energies by about 0.1 eV per unit cell in all the three cases. For the Fmmm RTO phase, the orthorhombic feature is basically lost in the simulated FM structure. The **a** and **b** lattice constants calculated for the simulated FM structure only differs by 0.00004 Åwhich is negligible. The simulation using the AFM magnetic structure replicates this feature much better. Based on this, it looks like the

distortion observed in the orthorhombic RTO La_2NiO_4 phase is caused by the magnetic interactions between the Ni ions. It is noted that the calculated HTT I4/mmm phase with the AFM magnetic structure agrees with the experimental values much better than the calculated structure with the NM magnetic ordering. In the experiments, this HTT phase only appears above 400 K. This temperature is much higher than the Neel temperature (330 K) of the La_2NiO_4 material and the HTT phase should always be paramagnetic in bulk. However, as suggested by our results, the AFM magnetic ordering should still be used for the DFT simulation to obtain sensible results. As mentioned earlier, the short-range magnetic order may still be there in the small simulation cells, even though the long-range magnetic order does not exist any more in the bulk samples.

While evaluating the errors between the calculations and the experiments, it is also important to recognize temperature's contribution to the errors. All the DFT simulations are carried out at 0 K, while the experimental lattice constants are measured at different temperatures. It is known that the B3LYP hybrid functional employed tends to overestimate lattice constants, as the partially mixed Hartree-Fock exchange tends to underestimate bonding strength. When not considering the error due to thermal expansions, the high-temperature phases' simulation results presented in table 4.2 looks like reproducing experiments better. However, this apparent improvement is almost exclusively caused by the lattice thermal expansion in this case. Pure La_2NiO_4's thermal expansion coefficient (TEC) is reported to be around $14.4 \times 10^{-6}K^{-1}$ up to 1200 K.[99] As an example, we can take this TEC value and calculated an extrapolated thermally expanded lattice constants at 700 K (experimental temperature) based on our calculated lattice constants of g-type HTT (I4/mmm) La_2NiO_4. The projected expanded lattice constants will be a = 3.964 Åand c = 12.961 Å. Calculating the errors with respect to the experiment again, we get 2.05% overestimation for a and 1.63% overestimation for c. Now this new error of 2.04% for lattice constant a of the HTT phase is very close to the low temperature phases error of 1.91%. Similarly, the temperature corrected RTO Fmmm lattice constants will give an error of 1.85% for a and b at 273 K (experimental temperature). Both temperature corrected errors are very close to the low temperature phase's calculated error of 1.91%. Therefore, we can see the importance of thermal expansion correction when comparing the DFT calculated lattice

constants and experimental lattice constants measured at room temperature or higher. It is also noticed that the c lattice constants are still having smaller errors comparing to the a and b parameters. This difference is caused by a known anisotropic expansion in the xy plane and z direction of the La_2NiO_4, as observed in experiments[99].

Some of the La_2NiO_4 material's properties like the band gap and magnetic coupling constants have been calculated to see if the simulation setups will affect property predictions. The stoichiometric La_2NiO_4 material's band gap has been measured at room temperature and is at least 4 eV[36]. Since the measurement was done at room temperature, only the band gaps of the FM and the AFM RTO phases are calculated in our study. Both band gaps are found to be indirect. The FM RTO phase's calculated band gap is 2.48 eV while the AFM RTO phase's calculated band gap is 3.57 eV. The calculated AFM RTO band gap is close to the experimental optical band gap. Our simulation's result agrees way better with the experiments than literature computational results based on the local density approximation which predicted La_2NiO_4 to be a metal[31,100]. This suggests the necessity to use the hybrid functional to correctly predict the La_2NiO_4 material's electronic properties.

To calculate the magnetic coupling constants, J, we followed the method used by Feng and Harrison[75,101]. The magnetic coupling constant J based on a simple Ising model is given by

$$J = \frac{\Delta E}{s^2 Z} \tag{4.1}$$

where ΔE is the energy difference per magnetic ion between the FM and the AFM phases, s is the spin (1 for Ni^{2+} ion) and Z is the number of nearest magnetic ions (4 in the case of La_2NiO_4 since it is a 2D antiferromagnet). The calculated magnetic coupling constants are listed in table 4.3 together with some literature computational and experimental values. From the results, we can see that, in addition to the DFT approximation method used, the input structure will also affect the calculated magnetic coupling constants significantly. Our result calculated using the relaxed P42/ncm phase and B3LYP functional agrees with experimental J very well, and overestimates much less than the value calculated from the I4/mmm phase. In addition to the modified B3LYP (using 35% Hartree-Fock exchange in stead of 20%) calculation, Feng also

Table 4.3: The magnetic coupling constant (J) calculated are listed in milli-electronvolt. The experimental value reported was measured at 35 K. The Néel temperature measured for the ideal La_2NiO_4 is 328 K. The literature simulation results were calculated using unrestricted Hartree-Fock method and a modified B3LYP functional (mixing 35% Hartree-Fock exchange instead of 20%). The literature calculations used the I4/mmm experimental structure without geometric optimisation.

Space Group	Mag. Config.	B3LYP	UHF	35% HF	Exp.
P42/ncm	AFM	32.97	-	-	31 (at 35 K)[34]
Fmmm	AFM	36.84	-	-	-
I4/mmm	AFM	36.81	9.2[102]	27.51[101]	-

used the standard B3LYP to calculate the magnetic coupling constant using the unrelaxed experimental I4/mmm structure. He got a magnetic coupling constant of 40.65 meV from that calculation[101]. In our case, the result obtained from the optimised I4/mmm structure is only 36.81 meV and is 3.84 meV less than Feng's unrelaxed structure's result. It is noted that the I4/mmm phase calculated is actually not the correct low temperature phase measured in the experiments. The experimental magnetic coupling constant is measured at 35 K and is measuring the P42/ncm phase rather than the I4/mmm phase using neutron scattering[34]. The exceptional agreement between our calculated result and corresponding experimental value is very interesting as the B3LYP functional usually overestimates the coupling constant by 30% or more for other materials[101]. As the magnetic coupling constant is not a major topic of this thesis, we will not go into the details to find out why this happens. Nonetheless, this finding suggests that it may be quite important to use the appropriate input structure to avoid unnecessary errors if we want to compare our simulation results to the experiments.

It is very common to evaluate the quality of the magnetic model by comparing the calculated and experimental Néel temperature. The Néel temperature of the ideal La_2NiO_4 determined in the experiment is 328 K, by evaluating the temperature evolution of the magnetic Bragg reflection intensity[34]. A simple mean field approximated 2D Ising model with 4 nearest neighbours can be used to calculated the Néel temperature, T_N , from the magnetic coupling, J as follows:

$$k_B T_N = \frac{4}{\ln(1+\sqrt{2})} J \tag{4.2}$$

This simple approximation will give a severely overestimated Néel temperature (about 816 K)

even if the experimental J is used for the La_2NiO_4 material. Although it is well known that the 2D Ising model will overestimate the Néel temperature by 1.5 - 2 times, the approximation is quite bad in the case of La_2NiO_4. Using a standard mean field approximated 2D classical Heisenberg model also gives little improvement on this problem. This significant discrepancy at relatively higher temperatures (close to T_N) is believed to be mainly due to the quantum mechanical behaviours, e.g. the correlation effects, which is omitted in the classical models[103]. More sophisticated model, like the 2D quantum non-linear sigma model, has been adapted to address this problem. The most successful adaption is done by Chakravarty, Halperin and Nelson (CHN).[104,105] Nakajima *et al.* have used the CHN solution to calculate a 2D Ising phase transition temperature of 305 K, which is very close to the reported T_N of 328 K. Nakajima_{1995} Nakajima *et al.* also suggested that this small difference is due to the weak inter-planar spin interaction.

In addition to the magnetic properties, we have also briefly looked at the electronic structure of the La_2NiO_4 materials by plotting their density of states (DOS). In Fig. 4.1 and 4.2, it is clear that forcing the ferromagnetic ordering will cause a significant decrease of bandgaps in all the three phases, due to extra up-spin Ni 3d orbital states which shifts the top of valence bands to higher energy levels. Correspondingly, the unoccupied down-spin Ni 3d orbital states become significant lowlying conduction bands in the FM calculations. In the AFM cases, the top of the conduction bands consist of Ni 3d states and O 2p states, while La atoms give little contribution to the states just below the Fermi energy. Comparing the bandgaps shown in Fig. 4.2, it is easy to see that the room temperature Fmmm phase/structure is giving a bandgap that is closest to the experimental optical bandgap of 4 eV at room temperature. As most of the experiments on the La_2NiO_4 material are conducted at room temperature, we decide to use the AFM RTO La_2NiO_4 setup for the La_2NiO_4 simulations so that the calculated results are more comparable to the experiments.

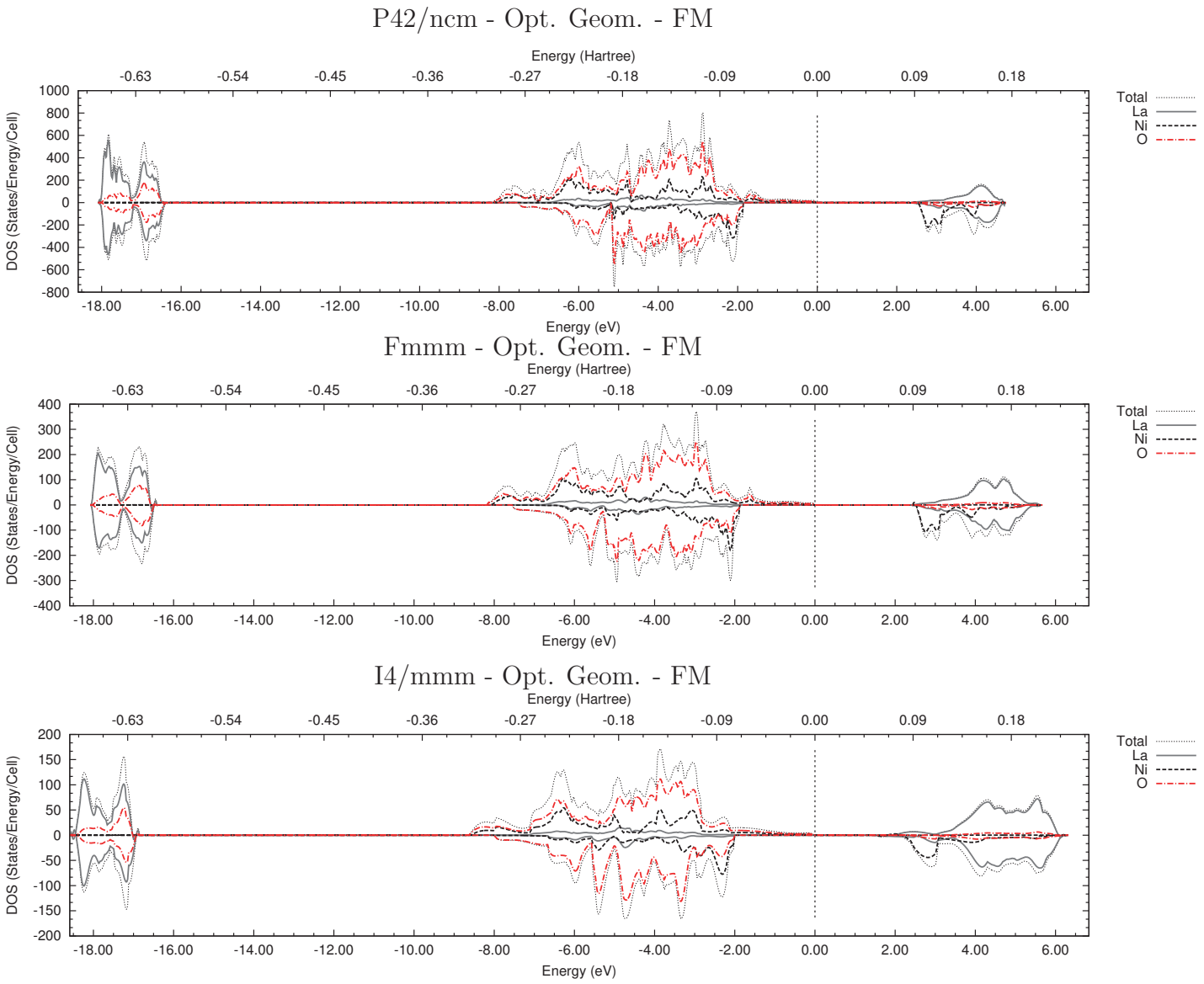


Figure 4.1: Density of states map for the low temperature (P42/ncm), room temperature (Fmmm) and high temperature (I4/mmm) phases of La_2NiO_4 with ferromagnetic ordering. The gray line is for La, the black line is for Ni and the red line is for O. The Fermi energies are marked as zero on the energy axes.

4.3 La defect formation energy

After the simulation setups are decided, we can start to evaluate the La defect formation energy and La diffusion energy. As mentioned in chapter 2, a defect's formation energy is given as

$$E^f_{def} = E_{def} - E_{ideal} - \mu_{def} - q\mu_e \tag{4.3}$$

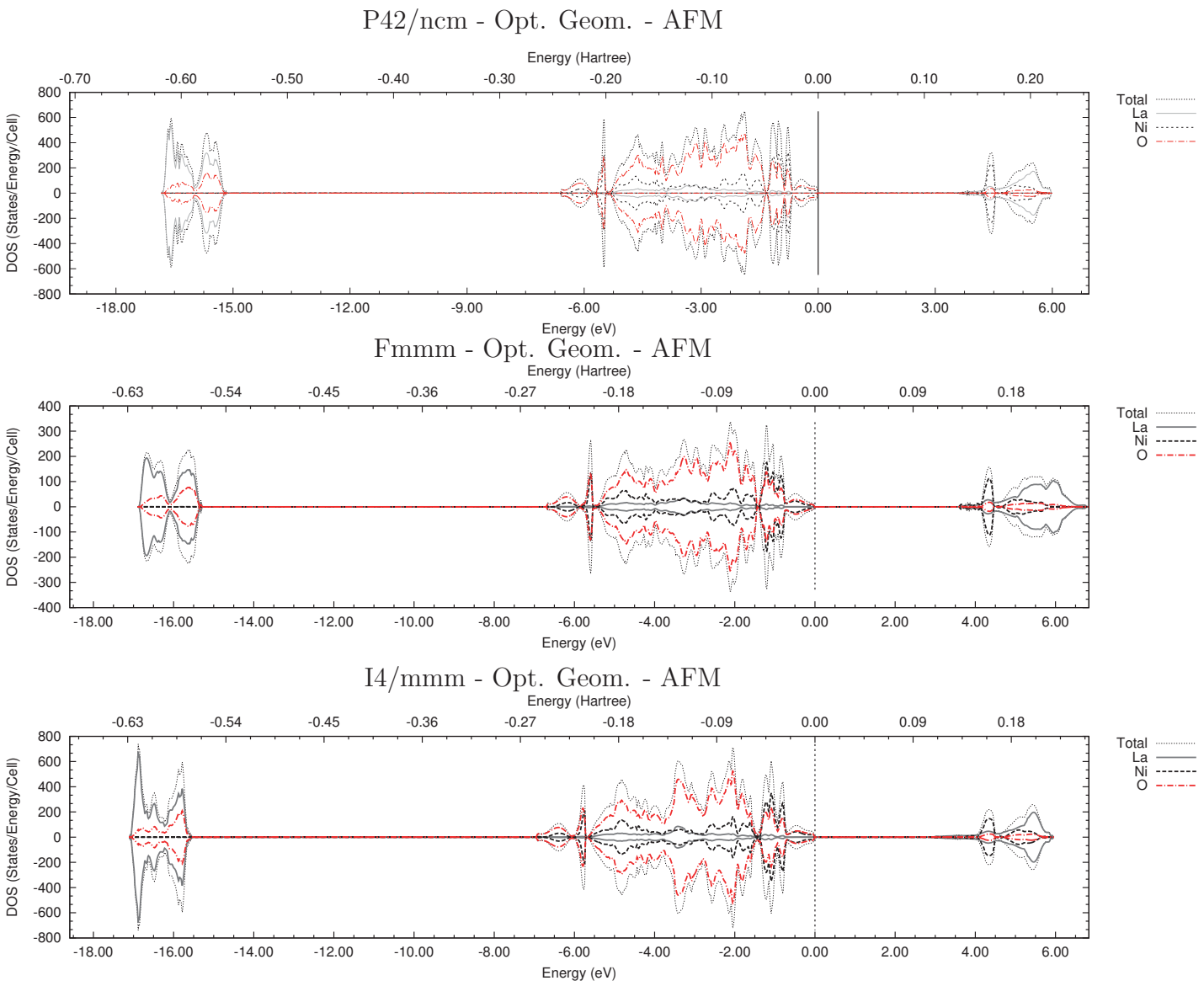


Figure 4.2: Density of states map for the low temperature (P42/ncm), room temperature (Fmmm) and high temperature (I4/mmm) phases of La_2NiO_4 with antiferromagnetic ordering. The gray line is for La, the black line is for Ni and the red line is for O. The Fermi energies are marked as zero on the energy axes.

where E^f_{def} is the formation energy of the defect, E_{def} and E_{ideal} are the total lattice energies of the defective cell and ideal cell respectively, μ_{def} is the chemical potential of the defect atom, q is the charge associated with the defect and μ_e is the electron chemical potential. In this study, we only consider neutral defects, so the charge q is always zero and the last term vanishes.

4.3.1 Calculations of metal chemical potentials

Based on the defect energy equation, E_{def} and E_{ideal} can be easily calculated from DFT simulations. However, the evaluation of a metal defect's chemical potential, μ_{def}, is not as straightforward when we are using the hybrid DFT approximations. As mentioned in chapter 2, the hybrid functional has difficulty to give accurate energetic reference states for metals due to the exact Fock exchange it contains. Therefore, the La chemical potential is calculated indirectly by using the Gibbs formation energies of its oxides instead. Equation 2.9 in chapter 2 gives the Gibbs formation energy of oxides generally. For La metal, its chemical potential μ^0_{La} at standard condition (298 K and 1 atm pressure) is calculated using the following equation:

$$\Delta G^0_{f\mathrm{La_2O_3}} = \mu_{\mathrm{La_2O_3}} - 2\mu^0_{La} - \frac{3}{2}\mu^0_O \tag{4.4}$$

where $\Delta G^0_{f\mathrm{La_2O_3}}$ is taken from literature experimental value[93], μ^0_O is determined by combining the ground state DFT calculated μ_O (0K) and the empirical oxygen gas chemical potential change due to rising temperature from the NIST database as discussed in chapter 3; $\mu_{\mathrm{La_2O_3}}$ can be equated to the ground state energy calculated with DFT.[106] The Ni chemical potential can be calculated similarly from the experimental Gibbs formation energy of its related compounds. It is noted that some of the Ni^{2+} ions are probably oxidized into Ni^{3+} ions to maintain charge neutrality in defective La_2NiO_4. Therefore, an average Ni chemical potential of both Ni^{2+} and Ni^{3+} should be obtained from the experimental Gibbs formation energies of NiO[107](Ni^{2+}) and $LaNiO_3$[92](Ni^{3+}). To check the reliability of the standard La and Ni chemical potentials calculated this way, we calculated and compared the theoretical Gibbs formation energies of La_2NiO_4, $La_3Ni_2O_7$ and $LaNiO_3$ at standard conditions to their literature experimental values. The calculation methods follow Eqn. 4.4 and the ground state energies of La_2NiO_4, $La_3Ni_2O_7$ and $LaNiO_3$ are calculated using hybrid DFT simulations. The results are summarized in table 4.4. From the table, we can see that the agreement between our approximation and literature experiments is not bad. The error for $LaNiO_3$ is significantly larger than the other two materials calculated. It is probably because that the Ni chemical potential used is an average value of Ni^{2+} and Ni^{3+} while only Ni^{3+} is present in $LaNiO_3$. In thermodynamic experiments, La_2NiO_4 will

Table 4.4: Comparison of calculated and experimental Gibbs free energy of formation (eV per formula unit) of relevant La-Ni-O Ruddlesden-Popper materials. The experimental Gibbs free energy of formation are measured at 298.15 K.

Compound	Experimental ΔG_f^0 (eV)	Calculated ΔG_f^0 (eV)	Error	Reference
La_2NiO_4	-21.616	-21.846	1.06%	[92]
$La_3Ni_2O_7$	-34.582	-34.381	-0.58%	[92]
$LaNiO_3$	-12.859	-12.088	-5.99%	[92]

absorb some oxygen and contain some Ni^{3+} unless in an oxygen-free atmosphere. Hence, the error for the calculated La_2NiO_4's Gibbs energy of formation is smaller than for $LaNiO_3$, even though stoichiometric La_2NiO_4 should only contain Ni^{2+} and cause larger errors. In summary, it is sensible to use the approximated standard La chemical potential to calculate the defect formation energies in La_2NiO_4.

After we obtained the standard La chemical potential, we are still not ready to calculate the La vacancy defect formation energy yet. In a compound, the standard chemical potential (μ_i^0) only determines the upper limit of the chemical potential (μ_i) that is allowed if the compound may exist stably. The lower stability limit must also be obtained. It is known that

$$\mu_i - \mu_i^0 \leq 0 \tag{4.5}$$

and we can define

$$\Delta\mu_i = \mu_i - \mu_i^0 \tag{4.6}$$

By combining these two equations, we will have

$$\Delta\mu_i \leq 0 \tag{4.7}$$

This change of variable can be convenient, as the following equation

$$\mu_{La_2NiO_4} = 2\mu_{La} + \mu_{Ni} + 2\mu_{O_2} \tag{4.8}$$

can be re-expressed as

$$\Delta G^0_{fLa_2NiO_4} = 2\Delta\mu_{La} + \Delta\mu_{Ni} + 2\Delta\mu_{O_2} \tag{4.9}$$

by deducting μ_{La}, μ_{Ni} and μ_{O_2} with their stoichiometric coefficients from both sides of Eqn. 4.8. From this equation, we can see that any of the element's $\Delta\mu_i$ cannot be so small that the value will force the other elements' $\Delta\mu_i$ to exceed 0. Therefore, the range of possible $\Delta\mu_i$ for any of the elements in La_2NiO_4 is

$$\frac{1}{x_i}\Delta G^0_{f\mathrm{La_2NiO_4}} \leq \Delta\mu_i \leq 0 \tag{4.10}$$

where the $\Delta G^0_{f\mathrm{La_2NiO_4}}$ can be calculated as mentioned in the previous paragraph.

From our calculated energies, the range of La, Ni and O chemical potentials in La_2NiO_4 are

$$-869.463\,eV \leq \mu_{La} \leq -858.540\,eV \tag{4.11}$$

$$-41063.667\,eV \leq \mu_{Ni} \leq -41041.822\,eV \tag{4.12}$$

$$-4100.820\,eV \leq \mu_{O_2} \leq -4089.897\,eV \tag{4.13}$$

These chemical potentials may be further limited by the chemical potentials of related binary compounds (La_2O_3 and NiO) in this case) when the binary compound can coexist with Ni or La element and allows lower La or Ni chemical potential respectively. Therefore, two energetic phase diagrams are plotted using the calculated Gibbs formation energies of La_2O_3 and NiO respectively as shown in Fig. 4.3. The La energetic phase diagram is plotted by assuming all phases are in equilibrium with a rich Ni reservoir, and the Ni energetic phase diagram is plotted by assuming all phases are in equilibrium with a rich La reservoir. From Fig. 4.3, we can see that the upper limit of the La chemical potential in La_2NiO_4 is limited by the competing La_2O_3 phase under a reducing environment (low oxygen chemical potential). On the other hand, the possible range of the Ni chemical potential in La_2NiO_4 is not affected by the NiO phase at all. Based on these results, we now have a new range of stable La chemical potential in La_2NiO_4 which is

$$-869.463\,eV \leq \mu_{La} \leq -863.777\,eV \tag{4.14}$$

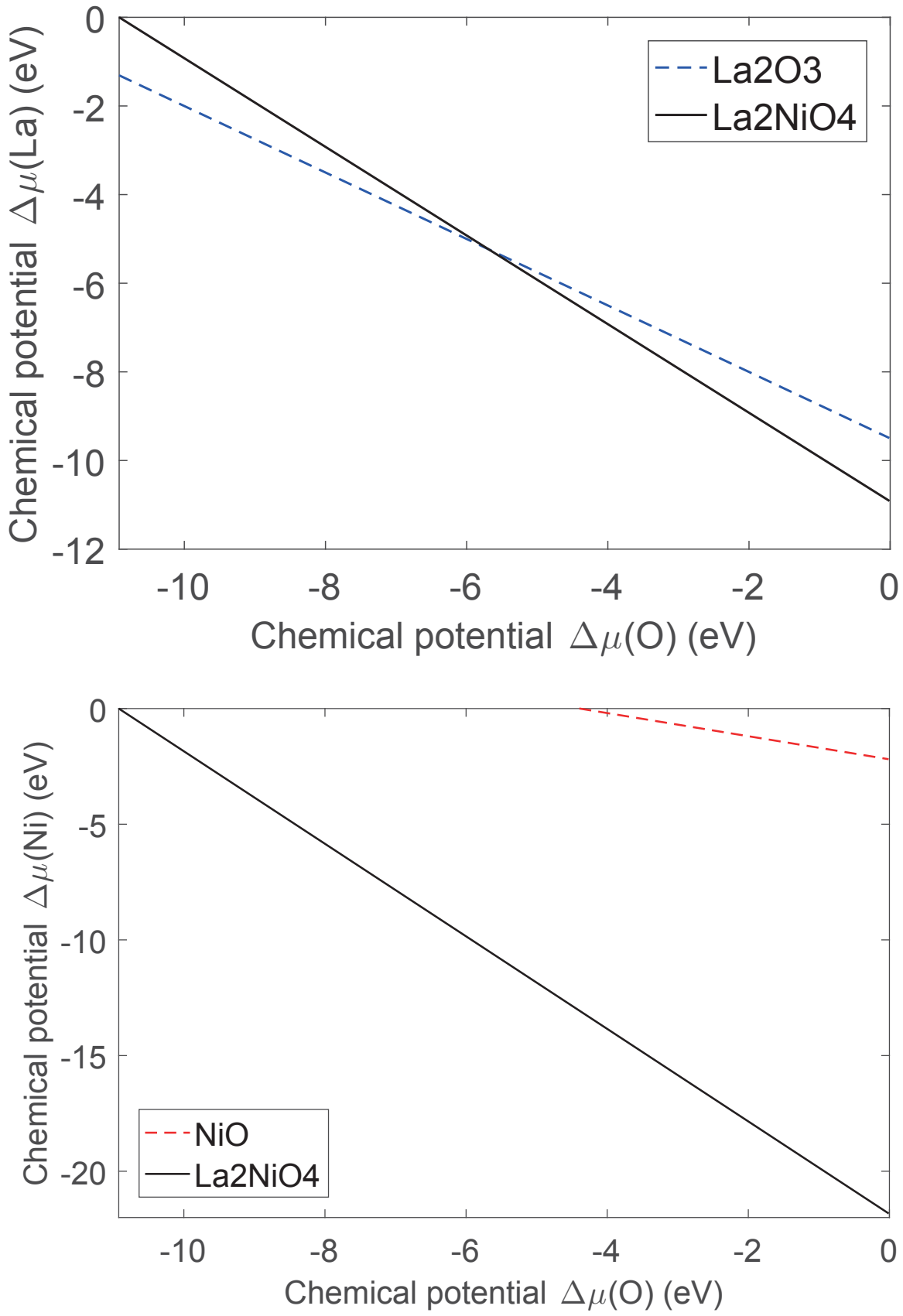


Figure 4.3: Two dimensional phase diagrams plotted using calculated Gibbs formation energies of La_2NiO_4, La_2O_3 and NiO. Top is the La energetic phase diagram. Bottom is the Ni energetic phase diagram. The regions above the La_2NiO_4 line and below the La_2O_3 or NiO line are the La_2NiO_4 stability regions in both diagrams.

The defective $La_{1.875}NiO_4$'s lattice energy is calculated using a $2 \times 1 \times 1$ La_2NiO_4 supercell in which one La atom is replaced with a 'ghost' atom (detailed in section 3.3). As all the La sites in La_2NiO_4 are symmetrically equivalent, it does not matter which La is removed. This defective supercell contains 55 atoms. The charge neutrality is maintained by promoting Ni^{2+} ions to Ni^{3+} ions. This defective lattice energy is then used together with our La chemical potential previously determined to give the range of La vacancy formation energy. This range of La vacancy formation energy is -2.14 eV to 3.55 eV per defect. Since this is the first time the La vacancy formation energy is calculated in defective La_2NiO_4, there is no literature results available for comparison. To have a better grasp of the magnitude of the La vacancy formation energy, we can compare it to the oxygen interstitial formation energy which has been studied well. Assuming the charges of the oxygen ions are compensated by the oxidation of Ni ions, the oxygen interstitial formation energy calculated by Minervini is -6.63 eV per defect in this case[48]. Our calculated range of La vacancy defect energy is significantly larger than the literature oxygen interstitial formation energy. This suggests that it is can be difficult for the La_2NiO_4 to lose many La atoms and contain a large number of La vacancies. A small number of La vacancies may be present in La_2NiO_4 though, as the lower end of our computed La vacancy formation energy range is still negative. This lower end value may be satisfied if the material is under a very oxidizing condition and the oxygen chemical potential is very high. In addition, we have calculated the oxygen interstitial formation energy using the total lattice energy of $La_2NiO_{4.25}$ and the oxygen chemical potential calculated in this chapter and previous chapter. As a confidence check, we compared our calculated oxygen interstitial formation energy with Minervini's one. The oxygen interstitial formation energy we obtained in $La_2NiO_{4.25}$ is -6.02 eV per interstitial at standard conditions and agrees well with Minervini's literature value. This again shows the reliability of our method which combines the hybrid DFT method and classical thermodynamics.

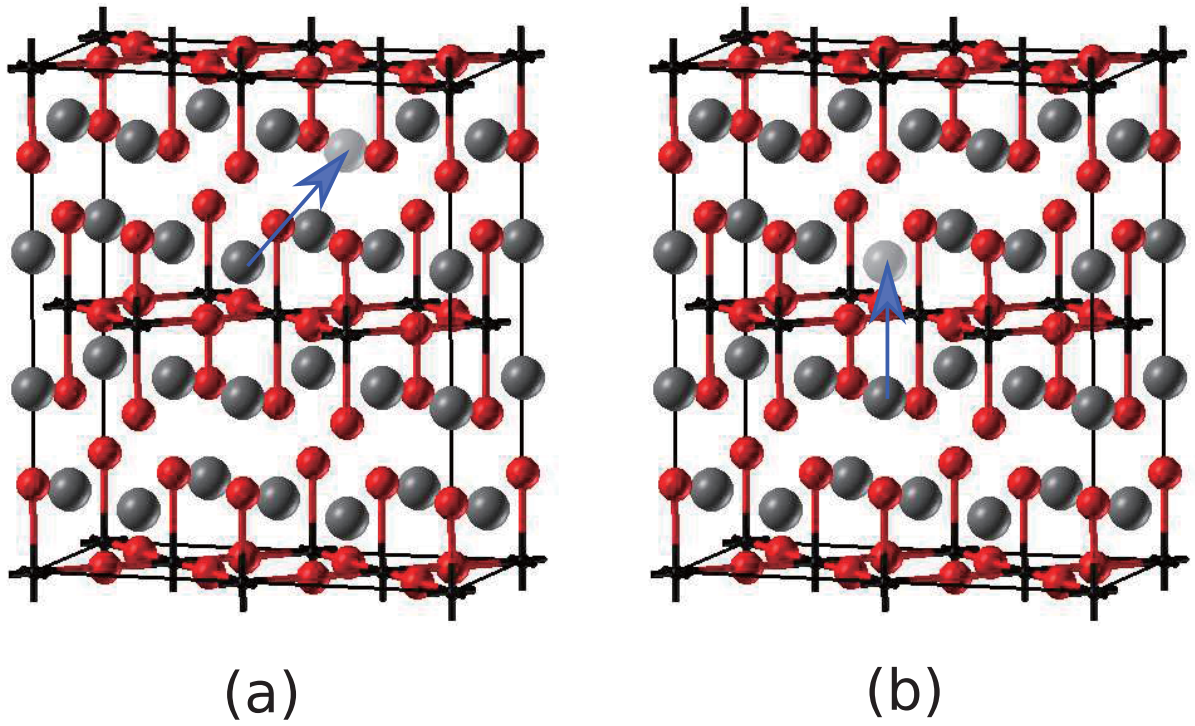


Figure 4.4: Schematics of two La diffusion pathways via vacancy mechanism in a LNO214 2×1×1 supercell with one La vacancy. In the figure, grey is La atom, black is Ni atom and red is O atom. The semi-transparent atom represents La vacancy. (a) shows the La migration pathway in the rocksalt layer. (b) shows the La migration pathway in the perovskite layer.

4.4 La vacancy migration energy in La_2NiO_4

As noted earlier, for the LNO214 structure to decompose and form extra La_2O_3 layers, La atoms need to diffuse to the surface. As an activated process, this diffusion has an associated activation energy. This activation energy is effectively the La vacancy migration energy barrier. Based on the transition state theory, this La vacancy migration energy barrier can be calculated by finding the minimum intermediate state or structure's energy during the La migration process. There are a few different transition state search methods available. One of the most commonly used methods is the Nudged Elastic Band (NEB) method[108] which only requires the knowledge of the reaction's initial state, final state and calculated potential energy surface's gradient.

In this study, we used the Distinguished Reaction Coordinates (DRC) method[109], as embedded in the CRYSTAL14 software package, to calculate the La diffusion's transition state's energy. The DRC method uses two steps to locate the transition state (TS): firstly it uses a rough scan to define a structure as close as possible to the TS, and secondly it optimises this structure

to obtain the actual TS. For the first step, we scan the energies of structures along a selected internal coordinate (in this case the La-Vacancy distance). This selected internal coordinate is then our distinguished reaction coordinate. During this scan, the distinguished reaction coordinate is fixed at each of the optimisation point and the other internal coordinates are relaxed to obtain a pseudo-relaxed structure at each point. By plotting the lattice energies of the pseudo-relaxed structures against the La-Vacancy distances, we can find a high energy region which corresponds to the TS region. The pseudo-relaxed structure with the highest energy is then used as the initial guess of the TS optimization step. For the TS optimization step, the initial Hessian matrix of the guess structure must be calculated to give the correct direction of optimization. The self-consistent field optimization's convergence tolerance criterion is also tightened to 10^{-11} Hartree to ensure the calculation's reliability.

It is noted that La diffusion in La_2NiO_4 has two paths with different surrounding environments despite all the La sites being symmetrically equivalent. These two paths occur in the rock-salt LaO layer and the perovskite $LaNiO_3$ layer respectively, as shown in Fig. 4.4. We have computed the activation energy of these two possible diffusion steps. We obtain a barrier height of 4.31 eV for the rock-salt path, and a height of 4.57 eV for the perovskite path. Although no experimental cation diffusion data for La_2NiO_4 is available, our calculated value for the perovskite layer (4.57 eV) is comparable to the La diffusion activation energy of 4.98 eV in $LaCrO_3$.[110] Comparing to the oxygen diffusion activation energy (0.88 eV)[15] in single crystal La_2NiO_4, the La diffusion activation energy is about five times as large. Assuming a simple Arrhenius relationship between the diffusion rate and diffusion activation energy, we can estimate that La diffusion rate is at least 3 orders of magnitudes smaller than O diffusion rate. That might be part of the reason behind the limited decomposition.

4.5 Conclusion

In this chapter, some of the possible defects in La_2NiO_4 are examined using hybrid density functional methods. Before the defects calculations, various input structural phases and magnetic

orderings of the La_2NiO_4 are tested to evaluate their impact on the DFT simulation results. It has been found that many calculated properties like relaxed lattice constants, band gaps and magnetic exchange coupling constants are significantly affected by the choice of input La_2NiO_4 structures and magnetic orderings. When comparing the calculated results to experimental data, the choice of input setups can be a major source of error in some cases. By considering our simulation target and the conditions used in available experimental studies, the room temperature orthorhombic La_2NiO_4 phase and the g_x type AFM magnetic ordering are selected as the simulation setups throughout this study.

To calculate the La defect formation energy in La_2NiO_4, the chemical potential of the metal La must be calculated in addition to the defective lattice's total energy. The hybrid density functional has innate limitations when describing metals due to the exact Hartree-Fock exchange included. Therefore, the chemical potential of the metal La can only be calculated indirectly by considering the experimental and calculated Gibbs formation energies of related compounds like La_2O_3, NiO and $LaNiO_3$, as suggested by Ahmad *et al.*[72]. To confirm the reliability of the La and Ni chemical potentials obtained this way, the Gibbs formation energies of $LaNiO_3$, La_2NiO_4 and $La_3Ni_2O_7$ at the standard conditions are calculated using these chemical potentials and compared to experimental values. The comparison has shown that the calculated Gibbs formation energies agree well with literature experimental values. Based on this knowledge, a range of La chemical potentials which allows the stable existence of the La_2NiO_4 are calculated. The range of possible La vacancy formation energies are calculated by combining the DFT calculated defective La_2NiO_4 lattice energy and the range of La chemical potentials obtained previously. Unfortunately, there is no other experimental or simulated La vacancy energies in defective La_2NiO_4 available for comparison. Therefore, we also calculated the oxygen interstitial formation energy in $La_2NiO_{4.25}$ so that we may have an idea on how difficult the formation of La vacancy is. The results show that it is much more difficult for the La vacancy to form compared to the formation of an oxygen interstitial in La_2NiO_4 material, which agrees with our expectation.

The La diffusion barrier via the vacancy mechanism is also calculated to investigate how difficult it is for the La to move around in this material. The La-deficient La_2NiO_4 structures optimised

previously are used to calculated the transition states. It is found that there are two paths by which the La atom can diffuse in the La_2NiO_4 material: one is between the neighbouring La sites within the rock-salt like LaO layer, the other is between the neighbouring La sites within the perovskite $LaNiO_3$ layer. Both diffusion barriers are calculated using the Distinguished Reaction Coordinates method embedded in the CRYSTAL14 package. The calculated rock-salt La diffusion barrier is 4.31 eV, while the calculated perovskite barrier is 4.57 eV. As these La diffusion barriers are calculated for the first time, there are no literature results available for comparison. However, the La diffusion barrier in a similar perovskite material $LaCrO_3$ has been calculated to be 4.98 eV[110], which is higher but still comparable to our calculated La diffusion barrier in the perovskite $LaNiO_3$ layer. The difference between the results is probably due to lower electronic repulsion in the La_2NiO_4 material, as there is higher proportion of negative oxygen ions in the La_2NiO_4 than in the $LaCrO_3$. Comparing to the Ni^{2+} ionic radii (about 0.6 Å) for, the larger ionic radii of the Cr^{2+} ions (about 0.7 Å) should also make it more difficult for the La ion to move around[111]. The literature oxygen interstitial diffusion activation energy is 0.88 eV[15] and our La diffusion activation energy is about 5 times this. By assuming an Arrhenius relationship between diffusion rates and diffusion barriers, our estimation suggests that the La diffusion rate is at least 3 orders of magnitudes smaller than the O diffusion rate in La_2NiO_4 materials. Therefore, it is quite possible that the slow rate-determing La diffusion step limits and prevents the complete decomposition of La_2NiO_4.

Chapter 5

Oxygen diffusion in $CeNbO_{4.25}$

Part of this work has been published and reprinted with permission from Pramana, Stevin S., Baikie, Tom, An, Tao, Tucker, Matthew G., Wu, Ji, Schreyer, Martin K., Wei, Fengxia, Bayliss, Ryan D., Kloc, Christian L., White, Timothy J., Horsfield, Andrew P., Skinner, Stephen J. Correlation of Local Structure and Diffusion Pathways in the Modulated Anisotropic Oxide Ion Conductor $CeNbO_{4.25}$. J. Am. Chem. Soc. 138, 12731279 (2016). Copyright 2016 American Chemical Society.

5.1 Introduction

In the past few years, materials with oxygen hypostoichiometry stirred interests in the solid state ionics community due to the low diffusion activation energy of their interstitial oxygen ions. This property has been demonstrated in a number of different materials and structures, including Ruddlesden-Popper materials like aforementioned La_2NiO_4[13,14] and Pr_2NiO_4[112], melilites like $La_{1+x}Sr_xGa_3O_{7+x/2}$[113,114], oxides like Ce(V,Ta)$O_{4+\delta}$[115–118], as well as doped and undoped lanthanide silicate and germanate apatites[119]. Comparing to the oxygen vacancy transport mechanism commonly found in high-symmetry ionic material like the yttria-stabilised zirconia fluorite and mixed ionic electronic conductors (MIECs) such as $La_{1-x}Sr_x$(Co,Mn,Fe)$O_{3-\delta}$[120], the interstitial based diffusion mechanism opens a new route to explore oxygen-rich low-symmetry

materials as novel ionic conductors or MIECs. The low-symmetry $CeNbO_{4+\delta}$ material is a promising prototypical candidate of the oxygen hypostoichiometric MIEC family. Under atmospheric oxygen partial pressure, the $CeNbO_{4+\delta}$ has a total conductivity of 0.030 Scm^{-1} and a remarkable oxygen self diffusion coefficient of 8.3×10^{-8} cm^2s^{-1} at 850°C[121–124]. This oxygen diffusion coefficient is comparable to the mixed-conducting $La_{1-x}Sr_xCoO3-\delta$[120]. However, $CeNbO_{4+\delta}$ still needs to improve its electronic conductivity further to qualify as a good SOFC cathode material. Despite the remarkable oxygen diffusion property exhibited by the $CeNbO_{4+\delta}$ material at a relatively low temperature, the details of its oxygen diffusion mechanism remain largely unknown. To date, no theoretical study has been performed on this problem. This is partly due to the fact that the structures of the $CeNbO_{4+\delta}$ materials, especially its oxygen-rich phases, are difficult to characterize and has not been solved completely yet. A well-solved input crystal structure is usually the pre-requisite of a sensible modelling study. In this work, molecular dynamics (MD) simulations are carried out using the $CeNbO_{4.25}$ structure recently solved by my colleagues, Pramana *et al.*[4], in an attempt to understand the oxygen diffusion mechanism of this material. The results from the computational study would certainly provide useful insights for any further optimization of this promising material.

5.2 $CeNbO_4$ and $CeNbO_{4.25}$ Crystallography

A good understanding of crystallography is always important when simulating complex solid oxide materials. In the case of $CeNbO_{4+\delta}$, it has been shown that, apart from the parent structure $CeNbO_4$, this material is able to take extra oxygen and form three hypostoichiometric phases corresponding to the formulae $CeNbO_{4.08}$, $CeNbO_{4.25}$ and $CeNbO_{4.33}$.[125,126] The stoichiometric $CeNbO_4$ structure has been determined to be a monoclinic fergusonite type structure at room temperature, using both powder neutron diffraction and single crystal X-ray diffraction[127,128]. It is also revealed that the $CeNbO_4$ fergusonite phase transforms to a tetragonal Scheelite type structure over 800 °C (or 1073 K)[127]. Despite improved ionic conductivities of the oxygen-rich $CeNbO_{4+\delta}$ materials, very limited work has been done on their structures until recently[4,129,130]. This is partly due to the alternating commensurate and incommensurate modulated structures

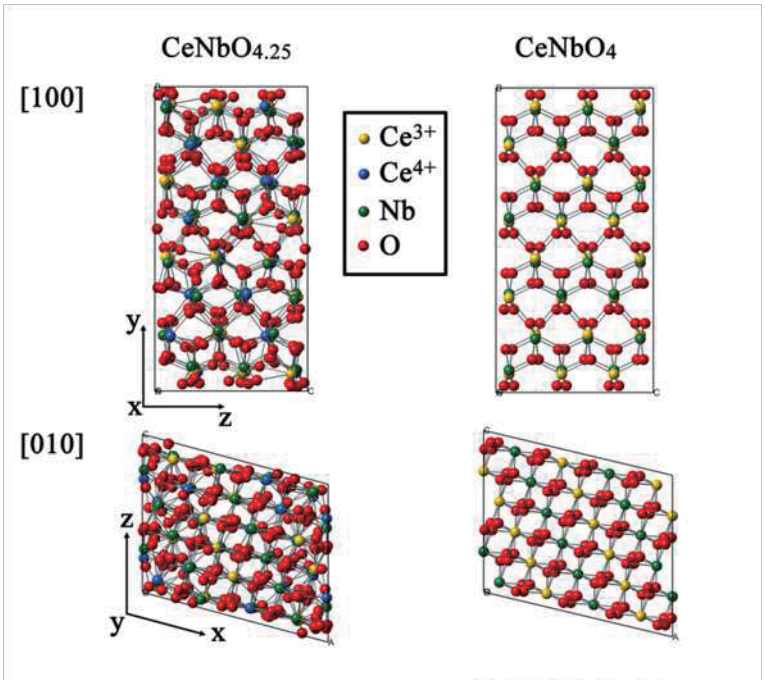


Figure 5.1: Projected crystal structures of $CeNbO_4$ (right) and $CeNbO_{4.25}$ (left)[4,128] along [100] and [010] axes are compared. The interstitial oxygens clearly distort the $CeNbO_{4.25}$ structure and symmetry is broken. Ce^{3+}, Ce^{4+}, Nb^{5+} and O^{2-} are represented with yellow, blue, green and red spheres respectively.

observed in electron microscopy studies on the $CeNbO_{4+\delta}$ materials[131]. This interesting feature, believed to be a result of the incorporation of interstitial oxygen ions, poses difficulty to structure analysis using simple powder diffraction techniques. The modulated structures may have large supercells that give rise to high reflection overlap and weak supercell reflections in powder diffraction spectra. The refinement of such diffraction spectra can be ambiguous and unreliable.

To solve this problem, Pramana *et al.* managed to grow a large single crystal of the stoichiometric $CeNbO_4$ and introduce oxygen interstitials by post heat treatment in oxidizing environments. The prepared $CeNbO_4$ and $CeNbO_{4.25}$ single crystals are examined using both neutron and high-brightness synchrotron X-ray diffraction. The long-range average structure of the materials are modelled and solved using both neutron and X-ray diffraction data. On the other hand, pair distribution function (PDF) analysis is also applied to the neutron diffraction data to determine the short range ion-ion coordination environment in the samples. The refined structures of $CeNbO_4$ and $CeNbO_{4.25}$ are shown in Fig. 5.1 and 5.2[4]. Based on Fig.

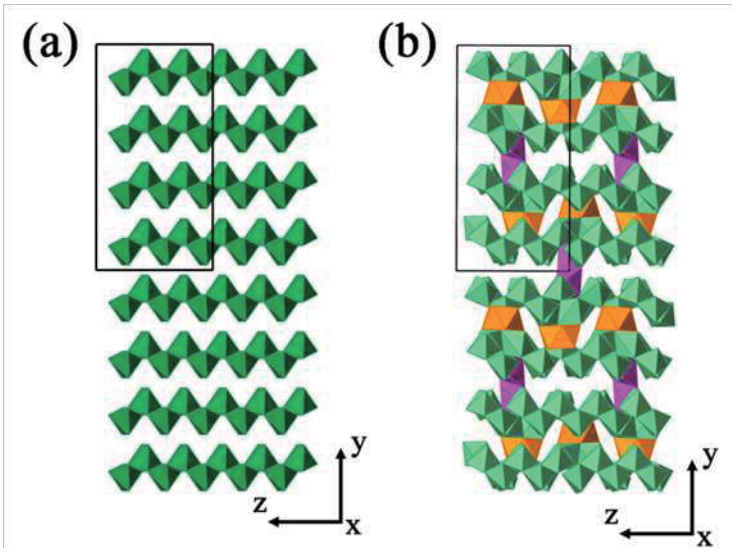


Figure 5.2: Comparison of projected crystal structures of $CeNbO_4$ (a) and $CeNbO_{4.25}$ (b) along [100] axes with polyhedra highlighted.[4] NbO_6, NbO_7 and NbO_8 polyhedra are coloured with green, purple and orange respectively. The NbO_7 and NbO_8 polyhedra are connecting different x-z planes of NbO_6 in $CeNbO_{4.25}$ and possibly enhancing diffusion by providing extra intermediate interstitial sites.

5.1, it is apparent that the $CeNbO_{4.25}$ structure is strongly distorted by the presence of oxygen interstitials compared to the parent $CeNbO_4$ structure. In Fig. 5.2, additional NbO_7 and NbO_8 are clearly shown in the $CeNbO_{4.25}$ structure while only NbO_6 is present in $CeNbO_4$. These NbO_7 and NbO_8 polyhedra accommodate extra oxygen ions and also form a kind of sinusoidal bridge between different x-z planes in the $CeNbO_{4.25}$ structure. In addition, Pramana *et al.* used the bond valence sums (BVS) method to distinguish the exact positions of the Ce^{3+} and Ce^{4+} ions. Some of the Ce^{3+} ions in the $CeNbO_{4.25}$ structure are oxidized to Ce^{4+} to compensate the extra charges of the interstitial oxygen ions. The BVS method estimates the ions' oxidation states and "bond valences" in ionic compounds by summing up all interactions up to a cutoff distance. The interactions can be calculated from observed bond lengths. In Pramana *et al.*'s work, the cutoff distance is 3 Å. This information is crucial to a successful simulation of the $CeNbO_{4.25}$ material. Due to this material's modulated structure and long-range ordering, a random allocation of Ce^{3+} and Ce^{4+} ions is not justifiable. Knowing the exact arrangements of Ce^{3+} and Ce^{4+} positions allows for better description of reality. In this work, Pramana's reported structures of the $CeNbO_4$ and $CeNbO_{4.25}$ crystals are used as input for their respective simulations[4].

5.3 Computational Details

Molecular dynamics simulation of the oxygen ion diffusion in $CeNbO_4$ and $CeNbO_{4.25}$ are carried out based on a Born-like description of the ionic lattices[56]. The initial input structure used are supercells of aforementioned $CeNbO_4$ and $CeNbO_{4.25}$ crystal structures determined by Bayliss *et al.* and Pramana *et al.*[4,128]. The $CeNbO_4$ input supercell is constructed by expanding its primitive unit cell to a 10 × 10 × 8 unit cell. The $CeNbO_{4.25}$ input supercell is a 4 × 4 × 4 unit cell expanded from its primitive cell. Both input supercells contain 19200 atoms. The interaction between ions is described by the long-range Coulombic force and the short-range Buckingham potential as explained in Chapter 2. The summation cutoff distance for the Buckingham potential is set to be 10.5 Å, as the effect of the Buckingham potential is much less significant at long range.

None of the existing pair potential sets are specifically derived and optimised to study the $CeNbO_{4+\delta}$ systems. Therefore, the Buckingham potential parameters must be selected from the literature of related systems containing Ce, Nb and O. The Ce^{3+} - O^{2-} and Ce^{4+} - O^{2-} potential parameters are extracted from the potentials used for Ce-Metal-O systems, where the metal species considered are quite broad, ranging from post-transition metals, transition metals to lanthanides[132,133]. The Nb^{5+} - O^{2-} potential is extracted from the K-Nb-O system[134]. The O^{2-} - O^{2-} potentials used in the literature Ce-Metal-O system and the literature K-Nb-O system are quite different. Therefore two pair potential sets are created and tested using different O^{2-} - O^{2-} potentials. The two potential sets are summarised in Table 5.1. The two pair potential sets constructed for the Ce-Nb-O system are then tested using 0 K relaxation calculations with the GULP package[135]. Experimental $CeNbO_4$ and $CeNbO_{4.25}$ primitive unit cells from Bayliss and Pramana are calculated. The results are shown in Table 5.2 in comparison to the experimental lattice constants obtained at room temperature. Based on the comparison, we can say that the calculated results using different pair potentials are similar to each other and both agree with the experimental values. As the simulation temperature is 0 K, it is expected that there will be some error when comparing the 0 K computed results to room temperature experimental lattice parameters. Since there are no experimental lattice parameters measured

Table 5.1: Buckingham pair potential parameters considered for relevant ion pairs. For both potential set A and B, the Ce^{3+} - O^{2-} and Ce^{4+} - O^{2-} potential parameters are taken from Vyas and Minervini's works[132,133]; the Nb^{5+} - O^{2-} potential is taken from Sepliarsky's work[134]. For the potential set A, the O^{2-} - O^{2-} potential is taken from Vyas and Minervini's works[132,133]. For the potential set B, the O^{2-} - O^{2-} potential is taken from Sepliarsky's work[134] and different from the one used in potential set A.

Potential Sets	Interactions	A_{ij} (eV)	ρ_{ij} (Å)	C_{ij} (eV Å^6)	Reference
Shared	Ce^{3+} - O^{2-}	2010.18	0.3449	23.11	[132,133]
	Ce^{4+} - O^{2-}	1809.68	0.3547	20.40	[132]
	Nb^{5+} - O^{2-}	1036.63	0.3900	0.0	[134]
Set A	O^{2-} - O^{2-}	9547.96	0.2072	32.0	[132,133]
Set B	O^{2-} - O^{2-}	3600.26	0.2834	200.0	[134]

at cryogenic temperature, it is difficult to judge whether there will be any phase transformation of the $CeNbO_4$ at low temperature. Apart from the uncertainty of possible phase change, at least some parts of the errors observed here are due to thermal effects. Both potential sets underestimate b but overestimate a and c lattice constants. This suggests that the $CeNbO_4$ material may have an anisotropic thermal expansion behaviour which needs further confirmation from experiments. Neither of the pair potential sets gives systematically better lattice constants compared to the other potential set. This also means that the pair potential sets are transferable and general to a certain extent. Therefore, the choice of pair potential sets does not affect our results significantly in this particular study. For following molecular dynamics simulations, the pair potential set A is used.

The molecular dynamics simulations for the $CeNbO_4$ and $CeNbO_{4.25}$ are carried out with the DL_POLY4 package[136,137]. Oxygen diffusions in these two structures are simulated over the temperature range of 1073 K to 2173 K. The input $CeNbO_4$ and $CeNbO_{4.25}$ supercells for molecular dynamics simulations are pre-relaxed at 0 K using the GULP package. The timestep chosen for the MD simulations is 0.001 ps. Before the production run of the MD simulation, the lattices are equilibrated for 10 ps first in the NVT ensemble (number of ions (N), cell volume (V) and temperature (T) are kept constant) then 10 ps in the NPT ensemble (number of ions (N), pressure (P) and temperature (T) are kept constant). The lattice total energies and volumes are checked respectively to ensure equilibration is reached. After equilibration, the production runs start with the equilibrated structures under the NVT conditions again

Table 5.2: Comparison of experimental and calculated lattice parameters of $CeNbO_4$ and $CeNbO_{4.25}$. The percentage differences are calculated with respect to the experimental lattice constants. The calculated lattice parameters are resulted from two different sets of pair potentials. The experimental lattice parameters are measured at room temperature. See Table 5.1 for the details of the pair potential sets' parameters.

		Experimental[4,128]	Potential Set A	Difference	Potential Set B	Difference
$CeNbO_4$	a (Å)	7.261	7.690	5.91%	7.564	4.17%
	b (Å)	11.403	11.171	-2.04%	10.867	-4.70%
	c (Å)	5.162	5.438	5.34%	5.348	3.61%
	β (°)	130.53	135.01	3.43%	135.00	3.42%
$CeNbO_{4.25}$	a (Å)	14.373	14.977	4.20%	14.782	2.84%
	b (Å)	22.792	22.462	-1.45%	21.912	-3.86%
	c (Å)	11.832	11.954	1.03%	11.753	-0.67%
	β (°)	105.07	106.69	1.54%	106.69	2.10%

and last for at least 100 ps. The ion trajectories are recorded for the production runs with an interval of 100 timesteps (0.1 ps). The first 60 ps of the data are excluded from analysis to ensure equilibrium is reached. The mean-squared displacements of the ions are calculated using the MD data. The trajectories of the ions are analyzed and visualized using the visual molecular dynamics (VMD) package[138].

5.4 Oxygen diffusion in $CeNbO_4$ and $CeNbO_{4.25}$

The mean-squared displacements (MSDs) data is the most significant indicator to determine whether diffusion has taken place or not. The oxygen ions' MSD data are calculated from the MD simulation results of both $CeNbO_4$ and $CeNbO_{4.25}$. Selected calculated oxygen MSD data at temperatures ranging from 1173 K to 1773 K is summarized and compared in Fig. 5.3. It is apparent from Fig. 5.3 that the oxygen ions in the $CeNbO_4$ structure only give local thermal vibration with the increase of temperature. The steady increase of the oxygen MSD data in the oxygen-rich $CeNbO_{4.25}$ shows that oxygen ions are displaced further away from their original position over time and indicates oxygen diffusion. On the other hand, even to the very high temperature of 1773 K, no significant oxygen displacement over time is observed in the oxygen MSDs of $CeNbO_4$ within the simulation time frame. The oxygen MSD data shown for the $CeNbO_4$ is cut earlier than that of the $CeNbO_{4.25}$ as no significant change is found after 110 ps.

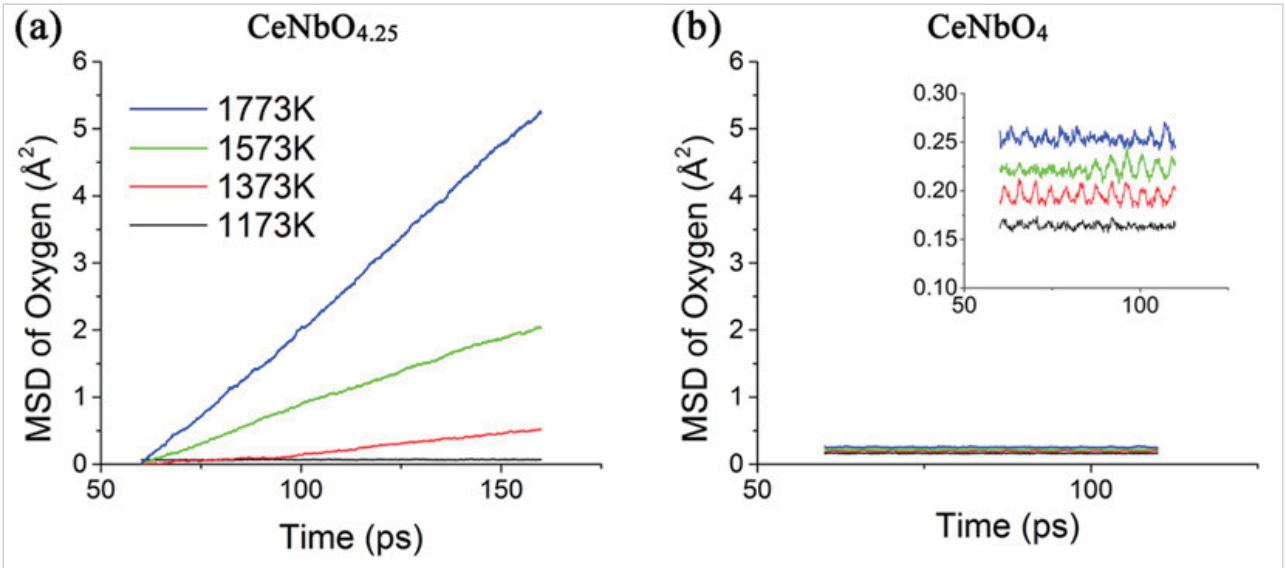


Figure 5.3: Comparison of MD calculated mean-squared displacements (MSDs) of oxygen ions in (a) $CeNbO_{4.25}$ and (b) $CeNbO_4$ materials over temperatures ranging from 1173 K to 1773K. Data from the first 60 ps are omitted to ensure equilibration and low noise.[4]

This firmly evidences that the inclusion of the oxygen interstitials is mandatory to facilitate oxygen diffusion in the $CeNbO_{4+\delta}$ materials. Any further modification and optimisation of the $CeNbO_{4+\delta}$ materials should consider this point.

The oxygen diffusion coefficients can be calculated based on the relevant MSD data too. For a system with N ions, its ion diffusivity D is linked to the MSD by

$$\frac{1}{N}\sum_{i=1}^{N}[r_i(t) - r_i(0)]^2 = 6Dt + B \tag{5.1}$$

where $r_i(t) - r_i(0)$ is the displacement of an ion from its initial position after a time t, B is the displacement due to thermal vibration near the initial position. The left hand of the equation is effectively the MSD at time t of the relevant ion. Using this equation, the diffusion coefficients of the oxygen ion in $CeNbO_{4.25}$ are calculated based on the MD MSD data over a range of temperatures. The oxygen diffusion coefficients at various temperatures are summarized and plotted on the logarithmic scale in Fig. 5.4. The data presented in Fig. 5.4 samples at more temperature points than Fig. 5.3 to ensure the diffusion coefficient's trend is shown clearly and reliably. With this graph, the diffusion activation energy of the oxygen ions can be calculated with the assumption that the oxygen diffusion is thermally activated. The Arrhenius equation

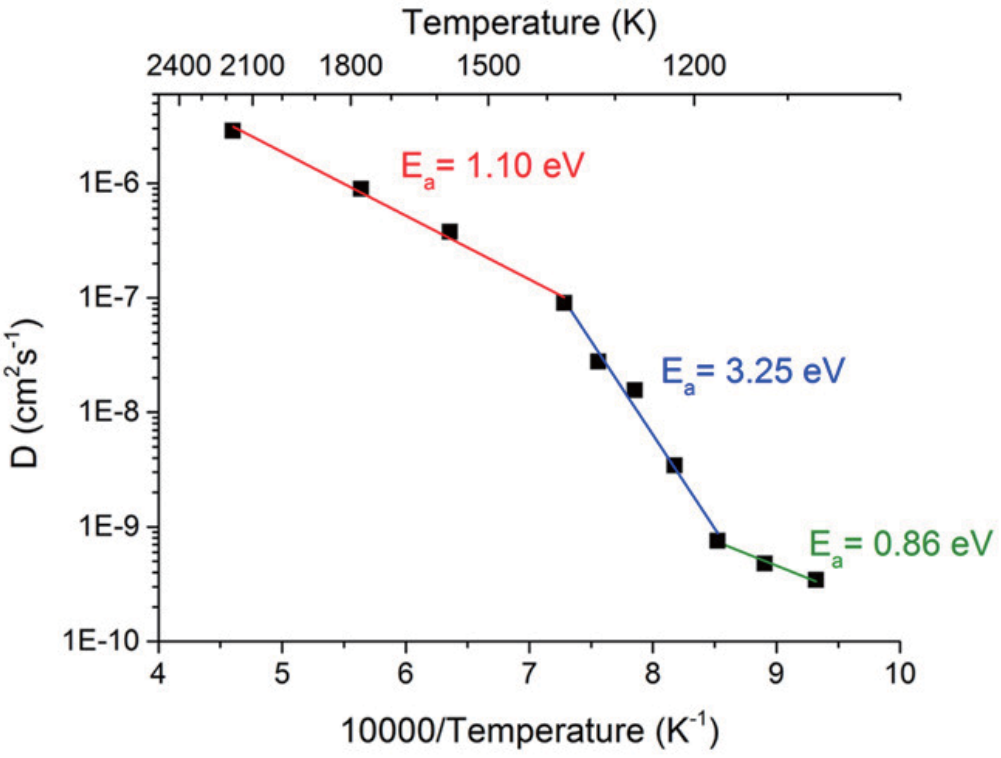


Figure 5.4: Summary of calculated oxygen diffusion coefficients in $CeNbO_{4.25}$ over a temperature range of 1073 K to 2173K. Three regions with different diffusion activation energies are labelled. Diffusions at additional temperatures are calculated to ensure the trends in all the three regions are represented reliably.[4]

gives the relationship between diffusion activation energy E_a and related diffusion coefficient D as

$$D = D_0 \exp(\frac{E_a}{k_B T}) \tag{5.2}$$

where D_0 corresponds to the maximum diffusion coefficient at infinite temperature, k_B is the Boltzmann constant and T is the temperature. The diffusion activation energy can be easily calculated from the gradient of a D-T graph on the logarithmic scale as shown in Fig. 5.4. The calculated oxygen diffusion activation energies are labelled in the same graph. A number of interesting points can be observed in Fig. 5.4. First of all, the graph show three regions with different calculated diffusion activation energies and possibly different diffusion behaviours. The significant change of diffusion activation energy is not commonly seen in other MD studies of oxygen diffusion in complext oxides. For example, MD studies on oxygen diffusions in $La_2NiO_{4+\delta}$ [19], $Pr_2NiO_{4+\delta}$ [139] and $Sr_{0.75}Y_{0.25}CoO_{2.625}$ [140] all gave straight lines in similar Arrhenius plots and temperature ranges as reported here. The temperature dependence of oxygen diffusion

activation energy should not cause such a steep change of trend in an Arrhenius plot either. Thus, this drastic change of oxygen diffusion activation energy with temperature is worth pondering. The transition region in Fig. 5.4 with calculated $E_a = 3.25eV$ may correspond to a phase change process. The temperature of this transition region (about 1100 - 1300 K) is slightly higher than the reported phase change temperature in experiments (about 1073 K)[124]. This range may correspond to the continuous and gradual change from the $CeNbO_{4.25}$ structure to the $CeNbO_{4.08}$ structure observed in experiments[124]. However, the trend of change in oxygen diffusion coefficients observed in experiments is very different or rather opposite of what we see from simulation. In the simulation results, with the increase of temperature, the oxygen diffusion becomes significantly faster after the transition temperatures, while Packer's experimental results suggest that oxygen diffusion coefficient drops by a few orders of magnitude when the temperature is above the transition temperature. A possible reason behind the differences may be the difference of oxygen content between the experimental samples and our simulation cells. In Packer's experiments, the sample is heated and tested for a time that is much longer (hours) than our simulation time-scale (hundreds of ps). The oxygen interstitials in the sample have plenty of time to adapt to the tetragonal structure and leave the material and this causes a significant drop in sample's oxygen content in reality, while this oxygen loss does not have enough time to complete during the MD simulation. As shown in Fig. 5.3, the loss of interstitial oxygen can impair oxygen diffusion in the $CeNbO_{4+\delta}$ structure heavily. Therefore, the drop in experimentally measured oxygen diffusion coefficient caused by the loss of interstitial oxygen does not happen for the simulation. With the limited available experimental and simulation data, it is difficult to firmly explain why the oxygen activation energy changes significantly around 1073 K. Further analysis of the $CeNbO_{4.08}$ structure, the oxygen diffusion simulation based on that and comparisons with the results for the $CeNbO_{4.25}$ phase may reveal more details of the transition process occuring at this temperature. On the other hand, the calculated fast oxygen diffusion in the $CeNbO_{4.25}$ phase at higher temperature might help the understanding of the oxygen movements during the phase transformation into the $CeNbO_{4.08}$ phase, as it is difficult to observe the oxygen loss and phase transformation process directly at high temperature during experiments. Such studies may suggest possible ways to stabilize the

oxygen conducting $CeNbO_{4.25}$ phase.

Secondly, the calculated diffusion coefficient in $CeNbO_{4.25}$ is significantly lower than the experimental values in the low temperature region. At 1073 K, the calculated diffusion coefficient ($\sim 10^{-9}$ cm^2s^{-1}) is about 2 orders of magnitude lower than the literature experimental value ($\sim 10^{-7}$ cm^2s^{-1})[124]. At the same time, the oxygen diffusion activation energy calculated for the low temperature region ($E_a = 0.86$ eV) is a bit lower than the experimental diffusion activation energy ($E_a = 0.99$ eV). The comparisons suggest that the thermally activated diffusion part, i.e. the diffusion rate increase with the temperature, seems to be captured well by the MD simulation. However, a systematic difference exists between the MD simulated and experimental oxygen diffusion coefficient measured with isotope exchange technique. A number of reasons may cause this difference. The experimental values presented by Packer have large error bars, as the oxygen content in the sample is dynamic, environmentally dependant and heavily affected by the measurement process itself. During the measurement, the sample would have already changed its oxygen content and no longer has an exact oxygen δ of 0.25. Another speculation is that the pair potential MD is too simple a model to reproduce the thermally independent oxygen diffusion mechanism in $CeNbO_{4.25}$. Such mechanism may be due to change in the electronic structure and polarization surrounding the mobile oxygen ions and can be captured with an electronic structure method like DFT.

The MD simulation is able to reveal possible oxygen diffusion pathways by analysing recorded ion trajectories. A number of recorded ion trajectories of both $CeNbO_4$ and $CeNbO_{4.25}$ structures are visualized and shown in Fig. 5.5. The $Ce^{3+/4+}$, Nb^{5+} and O^{2-} ions are coloured in cyan, dark blue and red respectively. Comparing the visualized trajectories of the $CeNbO_4$ and $CeNbO_{4.25}$ simulations at 673 K, it can be seen that some of the oxygen ions in the $CeNbO_{4.25}$ are already more mobile than those in the $CeNbO_4$ even at such a low temperature. Looking at the snapshots of $CeNbO_{4.25}$ trajectories at both 673 K and 1073 K, we can see that the oxygen diffusion paths concentrate in the x-z planes with interstitial oxygen ions. In the layers with less interstitial oxygen, the oxygen ions are significantly less mobile. This supports our previous argument that the presence of interstitial oxygen ions facilitate oxygen diffusion. To examine the possible diffusion pathways more clearly, an enlarged local ionic trajectory snapshot of the

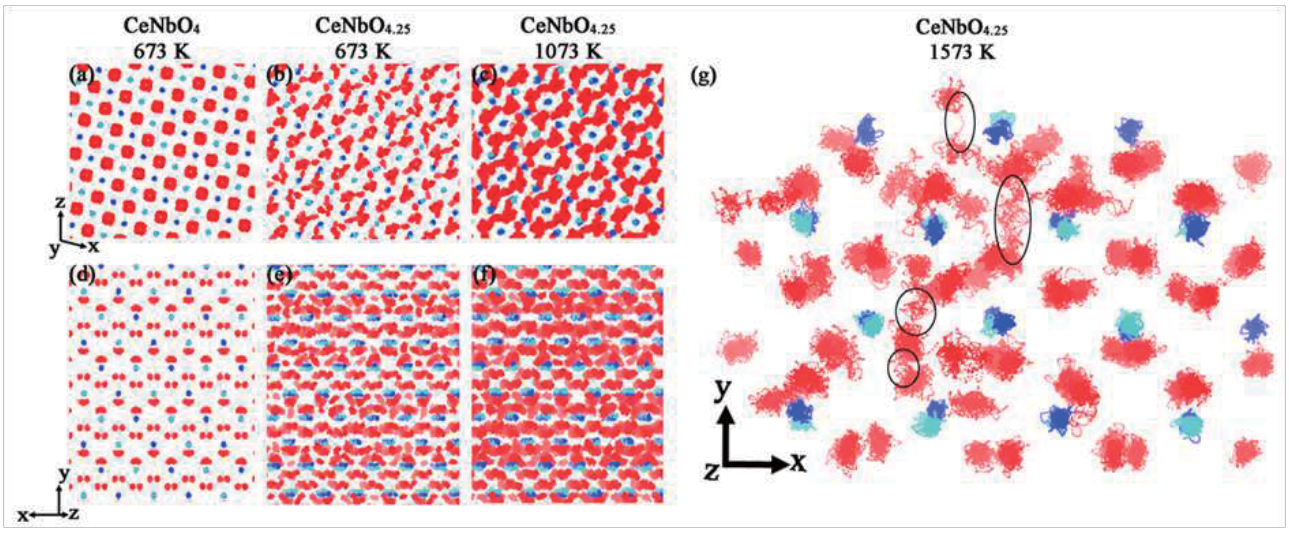


Figure 5.5: Oxygen diffusion trajectories over 100 ps captured in $CeNbO_4$ (a, d) at 673 K and $CeNbO_{4.25}$ (b, c, e, f) at 673 K and 1073 K. Local oxygen diffusion trajectories over 20 ps in $CeNbO_{4.25}$ at 1573 K are enlarged and shown in (g). The cyan, dark blue and red dots are representing $Ce^{3+/4+}$, Nb^{5+} and O^{2-} ions respectively. Oxygen diffusions in the x-z planes can be seen clearly. Occasional diffusions in y-direction are also observed (circled region).[4]

$CeNbO_{4.25}$ material is taken as shown in Fig. 5.5(g). This snapshot is taken from the simulation at 1573 K for 20 ps. The snapshot is taken for a shorter time to avoid too many diffusion trajectories which create a lot of noise in the figure. The higher temperature is used to allow faster diffusion and make sure completed oxygen hopping between oxygen sites can be captured in the short time-frame of 20 ps. In this snapshot, some oxygen hoppings in the y-direction (circled region in Fig. 5.5(g)) are seen in addition to oxygen diffusion along the x-z planes. The y-direction hopping happens around the NbO_7 and NbO_8 sites and corresponds to the channels formed by a series of NbO_7 and NbO_8 tetrahedra as revealed in the structure characterization by Pramana. This observation suggests that the oxygen diffusion in the $CeNbO_{4.25}$ is somewhat anisotropic. It would be very interesting to calculate and compare the hopping barriers of the x-z plane diffusion and the y-direction diffusion in further studies. Future material optimization efforts may focus on the editing of the NbO_7 and NbO_8 tetrahedra through appropriate doping.

The $CeNbO_{4.25}$ material has shown some anisotropic oxygen diffusion behaviours in Fig. 5.5(g). Other layered oxygen ion conductors, e.g. $La_2NiO_{4+\delta}$ and $PrBaCo_2O_{5+\delta}$, have shown similar anisotropic oxygen diffusion properties and are confirmed both experimentally and the-

oretically[15,19,48,141]. To further characterize the anisotropic oxygen diffusion phenomenon in $CeNbO_{4.25}$, its oxygen MSD data at 1573 K are analyzed and separated into component MSDs along the crystal's x, y and z directions respectively. The separated component MSDs and the total MSD are shown in Fig. 5.6. From the graph, it is clear that the oxygen diffusion is indeed anisotropic in the $CeNbO_{4.25}$ structure. The oxygen diffusion favours the x and z direction, but also happens in the y direction, which agrees with our previous observation from the local oxygen trajectories shown in Fig. 5.5. The x-direction diffusion is slightly faster than the z-direction diffusion according to the graph. This anisotropic diffusion is not as strong as the anisotropy observed in $La_2NiO_{4+\delta}$ though. In $La_2NiO_{4+\delta}$, only the oxygen ions in the La-O layers are involved in the oxygen diffusion process, while the oxygen ions in the perovskite layers are static. The y-direction diffusion in the $CeNbO_{4.25}$ structure may be enhancing the overall oxygen diffusion rate in the material.

As seen in Fig. 5.5, there seems to be a mobility difference between the oxygen ions at different locations. To understand the oxygen diffusion mechanism in the $CeNbO_{4.25}$ material better, it is of interest to check whether this intuitive observation is real. The minimum crystallographic cell of the $CeNbO_{4.25}$ material has 204 distinctive oxygen sites in total. The oxygen ions are labelled as O1 to O204 in the MD structure input. This input is enlarged to the standard input supercell which contains 19200 atoms in total. The oxygen ions in the enlarged supercell that share the same symmetric sites will have the same labels. This new input supercell is used to carry out a complete MD simulation at 1773 K. From this simulation, the oxygen MSD data and corresponding diffusion coefficients are calculated. The fastest oxygen ions sharing the same symmetric sites have an average diffusion coefficient of 18.05 cm^2s^{-1} while the slowest ones have an average diffusion coefficient of 1.40 cm^2s^{-1}. The range of diffusion coefficients between the fastest ones and the slowest ones is then divided into ten intervals. Each interval is one tenth of the whole diffusion coefficient range. The number of oxygen ions with diffusion coefficients falling into each interval is counted and summarized in Fig. 5.7. Combining the graph and the $CeNbO_{4.25}$ structural data, we find that the oxygen diffusion rate is not strongly dependent on the oxygen ion's symmetric sites. There is only one peak in the distribution graph shown in Fig. 5.7, and the oxygen diffusion coefficient corresponding to the peak is close to the

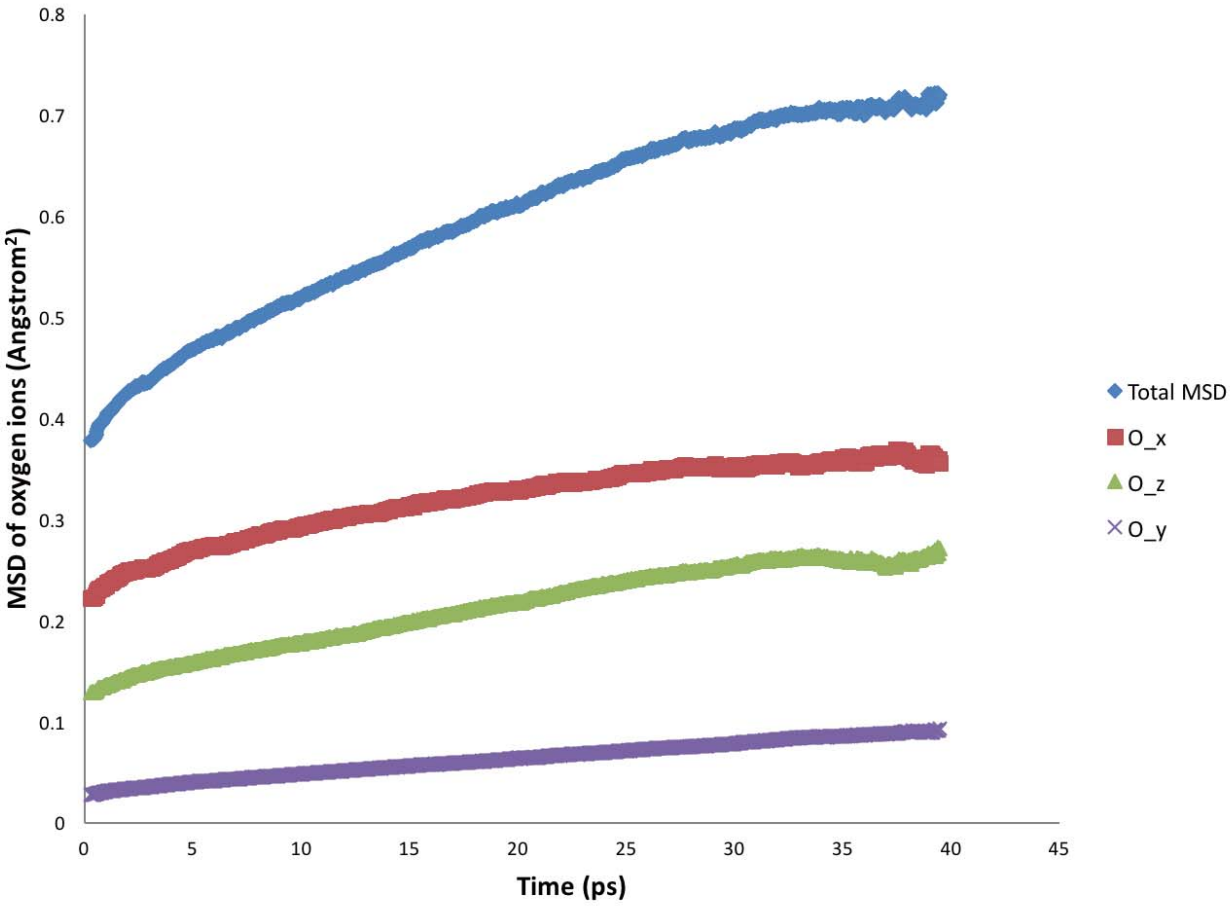


Figure 5.6: The MSDs of oxygen ions in $CeNbO_{4.25}$ at 1573 K separated into x, y and z directions are summarized together with the total oxygen MSD. The O_ x, O_ z and O_ y labels correspond to the oxygen MSD in x-direction, y-direction and z-direction respectively. Note that the angles between the x and z directions are about 105 ° and y-directon is perpendicular to the x-z plane. Please refer to Fig. 5.1 and Fig. 5.2 for illustration of the directions. The x and z directions The first 60 ps is still omitted and the starting 0 ps in this graph is the same time as the 60 ps in Fig. 5.3. The MSD data agrees with trajectory projections and shows the majority of oxygen diffusion is in the x-z plane. The diffusion in y-direction is not zero though.

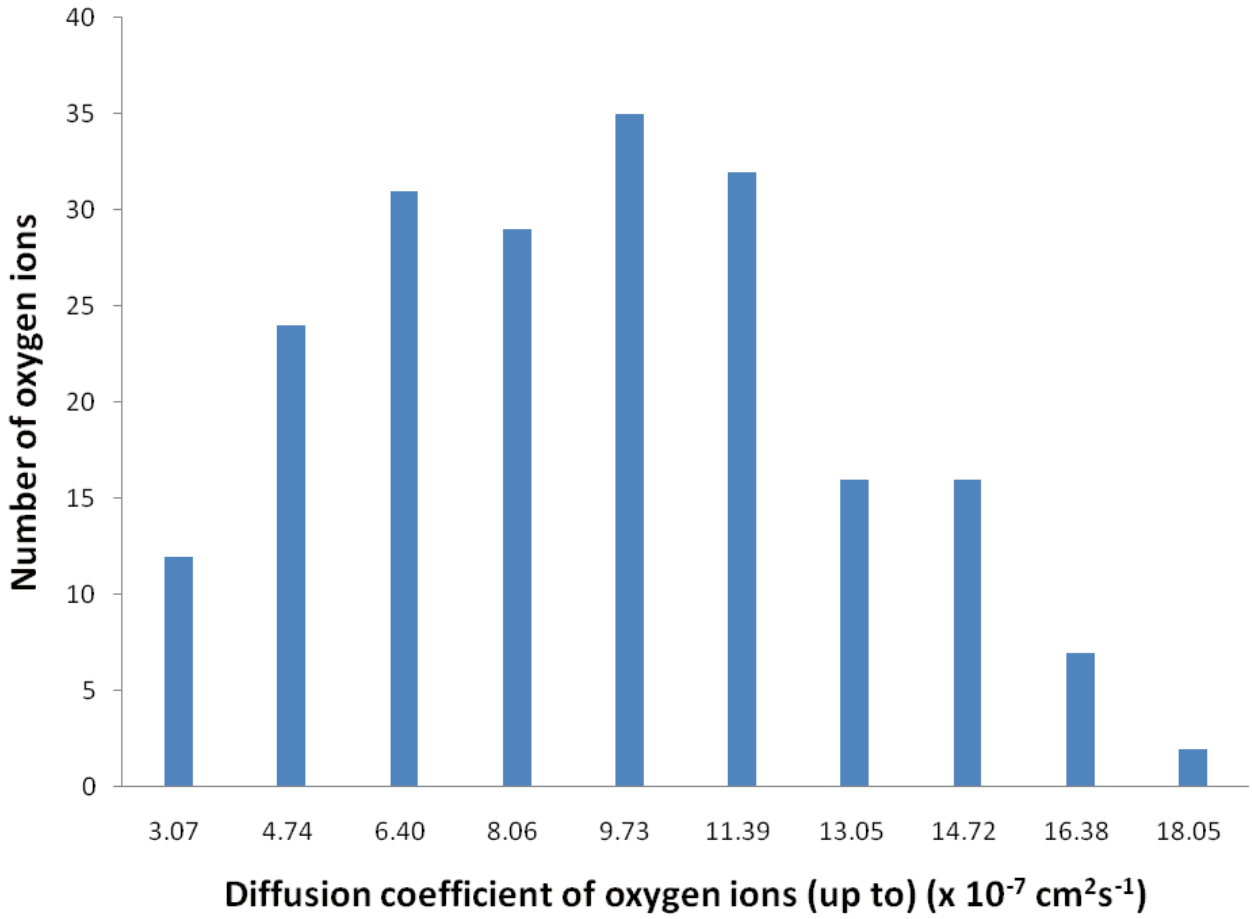


Figure 5.7: All the oxygen ions in the minimum cell of $CeNbO_{4.25}$ are labelled from O1 to O204. The distribution of the labelled oxygen ions' calculated diffusion coefficient in the enlarged $CeNbO_{4.25}$ supercell at 1773 K is summarized in this figure. The x-axis is starting from $1.40\times10^{-7}cm^2s^{-1}$ to $18.05\times10^{-7}cm^2s^{-1}$ and is evenly divided into 10 regions. Each of the bars represents the number of interstitial oxygen ions with diffusion coefficients inbetween the previous x-axis label and the current one. For example, the first bar shows the number of interstitial oxygen ions with diffusion coefficient inbetween $1.40\times\ 10^{-7}cm^2s^{-1}$ to $3.07\times\ 10^{-7}cm^2s^{-1}$. The distribution peak is quite close to the median of diffusion coefficients.

total average oxygen diffusion coefficient calculated earlier. Therefore, our intuitive observation in Fig. 5.5 is not true. It seems that the local environment around the oxygen ion does not significantly affect the oxygen ion's diffusion rate. The oxygen diffusion enhancement due to the inclusion of oxygen interstitials seems to be universal according to this calculation.

5.5 Conclusion

In this work, possible oxygen diffusions in both $CeNbO_4$ and $CeNbO_{4.25}$ are studied using MD simulations for a range of temperatures. This diffusion study is made possible with my colleague's identification of the exact oxygen interstitial sites and Ce^{3+}/Ce^{4+} sites. From the MD simulation results, we confirm that oxygen diffusion is only possible with oxygen interstitials in the $CeNbO_{4+\delta}$ system. The stoichiometric $CeNbO_4$ does not show any oxygen diffusion even at the high temperature of 1773 K. For the oxygen diffusion in the $CeNbO_{4.25}$ structure, three regions with different oxygen diffusion trends are identified. The transition region found starts at a temperature of about 1173 K, which is slightly higher than the phase transition temperature (1073 K) observed experimentally[127]. Although the oxygen diffusion activation energy calculated for the $CeNbO_{4+\delta}$ (0.86 eV) is comparable to the experimental value measured (0.99 eV) in the low temperature region, a few simulation results disagree with experimental findings. The experimental diffusion coefficients of oxygen are systematically higher than the values calculated from the simulations. This indicates that there is some diffusion mechanism which may be independent of the temperatures. Above the transition temperature region, experiments show a big drop of oxygen diffusion rate while our simulations give an increased oxygen diffusion coefficient. We believe that this is mainly due to the oxygen loss and phase change of the $CeNbO_{4.25}$ in experiments, which cannot happen in the simulation time-frame. If the $CeNbO_{4.25}$ phase can be stabilized and maintained at higher temperature, it may give much better performance.

In addition, oxygen diffusion pathways are revealed through the visualization of oxygen diffusion trajectories. The oxygen ions are hopping to the interstitial sites during diffusion. The channel formed by the NbO_7 and NbO_8 tetrahedra between the x-z planes provides additional oxygen diffusion pathways across the layers. This may enhance the overall oxygen diffusion rate. Anisotropic oxygen diffusion is confirmed through both diffusion trajectories and separation of directional component MSD data. The diffusion anisotropy is weaker than in other layered complex oxides like $La_2NiO_{4+\delta}$, where only the oxygen ions in the La-O layers are relevant to the oxygen diffusion process. The distribution of the oxygen diffusion coefficient with respect to

unique symmetric oxygen sites is calculated and analyzed. The result is similar to a Gaussian distribution and does not indicate any significant relationship between the oxygen diffusion rate and its corresponding local environment.

In summary, the oxygen diffusion mechanism in $CeNbO_{4+\delta}$ is very interesting and unique to a certain extent. Part of the oxygen diffusion mechanism has been revealed by this study, and these results provide new insights into the oxygen diffusion behaviour of anisotropic layered oxygen conductors. However, there are still open questions like the reason behind the faster oxygen diffusion observed at low temperature. There is very limited literature on the oxygen diffusion in $CeNbO_{4+\delta}$ for comparison to date, as this material is still relatively new. To fully elucidate the oxygen diffusion mechanism and utilize the material's potential, further experimental and theoretical studies, e.g. structure analysis of the $CeNbO_{4.08}$ and $CeNbO_{4.33}$ phase and related Ab Initio simulations, are certainly needed.

Chapter 6

Summary and Further Work

In this thesis, classical thermodynamics and atomistic simulation methods have been employed to investigate the La-Ni-O Ruddlesden-Popper and $CeNbO_{4+\delta}$ Fergusonite systems. A number of interesting questions and phenomena related to these materials have been evaluated. Specifically, a newly observed La-rich termination on the $La_2NiO_{4+\delta}$ material[1–3] and the origin of this termination has been investigated using classical thermodynamics in conjunction with Ab Initio simulation methods. The $CeNbO_{4+\delta}$ Fergusonite systems, as a potential candidate to be a novel ionic conductor, has been studied using molecular dynamics simulation to learn its oxygen diffusion mechanism for the first time.

6.1 $La_2NiO_{4+\delta}$ Ruddlesden-Popper materials

6.1.1 La_2NiO_4 surface energy

To investigate the La-rich termination on the $La_2NiO_{4+\delta}$ material, we started by evaluating the surface energies of the ideal La_2NiO_4 material's various possible surface terminations. There has been only one study on the surface energies of the La_2NiO_4 material in the literature and it is done by Read *et al.*[20]. Read calculated the surface energies of the material's low-lying orientations using static atomistic simulations based on classical pair potentials. Their

results suggested that the La_2NiO_4 material's stable terminations, depending on the orientation, should exhibit only Ni atoms or a mixture of La and Ni atoms. However, classical pair potential simulation has some limitations. The pair potentials are partly fitted to experiments and are ionic potentials. These potentials may not be able to fully capture the electronic effects like local polarisation. Therefore, we decided to use DFT to re-evaluate the La_2NiO_4 material's surface energies. The DFT method is an electronic structure method and can reproduce local polarisation effects much better than classical pair potentials.

Our initial analysis of the La_2NiO_4 material's possible surface terminations suggests that only some of the (001) surfaces may present La-only terminations, while the (010) or (100) surfaces will always present mixed La-Ni terminations. Therefore, our surface energies calculations focus on the (001) La_2NiO_4 terminations to check whether the La-only termination is possible or not. As discussed in chapter 3, there is only one Tasker's Type 2 surface among three possible La_2NiO_4 (001) terminations. This surface is labelled as the LaO surface. The other two surfaces, labelled as NiO2 and LaOOLa surfaces, always come together if unit cell stoichiometry is maintained. These two terminations will give a Tasker's Type 3 surface with dipole moments.

Before the calculation of the surface energies, there are some computational details that need to be confirmed as detailed in chapter 3 and 4. Due to the presence of the strongly correlated La atoms in the La_2NiO_4 material, the hybrid DFT method, which gives a better description of the strongly correlated atoms, is used. The La basis sets are further optimised to include a more diffuse f-orbital using La_2NiO_4 structural relaxation calculations. The structural relaxation calculations of the La_2NiO_4, $La_3Ni_2O_7$ and $La_4Ni_3O_{10}$ materials indeed show systematic improvements with the optimised La basis sets when comparing to the literature La basis sets, as discussed in chapter 2. Therefore, the new La basis sets are used throughout this work. As spin-polarised Ni is present in La-Ni-O Ruddlesden-Popper materials, the magnetic ordering used in the simulations is also discussed in chapter 4. Our results show that the most stable Ni magnetic ordering is the g-type anti-ferromagnetic ordering, which agrees with literature neutron scattering experimental results. In addition, our results show that the correct anti-ferromagnetic Ni magnetic ordering stabilizes the La_2NiO_4 material compared to no magnetic ordering or ferromagnetic ordering. Therefore, proper simulations of these materials should

always include the magnetic effects to ensure reliability.

By comparing the calculated surface energies of the NiO2, LaOOLa and LaO terminations, we show that the LaO surface is the most stable (001) La_2NiO_4 surface. This is different from what Read suggested in his pair potential simulation results[20]. We believe that the difference is mainly due to fact that the electron distribution and polarisation effects are not fully described by the pair potentials used by Read. In this work, we have only done a very quick check of the electronic densities of the simulation results and some electron polarisation is already observed. As the details of the electron distribution and related effect may have a strong impact on our understanding of these materials, it is very important to carry out detailed analysis of the electron densities and band structures in future work. Analysis methods like Mulliken charge analysis and projected density of states can give more detail on the degree of polarisation and serve as the basis for further investigation of the oxygen catalysis mechanism on La terminated surfaces.

6.1.2 $La_2NiO_{4+\delta}$ surface stability

As mentioned previously, our results suggest that the La_2NiO_4 material's La-terminated (001) surface is the most stable (001) surface. This result can partly explains the observed La-rich termination. However, the La-rich surface is also observed on a polycrystalline $La_2NiO_{4+\delta}$ sample. The ideal surface energies alone cannot explain this phenomenon. Inspired by Gauquelin's long-term heating experiments[90], we propose that the La-rich termination may be caused by the partial decomposition of $La_2NiO_{4+\delta}$. This partial decomposition can yield La_2O_3 and may be covering the $La_2NiO_{4+\delta}$. Thus, this La_2O_3 layer will show a La-rich termination on all surface orientations.

To validate this hypothesis, the thermodynamic stability of La_2NiO_4 is studied with respect to its higher order cousins, $La_3Ni_2O_7$, $La_4Ni_3O_{10}$ and $LaNiO_3$ in chapter 3. The Gibbs reaction energies of the decomposition of La_2NiO_4 into $La_3Ni_2O_7$, $La_4Ni_3O_{10}$ and $LaNiO_3$ with the side product La_2O_3 are calculated using literature experimentally-fitted thermodynamic parameters. The calculated Gibbs reaction energies of these reactions are exothermic up to about 1400 K at

0.2 bar oxygen partial pressure. The decomposition into $LaNiO_3$ is less favourable than the other two possible decomposition reactions. At temperatures below 1000K, $La_3Ni_2O_7$ will be formed, while at higher temperature, the formation of $La_4Ni_3O_{10}$ is more favourable. These results are very interesting, as the proposed working temperature of the intermediate temperature SOFC is just around 873 K to 1073 K. Depending on the exact working conditions, a mixture of these two materials may be formed in experiments. This also agrees with Gauquelin's results that both $La_3Ni_2O_7$ and $La_4Ni_3O_{10}$ are observed. For the decompositions into $La_3Ni_2O_7$ and $La_4Ni_3O_{10}$, the effect of oxygen partial pressure is also investigated by plotting the change in Gibbs reaction energy against both temperature and oxygen partial pressure. The results show that both reactions will stop if the oxygen partial pressure is very low. Under pure oxygen atmosphere, both decompositions are able to proceed at temperatures higher than 1400 K.

Usually, the $La_2NiO_{4+\delta}$ material is not ideal in experiments. This material is able to take extra oxygen atoms up to $\delta = 0.25$. Unlike $La_2NiO_{4+\delta}$, the higher ordered $La_3Ni_2O_7$ and $La_4Ni_3O_{10}$ structures are commonly found to be oxygen deficient. To include the effects of the oxygen defects in our thermodynamic studies, first principle calculations of oxygen defect energies are used to approximate the room temperature phenomena. The materials with the highest oxygen defect δ values are used as simulation inputs to represent the extreme cases. By examining the extreme cases, the range of change in Gibbs reaction energies may be roughly defined. The defective decomposition reaction discussed in chapter 3 are as follows

$$4La_2NiO_{4.25} \rightarrow 2La_3Ni_2O_7 + La_2O_3 \tag{6.1}$$

$$4La_2NiO_4 + \frac{1}{4}O_2 \rightarrow 2La_3Ni_2O_{6.75} + La_2O_3 \tag{6.2}$$

$$3La_2NiO_{4.25} + \frac{1}{8}O_2 \rightarrow La_4Ni_3O_{10} + La_2O_3 \tag{6.3}$$

$$3La_2NiO_4 + \frac{1}{4}O_2 \rightarrow La_4Ni_3O_{9.5} + La_2O_3 \tag{6.4}$$

These four reactions can be divided into two categories; reactions under oxidizing environments (containing $La_2NiO_{4.25}$) and reactions under reducing environments (containing $La_3Ni_2O_{6.75}$ or $La_4Ni_3O_{9.5}$). By incorporating DFT based oxygen defect energies into the Gibbs reaction energies of these reactions, the estimated Gibbs reaction energies are plotted together with

the ideal cases' Gibbs reaction energies in Fig. 3.8 and 3.9. These graphs show that the reactions under oxidizing environments are even more exothermic than the ideal cases. This is particularly relevant to real applications as the SOFC cathodes are usually in a slightly oxidizing environment. Under reducing environments, our simulation results show some shifts of the reactions curves, but the decomposition reactions are still favourable for temperatures lower than 800 K. It is important to remember that these results are approximated using 0 K defect formation energies and are only indicative. More rigorous calculations should be conducted to give quantitative predictions of the decompositions.

The ordering of the layered structure produced by the decomposition is suggested to be La_2O_3 - $La_3Ni_2O_7$ and/or $La_4Ni_3O_{10}$ - La_2NiO_4 (from surface to bulk). This ordering is believed to have minimal lattice mismatches and is most stable. The interfacial energies between these layers, however, are not calculated yet and is certainly a future topic to confirm the stability of this ordering. Powerful high-resolution surface characterisation techniques, such as transmission electron microscopy (TEM) and surface X-ray crystal truncation rod method, can also give the $La_2NiO_{4+\delta}$ surface structures directly. These experiments should provide very strong evidence and are crucial to confirming our hypothesis.

It is known that many experimental conditions of the $La_2NiO_{4+\delta}$ material's performance tests in the literature fall in the favourable range of our proposed decompositions. Therefore, our results suggest that oxygen reduction is likely to take place on the reformed $La_2NiO_{4+\delta}$ surfaces instead of exposed Ni sites. Still, these experiments show that this material is not bad as a SOFC cathode. The traditional view of the oxygen surface reduction requires a clearly-defined transition metal which is able to donate electrons and change its own oxidation state. In this case, it may be a new kind of oxygen reduction reaction that does not strictly require a transition metal to be involved. It is therefore very interesting to conduct more theoretical studies to explore how the oxygen reduction and incorporation works on these reformed surfaces. Possible studies may include first principle simulation of the oxygen reduction process on the La terminated surface. These studies may create new fronts in the field of surface catalysis.

Due to time constraints, our simulations focus on the surface termination and reconstruction

of the La-Ni-O Ruddlesden-Popper (RP) systems in this thesis. As mentioned in chapter 3, the A-site terminations and reconstructions are not limited to the La-Ni-O system. Similar phenomena have been observed on a number of perovskite and RP systems with the A-site being other Lanthanides, e.g. Pr in Pr_2NiO_4, and alkaline metals, e.g. Sr in $SrTiO_3$[1–3]. Among the Ln_2NiO_4-type materials exhibiting A-site enriched surfaces, the Pr_2NiO_4 material currently gives the best experimental performance[86]. Therefore, further studies on the Pr_2NiO_4 surface have important practical implications. These studies may suggest new ways to improve the best known Ruddlesden-Popper material's performance. Comparing the results from the study of the Pr_2NiO_4 material and the La_2NiO_4 material will also further our understanding on the series of Ln_2NiO_4-type Ruddlesden-Popper material and identify possible new MIEC materials.

6.1.3 La vacancy in $La_2NiO_{4+\delta}$

In chapter 3, we showed that a decomposition of the $La_2NiO_{4+\delta}$ material is thermodynamically favourable and may be the cause of the La-terminated surfaces observed in the experiments. In reality, only the surfaces of the $La_2NiO_{4+\delta}$ materials decompose and the bulk materials remain stable. Certainly, some factors are preventing the complete decomposition of the $La_2NiO_{4+\delta}$ materials. A very slow reaction step may be sufficient to limit the decomposition in the surface layers. During the transformation from $La_2NiO_{4+\delta}$ to the higher order $La_3Ni_2O_7$ and/or $La_4Ni_3O_{10}$, a LaO layer must be leaving and possibly moving to the top of the surface. As the oxygen in the $La_2NiO_{4+\delta}$ material's LaO layer is known to be mobile, we suggest that the La migration may be the slowest step of the decomposition reaction.

There have been reports of La vacancies in the La_2NiO_4 materials[142]. The presence of a La vacancy would certainly help the diffusion of La in La_2NiO_4. Therefore, we start our investigation by examining the La vacancy formation energy in La_2NiO_4. The calculation of the La vacancy formation energy requires the lattice energy of the stoichiometric phase, the lattice energy of the defective phase and related La chemical potential, as shown in Eqn. 4.3. The lattice energies can be directly calculated using hybrid DFT methods, but the La chemical potential range must be indirectly estimated due to the limitations of the hybrid

density functionals. The La chemical potential range is estimated using the experimental Gibbs formation energy of La_2O_3 and calculated oxygen chemical potential as detailed in chapter 4. For the calculation of defective La_2NiO_4's lattice energy, the $La_{1.875}NiO_4$ cell is used by removing one La atom from a $2 \times 1 \times 1$ La_2NiO_4 supercell. The La vacancy formation energy in La_2NiO_4 is then calculated to be in the range of -2.14 eV to 8.78 eV per La defect. There is no literature data available for a direct comparison to our results. Instead, we compare the La vacancy formation energy calculated to a literature oxygen interstitial formation energy calculated in La_2NiO_4. The oxygen interstitial formation energy calculated by Minervini is -6.63 eV per defect and is significantly lower than our calculated La vacancy energy. This large difference is expected as La atoms are not spontaneously leaving the La_2NiO_4 in experiments. On the other hand, it is very easy for La_2NiO_4 to absorb oxygen atoms when it is exposed to air.

The La vacancy migration barrier is then calculated using hybrid DFT assuming the presence of a La vacancy. The input cells used are the same as for the defective $La_{1.875}NiO_4$ cell used previously, except that the location of the La vacany is moved to represent different starting and ending structures of the La diffusion process. Although all the La vacancy sites are symmetrically equivalent and it will give the same total defective lattice energy no matter where the vacancy locates, the La diffusion processes are actually different depending on which layer it is moving through. The La can be moving through either the rock-salt like LaO layer or the perovskite like $LaNiO_3$ layer. Therefore, the activation barriers of both diffusion steps are calcualted using the Distinguished Reaction Coordinates method. Our results give an activation energy of 4.31 eV for the rock-salt layer and 4.57 eV for the perovskite layer. Again, as these processes are evaluated for the first time, no literature result is available to compare. There has been work on La diffusion in a similar perovskite material $LaCrO_3$ and they obtain a La diffusion barrier of 4.98 eV in this material[110]. The $LaCrO_3$ material has a similar structure to our $LaNiO_3$ layer and our diffusion energy for the $LaNiO_3$ layer is larger but still comparable to the La diffusion barrier in $LaCrO_3$. Our La diffusion activation energy is also compared to the oxygen interstitial diffusion activation energy in $La_2NiO_{4+\delta}$ (0.88 eV[15]). The La diffusion activation energy calculated is about five times of the oxygen diffusion energy. Using the Arrhenius equation, we estimate that the La diffusion in La_2NiO_4 is at least 3 orders of magnitudes slower

than the oxygen diffusion in the same material. These results support our hypothesis that the decomposition of La_2NiO_4 is limited by the very slow rate determining step. It is still possible for the La atom to move through the first few layers of La_2NiO_4 and form extra La_2O_3 on top, but the bulk material is unlikely to completely decompose.

There are several aspects related to La diffusion which are not considered in this thesis. In our work, only the La vacancy migration through bulk atomic layers is examined. The bulk migration barrier can be different from the La diffusion barrier close to the surface due to surface reconstructions and strain effects. Lee *et al.* has reported that the AO (LaO or SrO) and BO (TiO or NiO) atomic layer swaps during the growth of Sr_2TiO_4 and La_2NiO_4 thin films on the $SrTiO_3$ substrates[143]. Their observation results in a layered structure that is very similar to what we propose. In such a slab-like setup, it is important to know which layer is the most difficult one for the atoms to move through and how the diffusions lead to the layer-swapping observed. As such slab-like structures resemble thin-film growth condition, simulation works on the La diffusion in the slabs may provide insights to explain the thin-film layer swapping observed in the experiments. Knowing the possible swapping/diffusion mechanisms under the slab conditions may suggest ways to control thin-film growth and engineer the thin-film Ruddlesden-Popper-type materials. Besides the surface effects, grain boundary diffusion of La is also important but not examined in this thesis. This kind of diffusion is probably the fastest route for the La atoms to reach exposed surfaces in a poly-crystalline sample. As grain boundaries are very common in the experimental samples and devices, the evaluation of the grain boundary diffusion's impact will be very relevant to the practical application of the $La_2NiO_{4+\delta}$ material. Since the number of atoms required to properly reproduce a grain boundary is usually large, this kind of theoretical study may require a combination of simulation techniques (or multi-scale simulations) to reach reasonable results within a sensible time-frame. Last but not least, there has been reports of intrinsic A-site vacancies in materials like Nd_2NiO_4[144]. As this material is reported to exhibit better performance as a SOFC cathode compared to $La_2NiO_{4+\delta}$, it will be very interesting to explore the vacancy formation and possible Nd diffusion in this similarly structured Nd_2NiO_4 material. It will be very useful to understand whether similar decomposition happens in Nd_2NiO_4 and how it may affect this material's performance.

6.2 $CeNbO_{4+\delta}$ Fergusonite material

The $CeNbO_{4+\delta}$ Fergusonite material is an interesting material that exhibits quite high oxygen diffusion without any aliovalent doping[121–124]. This material can adopt four possible phases with different amounts of oxygen interstitials with δ = 0, 0.08, 0.25 and 0.33[125,126]. Similar to the $La_2NiO_{4+\delta}$ material studied in the previous chapters, oxygen diffusion in $CeNbO_{4+\delta}$ is believed to be related to the oxygen interstitials. Computational studies of possible interstitial diffusion pathways in $CeNbO_{4+\delta}$ materials have not been possible in the past as the structures of the oxygen-rich $CeNbO_{4+\delta}$ phases were not solved. Recently, my colleagues grew single crystal $CeNbO_{4.25}$ and successfully solved the $CeNbO_{4.25}$ structure using the single crystal samples. This finding allows for oxygen diffusion simulation in the $CeNbO_{4+\delta}$ materials for the first time. As the $CeNbO_{4.25}$ has a modulated structure and a very large primitive unit cell (300 atoms), it is very computationally expensive to conduct First Principle simulations on this material. Instead, we used pair potential based molecular dynamics simulations to investigate oxygen diffusions (if any) in the $CeNbO_4$ and $CeNbO_{4.25}$ materials.

Currently, no pair potentials are specifically derived for the $CeNbO_{4+\delta}$ materials. Therefore, some literature Ce^{3+} - O^{2-}, Ce^{4+} - O^{2-}, Nb^{5+} - O^{2-} and O^{2-} - O^{2-} pair potentials are taken from studies on the Ce-Metal-O systems. Two slightly different sets of pair potentials are formulated and tested using the 0 K relaxations of experimental $CeNbO_4$ and $CeNbO_{4.25}$ primitive unit cells as detailed in chapter 5. The results show that neither of the two potential sets is systematically better than the other set. This suggests that both potential sets are somewhat universal for the Ce-Metal-O systems. For molecular dynamics simulations in this work, the pair potential set A as noted in section 5.3 is used.

Molecular dynamics simulations have been done on the $CeNbO_4$ and $CeNbO_{4.25}$ materials. The input super cells are designed to contain 19200 atoms for both $CeNbO_4$ and $CeNbO_{4.25}$. The mean-squared displacements of the oxygen ions calculated for these two materials are plotted against diffusion time at various temperature up to 1773 K and compared. These results clearly show that there is no evidence of oxygen diffusion for ideal $CeNbO_4$ even up to a temperature of 1773 K, while the $CeNbO_{4.25}$ displays oxygen diffusion in the same temperature range. This

comparison confirms that the presence of oxygen interstitials is required for oxygen diffusion in the $CeNbO_{4+\delta}$ materials. The oxygen diffusion coefficients are calculated from the $CeNbO_{4.25}$ MSD results and plotted against temperature. This plot shows three regions with different oxygen diffusion behaviours. The oxygen diffusion activation energies for each of the regions are calculated assuming an Arrhenius relationship. For the lower temperature region, the calculated oxygen diffusion activation energy (0.86 eV) is comparable to the experimental value measured (0.99 eV) for the $CeNbO_{4.25}$ material[124]. However, the experimental oxygen diffusion coefficients in the lower temperature range are systematically higher than our calculated values. This suggests that the MD simulations are not replicating all the experimental behaviours. There may be some other undiscovered diffusion mechanisms which are independent of the temperatures. For the higher temperature region, the experimental oxygen diffusion coefficients drop significantly due to the loss of interstitial oxygen and related phase change. In the time frame probed by the MD simulations, the loss of interstitial oxygen and phase changes are not able to complete. It is not a surprise that the simulation results in the higher temperature region is different from experimental values. However, the simulation results also show a transition region (at about 1173 K) in the oxygen diffusion coefficient graph. One possible explanation is that this transition region may represent the activation of a new diffusion pathway, but we do not have any strong evidence to confirm this yet. This transition region found in the oxygen diffusion coefficients graph certainly needs to be examined further with both experimental and theoretical efforts to understand its origin. It may be revealing something new or just simply caused by the limitations of the simulation methods. If the simulation results at the higher temperature region truly reflect some reality, the $CeNbO_{4.25}$ phase may give much better performance when it is stabilized at these temperatures.

Some snapshots of the oxygen diffusion trajectories have been taken for the $CeNbO_{4.25}$ simulations. These trajectories show that the oxygen ions are diffusing mainly along the x-z planes with occasional hopping between the x-z planes. This partial diffusion anisotropy is later confirmed by analyzing the oxygen MSD data separated into different component directions. Unlike the strongly anisotropic diffusion observed in the $La_2NiO_{4+\delta}$ materials, direction-preferential oxygen diffusions in the $CeNbO_{4.25}$ is not very significant. The trajectory snapshots also reveal

that the diffusion pathways between the x-z planes are located at the NbO_7 and NbO_8 tetrahedra. This is an unique character of the $CeNbO_{4.25}$ modulated structure. Different unique symmetric oxygen sites are labelled to calculate average oxygen diffusion coefficients with respect to the sites. The distribution of the resulting oxygen diffusion coefficients is similar to a Gaussian distribution and does not seem to suggest any link between the oxygen diffusion coefficient and the oxygen's location.

As mentioned in chapter 5, the lack of clearly solved crystal structures deterred meaningful computational studies of the $CeNbO_{4+\delta}$ materials. So far, only the $CeNbO_{4.25}$ structure has been solved and simulated in this study. The other two oxygen rich $CeNbO_{4+\delta}$ phases, the $CeNbO_{4.08}$ and $CeNbO_{4.33}$, are still not solved yet. Any future experimental structural analysis would certainly benefit our understandings of the $CeNbO_{4+\delta}$ materials. Several questions regarding the oxygen diffusion in the $CeNbO_{4.25}$ arise in our simulations and many of them seem to be related to the oxygen interstitials movement during possible phase changes. Therefore, any comparisons between simulation results of the $CeNbO_{4.25}$ material and the $CeNbO_{4.08}$/ $CeNbO_{4.33}$ materials will be very helpful to reveal how the oxygen interstitials adapt between these different phases and affect oxygen diffusion. Our simulations of the $CeNbO_{4.25}$ may also be limited by the pair potential simulation methods, as the pair potential method may not capture electronic properties. First principle studies of the $CeNbO_{4+\delta}$ family, although computationally expensive, may tell more about the details of these materials.

Bibliography

[1] M. Burriel, S. Wilkins, J. P. Hill, M. a. Muñoz Márquez, H. H. Brongersma, J. a. Kilner, M. P. Ryan and S. J. Skinner, *Energy Environ. Sci.*, 2014, **7**, 311.

[2] J. Druce, T. Ishihara and J. Kilner, *Solid State Ionics*, 2014, **262**, 893–896.

[3] J. Druce, H. Téllez, M. Burriel, M. D. Sharp, L. J. Fawcett, S. N. Cook, D. S. McPhail, T. Ishihara, H. H. Brongersma and J. A. Kilner, *Energy Environ. Sci.*, 2014, **7**, 3593–3599.

[4] S. S. Pramana, T. Baikie, T. An, M. G. Tucker, J. Wu, M. K. Schreyer, F. Wei, R. D. Bayliss, C. L. Kloc, T. J. White, A. P. Horsfield and S. J. Skinner, *J. Am. Chem. Soc.*, 2016, **138**, 1273–1279.

[5] M. L. Pachauri R. K., *IPCC 2014, Climate Change 2014: Synthesis Report. Contribution of Working Groups I, II and III to the Fifth Assessment Report of the Intergovernmental Panel on Climate Change*, Intergovernmental panel on climate change (ipcc) technical report, 2014.

[6] G. Thomas, *Overview of Storage Development DOE Hydrogen Program*, Us doe hydrogen program 2000 annual review technical report, 2000.

[7] M. Ni, M. K. H. Leung and D. Y. C. Leung, *International Journal of Hydrogen Energy*, 2008, **33**, 2337–2354.

[8] R. O'Hayre, S.-W. Cha, W. Colella and F. B. Prinz, *Fuel Cell Fundamentals*, John Wiley & Sons, 2006.

[9] *Fuel Cell Science and Engineering*, ed. D. Stolten and B. Emonts, Wiley-VCH Verlag GmbH & Co. KGaA, Weinheim, Germany, 2012.

[10] G. Amow and S. J. Skinner, *J. Solid State Electrochem.*, 2006, **10**, 538–546.

[11] B. Steele, *Solid State Ionics*, 2000, **129**, 95–110.

[12] V. V. Kharton, A. P. Viskup, E. N. Naumovich and F. M. B. Marques, *J. Mater. Chem.*, 1999, **9**, 2623–2629.

[13] V. Kharton, A. P. Viskup, A. Kovalevsky, E. Naumovich and F. Marques, *Solid State Ionics*, 2001, **143**, 337–353.

[14] S. J. Skinner and J. A. Kilner, *Solid State Ionics*, 2000, **135**, 709–712.

[15] J. Bassat, P. Odier, A. Villesuzanne, C. Marin and M. Pouchard, *Solid State Ionics*, 2004, **167**, 341–347.

[16] J. Jorgensen, B. Dabrowski, S. Pei, D. Richards and D. Hinks, *Phys. Rev. B*, 1989, **40**, 2187–2199.

[17] J. Rodriguez-Carvajal, M. T. Fernandez-Diaz and J. L. Martinez, *J. Phys. Condens. Matter*, 1991, **3**, 3215–3234.

[18] J. Kilner and C. Shaw, *Solid State Ionics*, 2002, **154-155**, 523–527.

[19] A. Chroneos, D. Parfitt, J. a. Kilner and R. W. Grimes, *J. Mater. Chem.*, 2010, **20**, 266.

[20] M. S. D. Read, M. S. Islam, G. W. Watson and F. E. Hancock, *J. Mater. Chem.*, 2001, **11**, 2597–2602.

[21] G. Lander, P. Brown, J. Spal/ek and J. Honig, *Phys. Rev. B*, 1989, **40**, 4463–4471.

[22] M. Medarde and J. Rodríguez-Carvajal, *Zeitschrift f Phys. B Condens. Matter*, 1997, **102**, 307–315.

[23] A. Mehta and P. Heaney, *Phys. Rev. B*, 1994, **49**, 563–571.

[24] Y. Takeda, R. Kanno, M. Sakano, O. Yamamoto, M. Takano, Y. Bando, H. Akinaga, K. Takita and J. Goodenough, *Mater. Res. Bull.*, 1990, **25**, 293–306.

[25] E. a. Kiselev, N. V. Proskurnina, V. I. Voronin and V. a. Cherepanov, *Inorg. Mater.*, 2007, **43**, 167–175.

[26] C.-Y. Shi, Z.-B. Hu and Y.-M. Hao, *J. Alloys Compd.*, 2011, **509**, 1333–1337.

[27] S. J. Skinner, *Solid State Sci.*, 2003, **5**, 419–426.

[28] T. Brill, G. Hampel, F. Mertens, R. Schürmann, W. Assmus and B. Lüthi, *Phys. Rev. B*, 1991, **43**, 10548–10554.

[29] K. Nakajima, Y. Endoh, S. Hosoya, J. Wada, D. Welz, H.-M. Mayer, H.-A. Graf and M. Steiner, *J. Phys. Soc. Japan*, 1997, **66**, 809–817.

[30] E. Iguchi, H. Satoh, H. Nakatsugawa and F. Munakata, *Phys. B Condens. Matter*, 1999, **270**, 332–340.

[31] G. W. Guo and W. M. Temmerman, *Journal of Physics C: Solid State Physics*, 1988, **21**, L803.

[32] G. Aeppli and D. Buttrey, *Phys. Rev. Lett.*, 1988, **61**, 203–206.

[33] D. Góra and K. Parliki, *J. Magn. Magn. Mater.*, 2003, **257**, 235–238.

[34] S. Itoh, K. Yamada, M. Arai, Y. Endoh, Y. Hidaka and S. Hosoya, *J. Phys. Soc. Japan*, 1994, **63**, 4542–4549.

[35] K. Nakajima, K. Yamada, S. Hosoya, Y. Endoh, M. Greven and R. J. Birgeneau, *Zeitschrift fr Physik B Condensed Matter*, 1995, **96**, 479–489.

[36] P. Kuiper, J. van Elp, G. Sawatzky, A. Fujimori, S. Hosoya and D. de Leeuw, *Phys. Rev. B*, 1991, **44**, 4570–4575.

[37] P. Kuiper, D. Rice, D. Buttrey, H.-J. Lin and C. Chen, *Phys. B Condens. Matter*, 1995, **208-209**, 271–272.

[38] P. Odier, Y. Nigara, J. Coutures and M. Sayer, *J. Solid State Chem.*, 1985, **56**, 32–40.

[39] V. Anisimov, D. Bukhvalov and T. Rice, *Phys. Rev. B*, 1999, **59**, 7901–7906.

[40] M. A. Daroukh, V. V. Vashook, H. Ullmann, F. Tietz and I. A. Raj, *Solid State Ionics*, 2003, **158**, 141–150.

[41] A. Aguadero, J. A. Alonso, M. J. Mart?nez-Lope, M. T. Fern?ndez-D?az, M. J. Escudero and L. Daza, *J. Mater. Chem.*, 2006, **16**, 3402.

[42] E. Boehm, J.-M. Bassat, M. Steil, P. Dordor, F. Mauvy and J.-C. Grenier, *Solid State Sci.*, 2003, **5**, 973–981.

[43] S. Tajima, M. Seki, Y. Hidaka, K. Oka, H. Unoki, M. Suzuki, S. Suga, H. Ishii, T. Nakahashi, T. Murakami, T. Takagi and S. Uchida, *Journal of the Optical Society of America B*, 1989, **6**, 475.

[44] A. Cleave, J. Kilner, S. Skinner, S. Murphy and R. Grimes, *Solid State Ionics*, 2008, **179**, 823–826.

[45] E. Naumovich and V. Kharton, *J. Mol. Struct. THEOCHEM*, 2010, **946**, 57–64.

[46] N. L. Allan, J. M. Lawton and W. C. Mackrodt, *Philos. Mag. Part B*, 1989, **59**, 191–206.

[47] A. Chroneos, B. Yildiz, A. Tarancón, D. Parfitt and J. A. Kilner, *Energy & Environmental Science*, 2011, **4**, 2774.

[48] L. Minervini, R. W. Grimes, J. a. Kilner and K. E. Sickafus, *J. Mater. Chem.*, 2000, **10**, 2349–2354.

[49] C. Frayret, A. Villesuzanne and M. Pouchard, *Chem. Mater.*, 2005, **17**, 6538–6544.

[50] M. S. D. Read, M. S. Islam, F. King and F. E. Hancock, *J. Phys. Chem. B*, 1999, **103**, 1558–1562.

[51] D. Prabhakaran, P. Isla and A. Boothroyd, *J. Cryst. Growth*, 2002, **237-239**, 815–819.

[52] F. Kröger and H. Vink, *J. Phys. Chem. Solids*, 1958, **5**, 208–223.

[53] C. H. Shomate, *J. Am. Chem. Soc.*, 1944, **66**, 928–929.

[54] C. H. Shomate, *J. Phys. Chem.*, 1954, **58**, 368–372.

[55] D. Frenkel and B. Smit, *Understanding Molecular Simulation: From Algorithms to Applications*, Academic Press, 2002.

[56] M. Born and J. E. Mayer, *Zeitschrift für Phys.*, 1932, **75**, 1–18.

[57] J. Van der Waals, *K. Akad. Wet: Amsterdam, The Netherlands*, 1893.

[58] F. London, *Zeitschrift für Phys.*, 1930, **63**, 245–279.

[59] R. A. Buckingham, *Proc. R. Soc. A Math. Phys. Eng. Sci.*, 1938, **168**, 264–283.

[60] W. C. Swope, H. C. Andersen, P. H. Berens and K. R. Wilson, *J. Chem. Phys.*, 1982, **76**, 637.

[61] M. Born and R. Oppenheimer, *Ann. Phys.*, 1927, **20**, 457–484.

[62] P. Hohenberg and W. Kohn, *Phys. Rev.*, 1964, **136**, B864–B871.

[63] W. Kohn and L. J. Sham, *Phys. Rev.*, 1965, **140**, A1133–A1138.

[64] J. Perdew and Y. Wang, *Phys. Rev. B*, 1992, **46**, 12947–12954.

[65] J. P. Perdew, K. Burke and M. Ernzerhof, *Phys. Rev. Lett.*, 1996, **77**, 3865–3868.

[66] C. Lee, W. Yang and R. G. Parr, *Phys. Rev. B*, 1988, **37**, 785–789.

[67] D. Langreth and M. Mehl, *Phys. Rev. B*, 1983, **28**, 1809–1834.

[68] J. P. Perdew and W. Yue, *Phys. Rev. B*, 1986, **33**, 8800–8802.

[69] A. D. Becke, *Phys. Rev. A*, 1988, **38**, 3098–3100.

[70] A. D. Becke, *J. Chem. Phys.*, 1993, **98**, 1372.

[71] R. Dovesi, *CRYSTAL09 Users' Manual*, Universita di Torino, Torino, 2010.

[72] E. A. Ahmad, L. Liborio, D. Kramer, G. Mallia, A. R. Kucernak and N. M. Harrison, *Phys. Rev. B*, 2011, **84**, 085137.

[73] D. Muñoz, N. Harrison and F. Illas, *Phys. Rev. B*, 2004, **69**, 085115.

[74] J. Muscat, A. Wander and N. M. Harrison, *Chem. Phys. Lett.*, 2001, **342**, 397–401.

[75] G. Mallia and N. Harrison, *Phys. Rev. B*, 2007, **75**, 165201.

[76] N. Wilson, S. Russo, J. Muscat and N. Harrison, *Phys. Rev. B*, 2005, **72**, 024110.

[77] G. C. De Fusco, B. Montanari and N. M. Harrison, *Phys. Rev. B*, 2010, **82**, 220404.

[78] C. L. Bailey, L. Liborio, G. Mallia, S. Tomić and N. M. Harrison, *Phys. Rev. B*, 2010, **81**, 205214.

[79] A. Bloch, Annales de la Faculté des sciences de Toulouse: Mathématiques, 1925, pp. 1–22.

[80] H. J. Monkhorst and J. D. Pack, *Phys. Rev. B*, 1976, **13**, 5188–5192.

[81] M. Dolg, H. Stoll, a. Savin and H. Preuss, *Theor. Chim. Acta*, 1989, **75**, 173–194.

[82] C. D. Ling, D. N. Argyriou, G. Wu and J. J. Neumeier, *J. Solid State Chem.*, 2000, **152**, 517–525.

[83] C. S. Nichols, C. G. Van De Walle and S. T. Pantelides, *Phys. Rev. B*, 1989, **40**, 5484–5496.

[84] N. F. Mott and M. J. Littleton, *Trans. Faraday Soc.*, 1938, **34**, 485.

[85] P. W. Tasker, *J. Phys. C Solid State Phys.*, 1979, **12**, 4977–4984.

[86] J. A. Kilner and M. Burriel, *Annu. Rev. Mater. Res.*, 2014, **44**, 365–393.

[87] E. Bucher and W. Sitte, *Solid State Ionics*, 2011, **192**, 480–482.

[88] H. Ding, A. V. Virkar, M. Liu and F. Liu, *Phys. Chem. Chem. Phys.*, 2013, **15**, 489–496.

[89] J. Zhou, G. Chen, K. Wu and Y. Cheng, *J. Phys. Chem. C*, 2013, **117**, 12991–12999.

[90] N. Gauquelin, T. E. Weirich, M. Ceretti, W. Paulus and M. Schroeder, *Monatshefte für Chemie - Chem. Mon.*, 2009, **140**, 1095–1102.

[91] R. Dovesi, R. Orlando, B. Civalleri, C. Roetti, V. R. Saunders and C. M. Zicovich-Wilson, *Zeitschrift fur Krist.*, 2005, **220**, 571–573.

[92] M. Zinkevich, N. Solak, H. Nitsche, M. Ahrens and F. Aldinger, *J. Alloys Compd.*, 2007, **438**, 92–99.

[93] a. N. Grundy, B. Hallstedt and L. J. Gauckler, *J. Phase Equilibria*, 2001, **22**, 105–113.

[94] K. Johnston, M. Castell, A. Paxton and M. Finnis, *Phys. Rev. B*, 2004, **70**, 085415.

[95] P. Linstrom and W. Mallard, *NIST Chemistry WebBook, NIST Standard Reference Database Number 69*, National Institute of Standards and Technology, 2000.

[96] M. Zinkevich and F. Aldinger, *J. Alloys Compd.*, 2004, **375**, 147–161.

[97] X. Weng, P. Boldrin, I. Abrahams, S. J. Skinner and J. A. Darr, *Chem. Mater.*, 2007, **19**, 4382–4384.

[98] V. I. Voronin, I. F. Berger, V. A. Cherepanov, L. Gavrilova, A. N. Petrov, A. I. Ancharov, B. P. Tolochko and S. G. Nikitenko, *Nucl. Instruments Methods Phys. Res. Sect. A Accel. Spectrometers, Detect. Assoc. Equip.*, 2001, **470**, 202–209.

[99] V. V. Kharton, A. V. Kovalevsky, M. Avdeev, E. V. Tsipis, M. V. Patrakeev, A. A. Yaremchenko, E. N. Naumovich and J. R. Frade, *Chem. Mater.*, 2007, **19**, 2027–2033.

[100] G. Y. Guo and W. M. Temmerman, *Phys. Rev. B*, 1989, **40**, 285–288.

[101] X. Feng and N. Harrison, *Phys. Rev. B*, 2004, **70**, 092402.

[102] Y.-S. Su, T. Kaplan, S. Mahanti and J. Harrison, *Phys. Rev. B*, 1999, **59**, 10521–10529.

[103] M. Greven, R. J. Birgeneau, Y. Endoh, M. A. Kastner, B. Keimer, M. Matsuda, G. Shirane and T. R. Thurston, *Physical Review Letters*, 1994, **72**, 1096–1099.

[104] S. Chakravarty, B. I. Halperin and D. R. Nelson, *Physical Review Letters*, 1988, **60**, 1057–1060.

[105] S. Chakravarty, B. I. Halperin and D. R. Nelson, *Physical Review B*, 1989, **39**, 2344–2371.

[106] L. M. Liborio, C. L. Bailey, G. Mallia, S. Tomic and N. M. Harrison, *J. Appl. Phys.*, 2011, **109**, 023519.

[107] R. D. Holmes, H. S. O'Neill and R. J. Arculus, *Geochim. Cosmochim. Acta*, 1986, **50**, 2439–2452.

[108] H. Jónsson, G. Mills and K. W. Jacobsen, *Classical and Quantum Dynamics in Condensed Phase Simulations*, 1998, 385–404.

[109] A. Rimola, C. M. Zicovich-Wilson, R. Dovesi and P. Ugliengo, *J. Chem. Theory Comput.*, 2010, **6**, 1341–1350.

[110] T. Akashi, M. Nanko, T. Maruyama, Y. Shiraishi and J. Tanabe, *J. Electrochem. Soc.*, 1998, **145**, 2090.

[111] R. D. Shannon, *Acta Crystallographica Section A*, 1976, **32**, 751–767.

[112] E. Boehm, J. M. Bassat, P. Dordor, F. Mauvy, J. C. Grenier and P. Stevens, *Solid State Ionics*, 2005, **176**, 2717–2725.

[113] X. Kuang, M. A. Green, H. Niu, P. Zajdel, C. Dickinson, J. B. Claridge, L. Jantsky and M. J. Rosseinsky, *Nat. Mater.*, 2008, **7**, 498–504.

[114] F. Wei, H. Gasparyan, P. J. Keenan, M. Gutmann, Y. Fang, T. Baikie, J. B. Claridge, P. R. Slater, C. L. Kloc and T. J. White, *J. Mater. Chem. A*, 2015, **3**, 3091–3096.

[115] T. Negas, R. Roth, C. McDaniel, H. Parker and C. Olson, *Mater. Res. Bull.*, 1977, **12**, 1161–1171.

[116] R. Roth, T. Negas, H. Parker, D. Minor and C. Jones, *Mater. Res. Bull.*, 1977, **12**, 1173–1182.

[117] S. J. Skinner, H. M. Palmer, E. S. Raj and J. A. Kilner, *J. Solid State Chem.*, 2004, **177**, 2685–2690.

[118] R. Packer, J. Barlow, A. Cott and S. Skinner, *Solid State Ionics*, 2008, **179**, 1094–1100.

[119] A. Orera and P. R. Slater, *Chem. Mater.*, 2010, **22**, 675–690.

[120] S. Carter, A. Selcuk, R. J. Chater, J. Kajda, J. A. Kilner and B. C. H. Steele, *Solid State Ionics*, 1992, **53-56**, 597–605.

[121] R. J. Packer, S. J. Skinner, A. A. Yaremchenko, E. V. Tsipis, V. V. Kharton, M. V. Patrakeev and Y. A. Bakhteeva, *J. Mater. Chem.*, 2006, **16**, 3503.

[122] R. J. Packer, E. V. Tsipis, C. N. Munnings, V. V. Kharton, S. J. Skinner and J. R. Frade, *Solid State Ionics*, 2006, **177**, 2059–2064.

[123] E. Tsipis, C. Munnings, V. Kharton, S. Skinner and J. Frade, *Solid State Ionics*, 2006, **177**, 1015–1020.

[124] R. J. Packer and S. J. Skinner, *Advanced Materials*, 2010, **22**, 1613–1616.

[125] A. Santoro, M. Marezio, R. Roth and D. Minor, *J. Solid State Chem.*, 1980, **35**, 167–175.

[126] S. Skinner and Y. Kang, *Solid State Sci.*, 2003, **5**, 1475–1479.

[127] S. J. Skinner, I. J. E. Brooks and C. N. Munnings, *Acta Crystallographica Section C Crystal Structure Communications*, 2004, **60**, i37–i39.

[128] R. D. Bayliss, S. S. Pramana, T. An, F. Wei, C. L. Kloc, A. J. White, S. J. Skinner, T. J. White and T. Baikie, *J. Solid State Chem.*, 2013, **204**, 291–297.

[129] J. R. Cava and R. S. Roth, AIP Conference Proceedings, 1979, pp. 361–363.

[130] R. Cava, R. Roth, T. Negas, H. Parker and D. Minor, *J. Solid State Chem.*, 1981, **40**, 318–329.

[131] J. G. Thompson, R. L. Withers and F. J. Brink, *J. Solid State Chem.*, 1999, **143**, 122–131.

[132] S. Vyas, R. W. Grimes, D. H. Gay and A. L. Rohl, *Journal of the Chemical Society, Faraday Transactions*, 1998, **94**, 427–434.

[133] L. Minervini, M. O. Zacate and R. W. Grimes, *Solid State Ionics*, 1999, **116**, 339–349.

[134] M. Sepliarsky, A. Asthagiri, S. R. Phillpot, M. G. Stachiotti and R. L. Migoni, *Curr. Opin. Solid State Mater. Sci.*, 2005, **9**, 107–113.

[135] J. Gale, *J. Chem. Soc., Faraday Trans.*, 1997, **93**, 629–637.

[136] I. T. Todorov, W. Smith, K. Trachenko and M. T. Dove, *J. Mater. Chem.*, 2006, **16**, 1911–1918.

[137] W. Smith and T. Forester, *J. Mol. Graph.*, 1996, **14**, 136–141.

[138] W. Humphrey, A. Dalke and K. Schulten, *J. Mol. Graph.*, 1996, **14**, 33–38.

[139] D. Parfitt, A. Chroneos, J. a. Kilner and R. W. Grimes, *Phys. Chem. Chem. Phys.*, 2010, **12**, 6834–6.

[140] D. Rupasov, A. Chroneos, D. Parfitt, J. A. Kilner, R. W. Grimes, S. Y. Istomin and E. V. Antipov, *Phys. Rev. B*, 2009, **79**, 172102.

[141] M. Burriel, J. Peña-Martínez, R. J. Chater, S. Fearn, A. V. Berenov, S. J. Skinner and J. A. Kilner, *Chemistry of Materials*, 2012, **24**, 613–621.

[142] R. I. Dass, J.-Q. Yan and J. B. Goodenough, *Physical Review B*, 2003, **68**, 064415.

[143] J. H. Lee, G. Luo, I. C. Tung, S. H. Chang, Z. Luo, M. Malshe, M. Gadre, A. Bhattacharya, S. M. Nakhmanson, J. A. Eastman, H. Hong, J. Jellinek, D. Morgan, D. D. Fong and J. W. Freeland, *Nat. Mater.*, 2014, **13**, 879–883.

[144] J. Wan, J. B. Goodenough and J. H. Zhu, *Solid State Ionics*, 2007, **178**, 281–286.

Copyrights and Reprint Permissions

Why Ni is absent from the surface of $La_2NiO_{4+\delta}$?

J. Wu, S. S. Pramana, S. J. Skinner, J. A. Kilner and A. P. Horsfield, *J. Mater. Chem. A*, 2015, **3**, 23760
DOI: 10.1039/C5TA03759J

This article is licensed under a Creative Commons Attribution 3.0 Unported Licence. Material from this article can be used in other publications provided that the correct acknowledgement is given with the reproduced material.

Reproduced material should be attributed as follows:

- For reproduction of material from NJC:
  [Original citation] - Published by The Royal Society of Chemistry (RSC) on behalf of the Centre National de la Recherche Scientifique (CNRS) and the RSC.
- For reproduction of material from PCCP:
  [Original citation] - Published by the PCCP Owner Societies.
- For reproduction of material from PPS:
  [Original citation] - Published by The Royal Society of Chemistry (RSC) on behalf of the European Society for Photobiology, the European Photochemistry Association, and RSC.
- For reproduction of material from all other RSC journals:
  [Original citation] - Published by The Royal Society of Chemistry.

Information about reproducing material from RSC articles with different licences is available on our Permission Requests page.

Copyright Clearance Center RightsLink®

Home Create Account Help Live Chat

ACS Publications Most Trusted. Most Cited. Most Read.

Title: Correlation of Local Structure and Diffusion Pathways in the Modulated Anisotropic Oxide Ion Conductor CeNbO4.25

Author: Stevin S. Pramana, Tom Baikie, Tao An, et al

Publication: Journal of the American Chemical Society

Publisher: American Chemical Society

Date: Feb 1, 2016

Copyright © 2016, American Chemical Society

LOGIN

If you're a copyright.com user, you can login to RightsLink using your copyright.com credentials. Already a RightsLink user or want to learn more?

Quick Price Estimate

Permission for this particular request is granted for print and electronic formats, and translations, at no charge. Figures and tables may be modified. Appropriate credit should be given. Please print this page for your records and provide a copy to your publisher. Requests for up to 4 figures require only this record. Five or more figures will generate a printout of additional terms and conditions. Appropriate credit should read: "Reprinted with permission from {COMPLETE REFERENCE CITATION}. Copyright {YEAR} American Chemical Society." Insert appropriate information in pl